Universidad Carlos III de Madrid
www.uc3m.es

TESIS DOCTORAL

Advanced Acquisition and Reconstruction Techniques in Magnetic Resonance Imaging

Autor:

Paula Montesinos Suárez de la Vega

Directores:

Manuel Desco Menéndez

Juan Felipe Pérez-Juste Abascal

Tutor:

Manuel Desco Menéndez

DEPARTAMENTO DE BIOINGENIERÍA E INGENIERÍA AEROESPACIAL

Leganés, julio 2015

TESIS DOCTORAL

Advanced Acquisition and Reconstruction Techniques in Magnetic Resonance Imaging

Autor: *Paula Montesinos Suárez de la Vega*

Directores:

Manuel Desco Menéndez

Juan Felipe Pérez-Juste Abascal

Firma del Tribunal Calificador:

Firma

Presidente:

Vocal:

Secretario:

Calificación:

Leganés, julio de 2015

« Il dépend de celui qui passe
Que je sois tombe ou trésor
Que je parle ou me taise
Ceci ne tient qu'à toi
Ami n'entre pas sans désir »

Table of contents

Resumen

La Imagen por Resonancia Magnética (IRM) es una modalidad de imagen biomédica con notables características tales como un excelente contraste en tejidos blandos y una muy alta resolución espacial. Sin embargo, a pesar de estas importantes propiedades, la IRM tiene algunos inconvenientes, como una baja sensibilidad y tiempos de adquisición muy largos. Esta tesis se centra en buscar soluciones para el segundo inconveniente mencionado a través del uso de metodologías de *compressed sensing*.

Compressed sensing es una técnica novedosa que permite la reducción de los tiempos de adquisición y también la mejora de la resolución espacio-temporal y la calidad de las imágenes. La teoría de *compressed sensing* va más allá los límites tradicionales de la teoría de muestreo de Nyquist, permitiendo la reconstrucción de imágenes a partir de un número incompleto de muestras siempre que se cumpla que 1) las imágenes a reconstruir tengan una representación dispersa (*sparse*) en un determinado dominio, 2) el submuestreo aplicado sea aleatorio y 3) se usen algoritmos de reconstrucción no lineales específicos.

La resonancia magnética cardiovascular tiene que superar muchas limitaciones derivadas de los ciclos respiratorios y cardiacos, y además tiene que cumplir unos requisitos de resolución espacio-temporal muy estrictos. De ahí que cualquier mejora que se pueda conseguir bien reduciendo tiempos de adquisición o bien aumentando la calidad de las imágenes resultaría altamente beneficiosa. Esta tesis tiene como objetivo investigar los beneficios que la técnica de *compressed sensing* puede proporcionar a dos aplicaciones punteras en RM cardiovascular, la adquisición de cines cardiacos de pequeño animal y la visualización de placas ateroscleróticas en arterias coronarias en humano.

La adquisición de cines cardiacos en pequeño animal es una aplicación ampliamente usada para evaluar función cardiovascular. En esta tesis, proponemos una metodología de *compressed sensing* para reducir los tiempos de adquisición de secuencias de cine cardiaco denominadas *self-gated*. Desarrollamos esta metodología modificando el algoritmo de reconstrucción de Split-Bregman para incluir la minimización de la Variación Total a través de la dimensión temporal además de la espacial. Para ello, simulamos adquisiciones de *compressed sensing* submuestreando retrospectivamente adquisiciones completas. La calidad de los resultados se evaluó con medidas funcionales tanto en animales sanos como en animales a los que se les produjo un infarto cardiaco. El método propuesto mostró que factores de aceleración de 10-14 son posibles para animales sanos y en torno a 10 para animales infartados.

Estos factores de aceleración teóricos se verificaron en la práctica mediante la implementación de una adquisición submuestreada en un escáner de IRM de pequeño animal de 7 T. Se demostró que aceleraciones en torno a 10 son factibles en la práctica, valor muy cercano a los obtenidos en las simulaciones previas. Sin embargo para factores de aceleración muy altos, se apreciaron algunas diferencias entre la calidad de las imágenes con submuestreo simulado y las realmente submuestreadas; esto puede ser debido a una mayor sensibilidad a la contaminación por movimiento durante la adquisición.

La segunda aplicación cardiovascular explorada en esta tesis es la visualización de placas ateroscleróticas en arterias coronarias en humanos. Hoy en día, la visualización y clasificación *in vivo* de es te tipo de placas mediante IRM aún no es técnicamente posible. Pero no hay duda de que técnicas de aceleración, como *compressed sensing,* pueden contribuir enormemente a la consecución de la aplicación *in vivo*. Sin embargo, como paso previo a la evaluación de las técnicas de aceleración, es conveniente hacer un estudio sistemático de los requerimientos técnicos necesarios para la correcta visualización y caracterización de las placas coronarias.

Mediante simulaciones establecimos los límites de señal a ruido, resolución espacial y movimiento requeridos para la correcta visualización de las placas y propusimos un nuevo esquema de adquisición híbrido que reduce la sensibilidad al movimiento. Para valorar los beneficios que las técnicas de aceleración pueden aportar, evaluamos diferentes algoritmos de imagen en paralelo e implementamos una metodología de *compresed sensing* que tiene en cuenta la información de los mapas de sensibilidad de las antenas utilizadas. En este estudio se encontró, que para la configuración de antenas analizadas, los beneficios de la aceleración están muy limitados por el pequeño campo de visón utilizado. Por tanto, para incrementar los beneficios que estas técnicas de aceleración pueden aportar la imagen de placas coronarias *in vivo*, es necesario diseñar antenas específicas para esta aplicación.

Abstract

Magnetic Resonance Imaging (MRI) is a biomedical imaging modality with outstanding features such as excellent soft tissue contrast and very high spatial resolution. Despite its great properties, MRI suffers from some drawbacks, such as low sensitivity and long acquisition times. This thesis focuses on providing solutions for the second MR drawback, through the use of compressed sensing methodologies.

Compressed sensing is a novel technique that enables the reduction of acquisition times and can also improve spatiotemporal resolution and image quality. Compressed sensing surpasses the traditional limits of Nyquist sampling theories by enabling the reconstruction of images from an incomplete number of acquired samples, provided that 1) the images to reconstruct have a sparse representation in a certain domain, 2) the undersampling applied is random and 3) specific non-linear reconstruction algorithms are used.

Cardiovascular MRI has to overcome many limitations derived from the respiratory and cardiac cycles, and has very strict requirements in terms of spatiotemporal resolution. Hence, any improvement in terms of reducing acquisition times or increasing image quality by means of compressed sensing will be highly beneficial. This thesis aims to investigate the benefits that compressed sensing may provide in two cardiovascular MR applications: The acquisition of small-animal cardiac cine images and the visualization of human coronary atherosclerotic plaques.

Cardiac cine in small-animals is a widely used approach to assess cardiovascular function. In this work we proposed a new compressed sensing methodology to reduce acquisition times in self-gated cardiac cine sequences. This methodology was developed as a modification of the Split Bregman reconstruction algorithm to include the minimization of Total Variation across both spatial and temporal dimensions. We simulated compressed sensing acquisitions by retrospectively undersampling complete acquisitions. The accuracy of the results was evaluated with functional measurements in both healthy animals and animals with myocardial infarction. The method reached accelerations rates of 10-14 for healthy animals and acceleration rates of 10 in the case of unhealthy animals.

We verified these theoretically-feasible acceleration factors in practice with the implementation of a real compressed sensing acquisition in a 7 T small-animal MR scanner. We demonstrated that acceleration factors around 10 are achievable in practice, close to those obtained in the previous simulations. However, we found some small differences in image quality between simulated and real undersampled compressed sensing reconstructions at high acceleration rates;

this might be explained by differences in their sensitivity to motion contamination during acquisition.

The second cardiovascular application explored in this thesis is the visualization of atherosclerotic plaques in coronary arteries in humans. Nowadays, *in vivo* visualization and classification of plaques by MRI is not yet technically feasible. Acceleration techniques such as compressed sensing may greatly contribute to the feasibility of the application *in vivo*. However, it is advisable to carry out a systematic study of the basic technical requirements for the coronary plaque visualization prior to designing specific acquisition techniques.

On simulation studies we assessed spatial resolution, SNR and motion limits required for the proper visualization of coronary plaques and we proposed a new hybrid acquisition scheme that reduces sensitivity to motion. In order to evaluate the benefits that acceleration techniques might provide, we evaluated different parallel imaging algorithms and we also implemented a compressed sensing methodology that incorporates information from the coil sensitivity profile of the phased-array coil used. We found that, with the coil setup analyzed, acceleration benefits were greatly limited by the small size of the FOV of interest. Thus, dedicated phased-arrays need to be designed to enhance the benefits that accelerating techniques may provide on coronary artery plaque imaging *in vivo*.

Lista de abreviaturas

CT Computerized Tomography

CS Compressed Sensing

ECG Electrocardiogram

FLASH Fast Low Angle Shot

FOV Fielf of View

GRE Gradient Echo

MR Magnetic Resonance

MRI Magnetic Resonance Imaging

PET Positron Emission Tomography

RM Residual Motion

RMSE Root Mean Squared Error

ROI Region of Interest

SNR Signal to Noise Ratio

SPECT Single Photon Emission Computed Tomography

SVD Singular Value Decomposition

UTE Ultrashort Echo Time

TV Total Variation

1. Motivation and objectives

1.1 Motivation

Magnetic Resonance Imaging (MRI) is a biomedical imaging modality with outstanding features such as excellent soft tissue contrast and very high spatial resolution. However, MRI suffers from some drawbacks, as for instance long acquisition times and low sensitivity. Many efforts have been traditionally devoted to provide solutions to reduce these drawbacks. New fast sequences and new acceleration strategies such as partial Fourier or parallel imaging have been developed in the past 20 years, in order to shorten acquisition times in MRI. In this context, compressed sensing emerged with force in MRI around 2007, causing a great impact in the MRI community.

Compressed sensing theory surpasses the traditional limits of sampling theories (Nyquist theorem), enabling the reconstruction of images from an incomplete number of acquired samples, provided that the images to reconstruct have a sparse representation in a certain domain, that the undersampling applied is random and that specific non-linear reconstruction algorithms are used. Compressed sensing is quite a novel technique with great potential in MRI; it enables the reduction of acquisition times thus saving imaging costs. Besides, it can serve to improve spatiotemporal resolution and image quality, and it has also opened the opportunity of exploring new MR applications and new MR boundaries.

The overall impact of compressed sensing in MR is indeed of importance, but some applications can particularly benefit from its application. We believe this is the case of cardiovascular MRI. Cardiovascular MRI is a specially challenging and demanding area, as it has to deal with respiratory and cardiac motion, it requires a very high spatiotemporal resolution, and long acquisition times are prohibitive. This thesis aims to investigate the potential benefits of using compressed sensing in two leading cardiovascular MR applications: Cardiac cine in small animals and atherosclerotic plaque visualization in humans.

Cardiac cine acquisition in small animals is a widespread application, very useful to investigate cardiac pathologies and treatments. There are very well established cardiac cine sequences to evaluate relevant cardiovascular parameters such as ejection fraction, heart motility or left ventricular mass in both preclinical and clinical areas. Nevertheless, when whole hearts are scanned in preclinical MR, acquisition time tends to become prohibitively long, thus greatly limiting image quality and spatial resolution. Compressed sensing has been previously proposed to reduce acquisition time in cardiac cine sequences in humans, reporting excellent acceleration factors [1-7]; therefore, we believe the technique has a great potential to accelerate small-animal

cardiac sequences. However, there are few works exploring its applicability in small-animal sequences and the accelerations reported were quite modest [4, 8-11]. In addition, it is important to mention that most of the compressed sensing works published in the literature were just based on simulation studies and very few actually used real compressed sensing implementations.

Within this context, this thesis aims to explore the benefits of applying compressed sensing to reduce acquisition times in small-animal cardiac cine MR sequences. With that purpose, a new compressed sensing methodology is proposed and developed. This methodology is evaluated in terms of clinically relevant functional measurements in both healthy and unhealthy subjects. Moreover, theoretical feasible accelerations are verified in practice, with the implementation of a real compressed sensing acquisition in a small-animal MR scanner.

The second cardiovascular application explored in this thesis is the visualization of atherosclerotic plaques in coronary arteries in humans. Nowadays, clinical routine for the evaluation of coronary atherosclerotic plaques is based on computerized tomography (CT). Although *in vivo* visualization and classification of plaques by MRI is not yet technically feasible, there is clear consensus on the great benefits that an MRI-based approach would report. So far, coronary wall imaging has been limited to angiography, wall thickening, delayed enhancement and intraplaque hemorrhage studies [12-14]. The feasibility of the assessment of plaque morphology in coronary vessels has been encouraged by recent findings in carotid plaque characterization [15-19] and by *ex vivo* studies that demonstrated the potential of multicontrast MR to classify human coronary atherosclerotic plaques [20].

There is no doubt that the visualization of coronary plaques involves a lot of challenges to overcome, as very high spatial resolution requirements and respiratory and cardiac motion contamination. But, as it has been demonstrated in many other cardiovascular applications, we believe that compressed sensing can greatly contribute to the ultimate feasibility of the application *in vivo*. However, prior to the evaluation of the benefits that acceleration techniques might report, a systematic study of the basic technical requirements for the coronary plaque visualization has to be carried out.

Specifically, this thesis aims to define the spatial resolution, SNR (Signal to Noise Ratio) and motion limits required for the proper visualization of coronary plaques in humans *in vivo*. Once those thresholds are established, we aim to explore the potential benefits that compressed sensing and other acceleration techniques might provide for future *in vivo* human coronary plaque visualizations.

1.2 Objectives

The main objective of this thesis is to explore and evaluate the benefits that compressed sensing may provide to cardiovascular MRI, in particular to two leading applications: The acquisition of cardiac cines in small animals and the visualization coronary atherosclerotic plaques in humans.

The specific objectives of this thesis are the following:

1. To explore a new compressed sensing methodology to accelerate small-animal self-gated cardiac cine sequences and to study its feasibility and the benefits that it may report.
2. To implement a compressed sensing acquisition of a self-gated cardiac cine sequence in a small-animal MRI scanner and to validate the achievable acceleration factors in practice with the methodology proposed.
3. To investigate the resolution, SNR and motion limits required for the proper visualization and characterization of coronary atherosclerotic plaques in humans.
4. To explore the benefits that acceleration techniques may report for future *in vivo* coronary atherosclerotic plaques visualization studies using a 34 channel coil setup as a potential clinical scenario

1.3 Outline of the document

The present document is organized into nine chapters. Chapter 1 presents the motivation and objectives of the work. Chapter 2 introduces the main actual MRI challenges and the state of art that are the bases of this thesis. Chapter 3 provides a technical description of the fundamentals of the compressed sensing technique and the Split Bregman methodology used along the thesis. Chapter 4 presents a new compressed sensing methodology to accelerate small-animal cardiac cine studies. This compressed sensing approach is based on the Split-Bregman formulation, modified to minimize Total Variation (TV) across space and time. The benefits of this methodology are retrospectively evaluated in four healthy and two infarcted subjects. The attainable acceleration rates for this type of studies are assessed by quantitative and functional measurements.

Chapter 5 addresses the practical implementation of the compressed sensing methodology presented in Chapter 4. Compressed sensing undersampling requirements are achieved by modifying a standard cardiac cine sequence in a 7 T small-animal scanner. Differences between theoretical and practical achievable accelerations are evaluated in two healthy animal datasets.

Chapter 6 studies the limits in resolution, SNR and motion required for proper visualization and characterization of coronary atherosclerotic plaques in future *in vivo* applications. This chapter is based on simulations using *ex vivo* high-resolution datasets merged with *in vivo* coronary motion profiles.

Chapter 7 evaluates the potential benefits of applying acceleration techniques for the future visualization of human coronary atherosclerotic plaques *in vivo*. Same motion profiles as in Chapter 6 are used to mimic an *in vivo* acquisition. A clinical scenario is simulated using a 34 channel coil and a small inner FOV (Field Of View). Several parallel imaging techniques such GRAPPA, SENSE and a modification of SENSE in which TV is used are evaluated for different acceleration rates. Also, a compressed sensing methodology incorporating the coils sensitivity profile information into the solution of the problem is implemented and evaluated. All methods are compared and their benefits in terms of tolerance to motion are evaluated.

Finally, the Chapter 8 presents a global discussion together with the main conclusions and contributions of this thesis and some possible lines of future work. Finally, Chapter 9 presents the publications derived from this thesis.

2. Introduction

There is a general consensus about the great contribution of biomedical imaging techniques to the progress of medicine, as they provide some of the most useful tools for diagnosis and research. Noninvasive technologies such as computerized tomography (CT), positron emission tomography (PET), single photon emission computed tomography (SPECT) or magnetic resonance imaging (MRI) enable the detection, characterization and measurement of biological process at cellular and molecular levels without perturbing the systems under study [21] [22].

In particular, the discovery of nuclear magnetic resonance (NMR) revolutionized chemical and medical imaging areas [23]. Presently, MRI is recognized as one of the most important medical advances of the century, as it has opened new opportunities to improve the knowledge about the human body, revealing structural and functional information at a level unimaginable before [24]. MRI offers excellent features for preclinical and clinical fields, such as high spatial resolution and great soft-tissue contrast. Details about MRI physical principles are beyond the scope to this document, excellent explanations about MRI fundamentals can be found in [24-26].

Despite its great properties, MRI suffers from some drawbacks, such as low sensitivity and long acquisition times. Much research effort has been focused on improving these two downsides to fully exploit the tremendous potential of MRI [27]. MRI sensitivity has been enhanced by increasing magnetic field strengths, designing new SNR-improved radiofrequency coils (cryo-coils) and developing new specific contrast agents.

This thesis focuses on providing solutions for the second MR drawback, its long acquisition times. As it will be described later, due to the particular way data are collected in MRI, the acquisition process is slow compared with other imaging modalities. Shortening MR acquisition times is very appealing as it would result in a direct reduction of the costs of MR imaging and/or in improvements of image quality. Many efforts have been devoted to develop acceleration solutions for MRI, of very diverse nature. For example, fast sequences, k-space modified trajectories, parallel imaging strategies, etc. Amongst these strategies, compressed sensing emerged with force in the past years, revolutionizing the state-of-the-art and providing abundant benefits to many different MRI areas.

The application of compressed sensing seems particularly beneficial in some areas of MRI research and diagnosis, such as cardiovascular MRI [28]. Cardiovascular MR, which includes cardiac and coronary imaging, is indeed one of the most complicated and challenging MR applications. Cardiovascular MR has to overcome many limitations derived from the respiratory

and cardiac cycles, and has very strict requirements in terms of spatiotemporal resolution. Hence, any improvement derived from compressed sensing techniques in terms of reducing acquisition times or increasing image quality in cardiovascular MR will be highly beneficial.

In this context, this thesis aims to investigate the benefits that compressed sensing may provide in two leading and challenging cardiovascular MR applications: The acquisition of small-animal cardiac cine images and the visualization of human coronary atherosclerotic plaques. The first one is a widely used approach to assess cardiovascular function in preclinical MR whilst the second one is a potential MR clinical application of high interest.

2.1 Preclinical and clinical MRI

This section aims to explain the main differences between preclinical and clinical MRI and how despite their different technological requirements, both areas can highly benefit from compressed sensing methodologies.

From an engineering point of view, the main differences between preclinical and clinical MRI derive from the very different sample sizes involved. Preclinical scanners are generally focused on small animals, usually rodents, as it is the case of the 7 T preclinical scanner used in the first chapters of this thesis. The scale factor between humans and rodents translates into a much higher spatial resolution required in preclinical scanners in order to make both applications equivalent, which requires powerful magnetic field gradients. Besides, the small sample size used in preclinical scanners conditions a very low MR signal, together with low SNR levels, which can be partially alleviated by using very high magnetic field strengths. Small animal scanners usually have a bore size of about 20 cm, with main magnetic field intensities usually ranging from 4.7 to 16.4 T; clinical scanners usually have 70 cm bore size, with intensities in the order of 1.5-3 T (although some research human scanners can reach 7 T). As an example, figure 2.1 shows two different experimental setups for preclinical and clinical scanners. Differences in the bore size and also in the type of samples that can be acquired are easily appreciated.

Besides hardware differences, differences in sample size and the biological processes of the subjects under study (i.e., blood flow or cardiac and respiratory cycles) are indirectly translated into different imaging requirements. In general, a much higher temporal resolution is required in preclinical scanners due to faster biological process in small animals. Besides, there are other practical issues to take into account: One of the most obvious is the need of anesthetizing the animals while they are scanned, which demands proper monitoring of their vital constants.

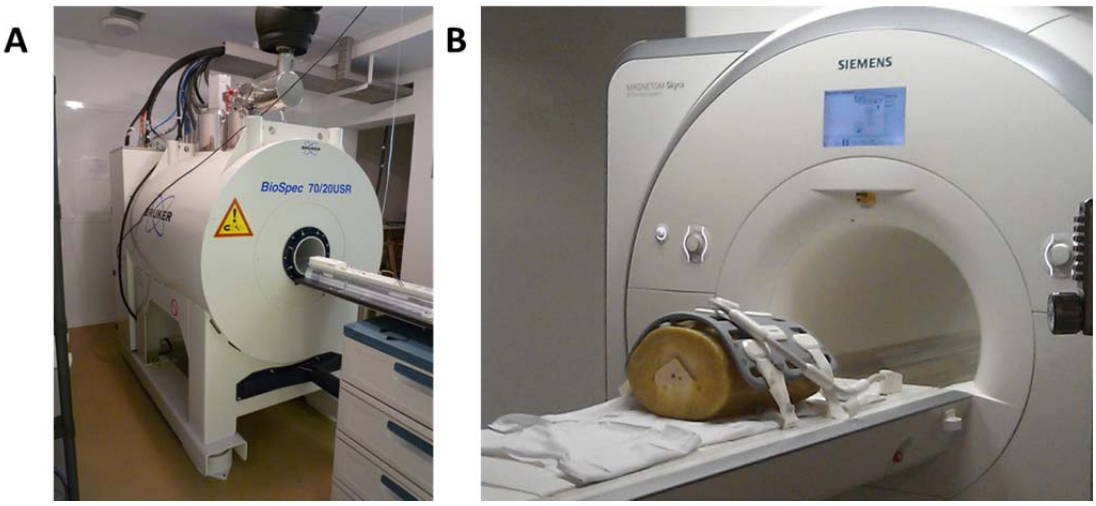

Figure 2.1 Preclinical and clinical cardiac experimental setup. A) 7 T preclinical MRI scanner, Bruker BioSpec 70/20 USR. B) 3T clinical MRI scanner, Skyra, Siemens Medical.

Reducing acquisition time is greatly appealing for both clinical and preclinical worlds. On the clinical side, reducing the scan time is particularly important when physical conditions of the patients are complicated, such as children or elder people, claustrophobic patients, patients with difficulties to hold position or respiration etc. From a logistical standpoint, it will increment the number of patients that can be scanned in the same time period, thus reducing cost and waiting lists.

In a preclinical environment, shorter acquisition times also have very important practical consequences. First, time efficiency of the scanners increase, as in the human case, enabling a higher throughput. Second, shorter scans reduce the amount of anesthesia inhaled, reduce cost and minimize the risk of developing hypothermia.

Moreover, as mentioned before, faster acquisition strategies can serve not only to reduce acquisition time and costs, but also to improve image quality. In both preclinical and clinical scenarios, faster acquisition strategies will result in less motion contamination, which is one of the main sources of artifacts in MRI. Furthermore, the savings in acquisition time can be used to either improve the SNR (by increasing the number of repetitions of the experiment) or the spatial resolution of the study (by increasing the number of phase encoding line to acquire). Most importantly, faster acquisitions may enable increases in temporal resolution, allowing us to monitor very fast physiological process. Significant biological and physiological information can be obtained from these faster acquisitions, such as contrast circulation, cardiac contraction etc.

2.2 Challenges in cardiovascular MRI

MRI acquisitions are a tradeoff between acquisition time, spatiotemporal resolution and SNR. This tradeoff is specially challenging in cardiovascular MR, where a delicate balance has to be found among all those factors. Cardiovascular MR is a very particular area, where the image is greatly influenced by cardiac and respiratory motion, which produces artifacts and blurring in the images. Besides the difficulties imposed by the presence of high amounts of motion, very high temporal and spatial resolutions are usually required [29]. The combination of all these factors makes cardiovascular MR one of the most attractive research MR areas.

To face cardiac and respiratory movement effects, gating methods are essential; gating can be performed in a prospective or retrospective way. In the former, the acquisition is stopped/triggered by particular events of the cardiac cycle being monitored, while in retrospective gating the acquisition runs in continuous mode, and later data corresponding to certain parts of the cycle are either discarded or binned into different frames.

Regarding respiratory motion, it is normally addressed by using breathold acquisition or respiratory gating. Respiratory gating is generally carried out using diaphragmatic navigators either in a prospective or retrospective way. In clinical scenarios, breatholding can be very difficult for unstable patients with deteriorated health conditions or respiratory difficulties. Furthermore, if an image is acquired in different breatholds, some mismatch can be noticed between different diaphragmatic positions. Thus, great accelerations are required to achieve free breathing acquisitions, which are highly desirable in clinical scenarios. Regarding preclinical scenarios, breatholding is only possible with assisted ventilation, which normally involves extra complications and is difficult to carry out.

Regarding cardiac motion, cardiac gating is the easiest method to achieve cardiac synchronization in both preclinical and clinical scenarios. This method makes it possible to obtain static or cine images with good quality and no motion contamination. Both ECG electrodes or navigators can be used to generate the gating signal [29], in either prospective or retrospective ways. However, the use of electrodes is more difficult in preclinical scenarios, where the signal is more difficult to obtain and its quality is easily impaired by high magnetic field effects. For this reason, the use of retrospective gating is very common in preclinical MRI.

All these challenges make cardiovascular MR one of the areas where acceleration techniques have indeed a greater impact [28].

2.2.1 Cardiac cine MR in small animals

Cardiac cine in small-animals is a widely used approach to assess cardiovascular function [30-33]. The acquisition of cine images enables the quantification of important functional parameters such as ejection fraction, heart motility, wall thickening or left ventricle mass [29].

The acquisition of cardiac cine sequences in small animals requires both respiratory and cardiac gating. This thesis focuses on a particular family of sequences, known as self-gated cine sequences [30]. This type of sequences avoids the use of electrodes in the animal and uses navigator data to properly classify acquired data into different cardiac frames and to reject data contaminated by respiratory motion. Acquisition times may become prohibitively long when acquiring the whole heart of the animals (scans can last up to 40 min [34]), and great benefits could be obtained from its acceleration. Besides reducing the total acquisition time, faster sequences may improve image quality, since cardiac cine sequences are very prone to motion artifacts. Furthermore, an enhanced temporal resolution may increase the number of different cardiac phases acquired [28, 35].

Figure 2.2 illustrates an example of small-animal cardiac cine images obtained with a self-gated sequence. End of systole and end of diastole frames are shown, as those are the most relevant cardiac phases for the calculation of quantitative measurements.

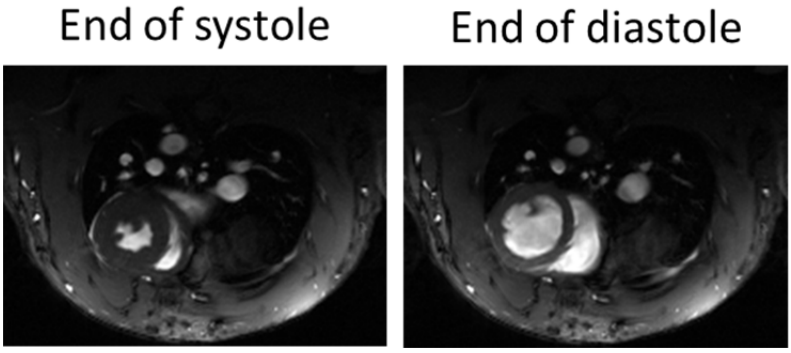

Figure 2.2 End systolic and end diastolic frames of a rat cardiac cine

2.2.2 Coronary atherosclerotic plaque visualization in humans

Atherosclerosis is a systemic and multifocal disease, that starts early in life. Most atherosclerotic plaques remain asymptomatic for years; over time some may become obstructive and a few may become vulnerable and prone to rupture/erosion/thrombosis [36]. The rupture of vulnerable (high-risk) plaques is the main cause of cardiovascular events, including myocardial infarction and stroke [37]. Imaging is key for prognosis and diagnosis and is essential to identify

the presence, extension, progression or regression of disease as well as vulnerability of plaques [36].

Currently, clinically established imaging methods rely on the quantification of the degree of stenosis to predict plaque risk. However, an increasing number of studies have demonstrated that the majority of unstable or ruptured atherosclerotic plaques can be found in arteries with a degree of stenosis of less than 60% [38]. The literature also points that the identification of morphological characteristics such as fibrous cap thickness, luminal stenosis, plaque area, necrotic core area, macrophage area and calcification determine the likelihood of adverse cardiovascular events [39, 40]. All these facts signal the need of developing imaging approaches for the *in vivo* visualization and characterization of atherosclerotic plaques. Clinical standard nowadays is based on CT imaging; non-invasive and non-ionizing imaging techniques such as MRI, that would avoid the use of radiation for diagnosis and follow up processes, are highly desirable, but not enough developed nowadays.

The main limitations to face for future atherosclerosis MRI detection in coronary vessels might be posed by SNR, resolution, acquisition time and particularly by coronary motion. All those limitations and the way to overcome them are investigated in this thesis. Among other strategies, we believe that acceleration techniques such as compressed sensing can definitively help to alleviate those restrictions.

Figure 2.3 shows an example of an *ex vivo* MRI atherosclerotic plaque acquisition . The high degree of spatial detail of this acquisition allows differentiation of morphological plaque features [20], as is the case of the calcification indicated in the image.

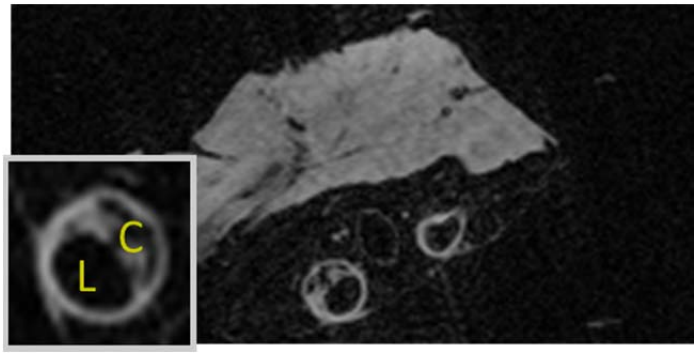

Figure 2.3 Ex vivo heart with diagnosed atherosclerotic plaques. Detail: zoom of a vessel section. The hypointense area on the right is an area of plaque calcification (C). The vessel lumen is the larger hypointense area on the left (L).

2.3 MRI acceleration techniques

MR imaging is a complex procedure that involves several steps such as signal generation, spatial codification, signal sampling, data storage and image reconstruction. A detailed description of these steps can be found elsewhere [24, 25]. The work developed in this thesis is closely related with two of those steps, signal sampling and image reconstruction.

Signal sampling in standard MRI acquisitions is governed by the Shannon-Nyquist theorem and reconstruction is generally performed by a standard Fourier transform. Sometimes the standard sampling process is modified for acceleration purposes; generally, in those cases, the reconstruction process needs to be also modified, as a standard Fourier transform would lead to artifacts in the reconstruction.

As mentioned before, great research effort has been devoted to develop efficient acceleration techniques in MRI, and many strategies involving different levels of complexity have been proposed. The range of accelerations attainable differs greatly from one technique to other, as well as their advantages and disadvantages. Some of the most commonly used acceleration strategies are:

- Fast sequences
- Strategies to reduce the number of phase encoding lines acquired
- Modified k-space trajectories
- Parallel imaging
- Techniques exploiting spatiotemporal redundancy
- Compressed sensing

Faster acquisitions can be achieved by modifying either sequence schemes or k-space trajectories. Traditional spin echo sequences have been wisely modified in different ways leading to faster MRI sequences, as is the case of Echo Planar Imaging, Turbo Spin Echo or Fast Spin Echo sequences [41, 42]. In these cases, more than one signal echo (phase encoding line) is acquired per excitation. On top of that, there are also simple acceleration strategies that can be applied to conventional Cartesian sequences, such as zero filling or Partial Fourier, which just reduce the number of phase encoding lines actually acquired per k-space. These strategies do not imply very complex modifications in the reconstruction process, although the achievable accelerations are quite modest, normally with acceleration rates inferior to two [43, 44].

Besides these strategies, there is also a great variety of sequences that use non-Cartesian k-space sampling trajectories, which are able to collect k-space data in few miliseconds. These

trajectories are generally obtained using special gradient waveforms, as it is the case of radial, propeller or spiral acquisitions [45-50]. All this non-Cartesian trajectories imply a modification of the standard Fourier transform reconstruction and present some drawbacks to consider, such as the introduction of artifacts, off-resonance effects or a lower spatial resolution.

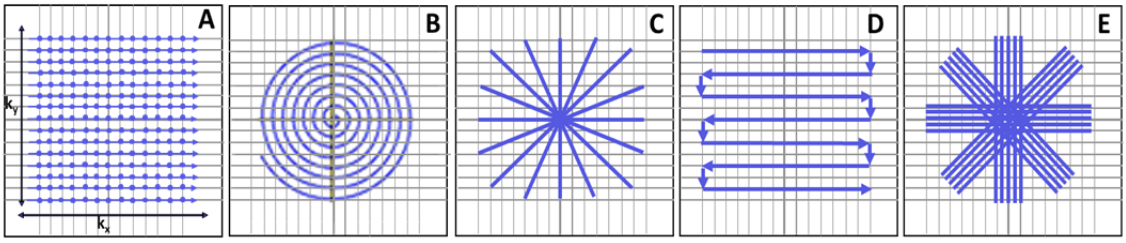

Figure 2.4. Different k-space sampling schemes. A) Standard Cartesian sampling. B) Spiral. C) Radial. D) EPI. E) PROPELLER

Higher acceleration factors can be obtained with more complex strategies: parallel imaging, techniques exploiting temporal redundancy and compressed sensing. Parallel imaging has been widely used in MRI through the past 20 years and is nowadays completely incorporated into many clinical routines. Techniques exploiting temporal redundancy and compressed sensing are more novel and some of them are still under development and do not have reached yet their maximum potential. All these strategies are based on the idea of undersampling or subsampling the k-space to reduce the acquisition times, but each of them follows a different strategy. Different undersampling schemes actually lead to different artifacts in the images, and thus different methods are used to eliminate them. For example, if a Cartesian k-space is undersampled in a uniform way and we perform a standard Fourier reconstruction, structured aliasing artifacts appear in the image (figure 2.5). This is the base of parallel imaging and some of the algorithms exploiting temporal redundancy. However, if we undersample the k-space in a random way, and we perform a standard reconstruction, unstructured artifacts will appear in the reconstruction. These unstructured artifacts can be removed with compressed sensing reconstruction algorithms [51], as we will discuss later in detail.

All the acceleration strategies mentioned above are just a sample of the fruitful work done on the field in the past decades. Many other methods have been developed for specific applications, as for example the Keyhole technique used in dynamic imaging [53]. A more detailed description of fast sequences and acceleration strategies can be found in [24, 25].

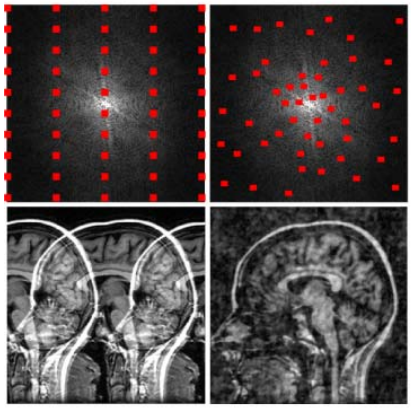

Figure 2.5 Effects of undersampling in an MR brain image. On the left uniform undersampling causes structured artifacts in the reconstructed image. On the right, random undersampling produces incoherent artifacts in the reconstructed image [52].

2.3.1 Parallel imaging

Parallel imaging relies on the use of the multiple elements of a phased array coil [54] in reception. As mentioned above, in parallel imaging the amount of data acquired in the k-space is reduced. The undersampling scheme followed with this technique is uniform, what implies that, structured artifacts appear in the reconstructed images after a standard reconstruction (figure 2.5), called aliased images. Advanced techniques exploit the information provided by the different elements of the phased-array coils to reconstruct artifact-free images.

There are two main families of parallel imaging reconstruction strategies, those applied in the k-space domain or those applied in the image domain. The objective of those reconstructions is either to fill the missing k-space lines, as is the case of SMASH [55] and GRAPPA [56], or to unfold the aliased images as is the case of SENSE [57] and PILS [58]. A detailed description of these parallel imaging strategies and its advantages can be found in the literature [59].

Acceleration rates are highly dependent on the particular application, which determines the coil configuration, its number of elements, the magnetic field strength, etc. Nowadays acceleration rates around 2-6 are commonly used in clinical cardiovascular environments [60]. In small animal applications the range of accelerations obtained is generally lower, seldom higher than 2, mainly due to the use of coils with lower number of elements (4-8 elements)

2.3.2 Techniques exploiting spatiotemporal redundancy

Under this general name we include algorithms that are a step beyond classical parallel imaging techniques. These strategies are based on parallel imaging combined with intelligent sampling strategies to exploit redundancy not only in the spatial domain but also in the temporal one [35].

The number of techniques using these principles, applied to cardiovascular MR, increased noticeably in the past years. Some of the most well-known reconstruction strategies are UNFOLD [61], TSENSE [62], TGRAPPA [63], k-t BLAST [64], k-t SENSE [64] or k-t PCA[65]. These algorithms outperformed parallel imaging acceleration rates, reaching acceleration factors up to 8, in average.

The way spatiotemporal resolution is exploited in these algorithms is pretty close to the compressed sensing philosophy; and some of the above-mentioned algorithms have been slightly modified leading to compressed sensing algorithms, as is, for example, the case of k-t SPARSE-SENSE [66] and k-t FOCUSS [67, 68].

2.3.3 Compressed sensing

Compressed Sensing applied to MRI was first proposed by Michael Lustig et al. [51, 52], and revolutionized acceleration concepts in MRI, as evidenced by the great amount of works developed under the compressed sensing framework in the past years.

Compressed sensing stands on three requirements; the existence of a certain transform domain in which our image has a sparse representation, the use of undersampling patterns that produce incoherent aliasing artifacts in the sparsifying transform representation, and the use of a non-linear reconstruction algorithm. Incoherent (noise-like) artifacts can be achieved by using random or quasi-random undersampling patterns (Figure 2.5). The non-linear reconstruction method has to enforce both the sparsity of the image representation and the consistency of the reconstruction with the acquired data [51].

In dynamic MRI, compressed sensing can exploit the spatiotemporal redundancy of the images under study. The degree of benefit that compressed sensing may provide to different applications will depend, among other factors, on the nature of the data and on the degree of redundancy that can be exploited with different sparsifying transforms. Higher redundancy implies higher sparsity, which will generally imply that higher acceleration factors can be

achieved. Cardiovascular MR has been one of the areas were compressed sensing has been more fruitful in the past years. Cardiac cine [67, 69-72], cardiac perfusion [73, 74] or angiography [75-77] have been profusely investigated and many reconstruction strategies have been proposed, achieving acceleration factors in the range 6-12. Recently, some of the acceleration algorithms proposed in literature combined principles from parallel imaging and compressed sensing, associating concepts of sparsity with joint information from different elements of a phased coil array [78, 79] [80] [81].

However, despite all the progress made in the area, compressed sensing has not reached a full clinical applicability yet. There exist some encouraging works reporting promising results in terms of the clinical applicability of the technique [82-84] but there is still a long way to go. This is due, in part, to the particularity of the compressed sensing artifacts, which are not yet completely characterized from a clinical point of view. Moreover, there is a general lack of practical works, with real implementations of compressed sensing sequences and systematic clinical evaluations.

Regarding the two cardiovascular MR applications addressed in this thesis, we believe that they can greatly benefit from the application of compressed sensing. In the case of cardiac cine sequences, there is a wide range of works exploring the potential of compressed sensing to the acquisition of cardiac cines in humans, reporting excellent acceleration factors. However, the applicability of compressed sensing in small-animal cardiac sequences has not been widely explored [4, 8-11], and only a very recent study has addressed the use of retrospective self-gated cine sequences [10], reporting an acceleration factor of 3.

With regard to the second cardiovascular application explored in this thesis, the visualization of atherosclerotic plaques in coronary arteries in humans is a novel application that is not technically feasible yet. Nevertheless, we believe that compressed sensing and other acceleration techniques can help to increase the feasibility of the technique, reducing acquisition time, improving image quality and relieving resolution, SNR and motion restrictions. Due to the novelty of the technique, there are no previous references that could indicate feasible acceleration rates for this application.

3. Fundamentals of compressed sensing

3.1 The relevance of compressed sensing

The emergence of the compressed sensing theory around 2004 had a great impact in sampling theories and related fields. Traditionally, sampling theories were governed by the Nyquist-Shannon theorem that states the precise sampling rate, expressed in terms of the signal bandwidth, required to recover a band-limited continuous signal.

The idea of compressed sensing was firstly introduced around 2004 by Candès, Romberg, Tao and Donoho [85-88]. In their works they considered the problem of recovering a signal from an incomplete number of samples by solving a convex optimization problem, provided that the signal is sparse in a certain domain. In addition, they also showed that compressed sensing is mainly applicable to cases with a high degree of incoherence between the sampling and the sparsifying basis. They deepened in the mathematical description of the compressed sensing problem, its quantitative understanding and the analysis of the problem requirements.

In plain terms, compressed sensing stands on the three requirements mentioned: 1) The existence of a certain transform domain in which our signal has a sparse representation, 2) the incoherence between the sampling and the sparsifying operators and 3) the use of a non-linear reconstruction algorithm.

The idea of recovering a signal from an incomplete number of samples, lower than what traditionally was considered as required, surpassed the limits of sampling theories and revolutionized innumerous fields such as applied mathematics, electrical engineering, signal detection, image processing etc. Among other areas, in medical imaging the impact of compressed sensing was particularly notorious. The compressible nature of medical images and the great potential benefits that compressed sensing provides to medical imaging turned compressed sensing into one of the most active areas of research in medical imaging in the past years.

In MR, the application of compressed sensing was firstly introduced by Mikael Lustig around 2007 [51, 52]. In MR, data redundancy is generally exploited by applying a certain sparsifying transform to the images. Also, images are undersampled during the acquisition in a random way, in such a way that this undersampling would produce incoherent (noise-like) artifacts in the images. Under these premises, MR images can be recovered using non-linear reconstruction algorithms as it is explained in this chapter.

3.2 Formulation for the problem

As mentioned before, compressed sensing aims to reconstruct a certain sparse signal (image) u from a subset of undersampled measurements f. In the particular case of MR, the image we aim to reconstruct and the measurements performed are related by the Fourier transform F, such that $Fu = f$. Reconstructing the images from an incomplete number of measurements (from the Nyquist point of view) is an ill-posed problem with infinite solutions, that cannot be solved directly. To restrict the solution of this problem, we add as a prior information the fact that our signal is sparse. A signal can be called *s*-sparse if at most *s* of its entries are non-zero

$$\|u\|_0 \leq s \qquad [3.1]$$

Thus, the solution of the reconstruction problem is restricted in the following way

$$\min_u \|u\|_o \text{ such that } Fu = f \qquad [3.2]$$

L0-norm minimization is not a convex optimization problem, it is an NP-hard problem, what makes the problem to solve computationally intractable. Alternatively, we can replace this L0-norm minimization by an equivalent convex relaxation L1-norm

$$\min_x \|u\|_1 \text{ such that } Fu = f \qquad [3.3]$$

This L1-norm based optimization problem can be solved with basis pursuit approaches using linear programming. However, despite its high efficiency, basis pursuit has a polynomial runtime, which is not desirable. Greedy algorithms are a good alternative to solve this L1-norm problem. Greedy algorithms are based on thresholding and iterative recovery of signal components, and yield similar reconstructions but requiring less computational resources [89]. Among others, they are noteworthy OPM (Orthogonal Matching Pursuit) [90], and IHT (Iterative Hard Thresholding algorithm) [91].

In the context of MR, L1-minimization implies that the image is sparse in the pixel domain, which is not generally true (just for a few applications, e.g., angiography). As an alternative, we can introduce an sparsifying transform, Ψ, in equation [3.3]. Taking into account the noise of the data, the compressed sensing problem to be solved in MR can be written as:

$$\min_u \|\Psi u\|_1 \text{ such that } \|Fu - f\|_2^2 < \sigma^2 \qquad [3.4]$$

The first term of the equation is meant to enforce the sparsity, while the second one enforces the data consistency.

Nowadays, there are some emerging alternatives to the L1-norm minimization, as is the case of including a nuclear norm term meant to exploit the low rankness of the data [74, 92].

Nevertheless, in this thesis we have focused on solving the L1-L2 minimization problem stated in equation [3.4] by using several sparsifying transforms.

In order to choose a proper reconstruction algorithm to solve this problem, it is important to take into account the nature of the data, the speed of convergence and runtime of the algorithm, its robustness against noise and its ability to converge to the right solution with very few measurements. Numerous algorithms have been explored in the context of MR: OMP [89], Split Bregman [34], FOCUSS [68], ISD [93], among many others.

3.2.1 Sparsifying transforms

Sparsifying transforms play an important role in the compressed sensing reconstruction. Among other factors, the acceleration that can be achieved with compressed sensing will depend on the degree of sparsity of our data. The nature of the data and its dimensions are key to choose the proper sparsifying transform. Different transforms have been proposed in the literature, such as wavelets transforms, discrete cosine transforms, finite differences, dictionary based representations, etc. In this thesis we used Total Variation (TV) as sparsifying transform because of its robustness and denoising properties [94].

Total Variation

TV is a functional widely used as regularizing tool in image processing, for denoising, deconvolution, texture processing, image analysis and other applications [95]. The TV functional is defined as follows:

$$TV(u) = \int_{\Omega} |\nabla u| \qquad [3.5]$$

Where ∇u denotes the gradient of u. In the discrete case the definition is

$$TV(u) = \|\nabla u\|_1 = \sum_i |\nabla u_i| \qquad [3.6]$$

Isotropic and anisotropic TV

Being u a bidimensional variable (an image), two different definitions of TV can be applied: isotropic and anisotropic TV. TV is defined isotropic if the L2-norm is applied, and anisotropic if the L1-norm is applied instead [96]. Thus, for the isotropic case the TV term remains:

$$TV(u) = \sum_{i,j} \sqrt{(\nabla_x u)_{i,j}^2 + (\nabla_y u)_{i,j}^2} \qquad [3.7]$$

while in the anisotropic case is defined as

$$TV(u) = \|\nabla_x u\|_1 + \|\nabla_y u\|_1 = \sum_{i,\mathrm{j}} |\nabla_x u_{i,j}| + |\nabla_y u_{i,j}| \quad [3.8]$$

Temporal TV

In image processing, TV is generally applied in spatial dimensions. However, in the case of dynamic applications, (as is the case of the work developed in chapter 4) besides the two spatial dimensions, the data have an additional third dimension, the temporal dimension. Thus, for that type of data we have defined the concept of temporal TV (TTV), applied over time

$$TTV(u) = \sum_{i,j,k} |\nabla_t u_{i,j,k}| \quad [3.9]$$

To solve the problem posed in chapter 4, TV was chosen as isotropic in plane and anisotropic with relation to space-time. Thus the global definition of TV remained

$$\|(\nabla_x u, \nabla_y u)\|_1 + \|\nabla_t u\|_1 = \sum_{i,j,k} \sqrt{(\nabla_x u)^2_{i,j,k} + (\nabla_y u)^2_{i,j,k}} + \sum_{i,j,k} |\nabla_t u_{i,j,k}| \quad [3.10]$$

3.3 Split Bregman methodology

Split Bregman is the methodology chosen to solve the compressed sensing problem in this thesis. Split Bregman is an efficient way of solving constrained optimization problems involving L1 and L2-functionals. This methodology states an efficient way of solving an equivalent problem in which L1 and L2-functionals are decoupled and the problem is solved by alternative minimization.

The aim of this section is to introduce the key concepts required for the understanding of the Split Bregman methodology. A more detailed mathematical development can be found in the work from Goldstein and Osher [94], as well as a description of the algorithm's pseudocode. Also, a basic code implementation can be found in the following webpage: http://tag7.web.rice.edu/Split_Bregman.html. The formulation and the code mentioned have been the basis for all the Split Bregman solutions developed and implemented in this thesis.

3.3.1 Bregman iteration

Bregman iteration is a concept originated in functional analysis for finding extrema of convex functionals [94, 97]. It has been used to solve a wide variety of constrained optimization problems in image processing and medical imaging [98-102].

This section is focused on the particular case of using Bregman methodology to solve the compressed sensing problem in MR, using TV as sparsifying transform. The constrained optimization problem we aim to solve is as follows

$$\min_u \ \|\nabla u\|_1 \quad \text{such that } Fu = f \qquad [3.11]$$

This problem has two terms which correspond to the L1-minimization and the data constraint, respectively. This constrained problem is computationally hard to solve but it can be approximated by an equivalent unconstrained problem applying the Bregman iterations. If we apply the Bregman iteration to the data constraint term in equation [3.11] we obtain the following iterative formulation

$$\begin{aligned} u^{k+1} &= \min_u \ \|\nabla u\|_1 + \frac{\lambda}{2} \|Fu - f^k\|_2^2 \\ f^{k+1} &= f^k + f - Fu^k \end{aligned} \qquad [3.12]$$

This unconstrained problem is equivalent to the one in equation [3.11]. In the Bregman formulation restrictions are imposed iteratively; adding the error back in the data constraint [94]. This problem converges in a L2-norm sense for large values of k, and the iterates u^k will get close to a solution of the original constrained problem.

The L1-minimization term present in the compressed sensing formulation of the problem is non-differentiable and thus difficult to solve. Bregman iterations can be also applied to solve this type of L1-regularization problems. If we aim to solve a non-differentiable problem as follows

$$\min_{u,d} \ |d| + H(u) \text{ such that } d = \nabla u \qquad [3.13]$$

By applying Bregman iteration we obtain the equivalent update rule

$$\begin{aligned} (u^{k+1}, d^{k+1}) &= \min_{u,d} \ |d| + \mathrm{H}(u) + \frac{\lambda}{2} \|d - \nabla u - b^k\|_2^2 \\ b^{k+1} &= b^k + \nabla u^{k+1} - d^{k+1} \end{aligned} \qquad [3.14]$$

3.3.2 Split Bregman applied to the compressed sensing problem

In the previous section it was shown how to apply Bregman iteration to convex optimization problems. The compressed sensing problem has two constraints, data constraint and L1-minization constraint, that can be both solved using Bregman iteration.

$$\min_u \ \|\nabla u\|_1 \quad \text{such that } \|Fu - f\|_2^2 < \sigma^2 \qquad [3.15]$$

If we apply the Bregman iteration into the data constraint, we obtain equation [3.12]. To solve the L1-minimization we introduce and auxiliary variable $d = \nabla u$

$$\begin{aligned} u^{k+1} &= \min_{u,d} \ \|d\|_1 \ + \frac{\lambda}{2} \ \left\|Fu - f^k\right\|_2^2 \ \text{such that } d = \nabla u \\ f^{k+1} &= f^k + f - Fu^k \end{aligned} \qquad [3.16]$$

If we apply now Bregman iterations as in equation [3.14] we obtain the update rules of equation [3.17]. This way, the L1 and L2 portions of the problem have been "split", u and d are decoupled and the problem can be solved in an effective way minimizing iteratively with respect to u and d separately

$$\begin{aligned} u^{k+1} &= \min_{u} \ \frac{\mu}{2} \ \left\|Fu - f^k\right\|_2^2 \ + \frac{\lambda}{2} \ \left\|d^k - \nabla u - b^k\right\|_2^2 \\ d^{k+1} &= \min_{d} \ |d| \ + \frac{\lambda}{2} \ \left\|d \ - \nabla u^{k+1} - b^k\right\|_2^2 \\ b^{k+1} &= b^k + \nabla u^{k+1} - d^{k+1} \\ f^{k+1} &= f^k + f - Fu^k \end{aligned} \qquad [3.17]$$

Solution of u

The optimization problem that we must solve now for u^{k+1} is differentiable and has analytical solution. If we differentiate with respect of u and set the result equal to zero, we obtain

$$\left(\mu F^T F + \lambda \nabla^T \nabla\right) \cdot u^{k+1} = \mu F^T f^k + \lambda \nabla^T \left(d_x^k - b_x^k\right) \qquad [3.18]$$

$$K \cdot u^{k+1} = rhs^k \qquad [3.19]$$

This linear system can be solved in the image domain or in the Fourier domain, as proposed in [94, 96]. Solving the problem in the Fourier domain might reduce the computational burden of the problem, but it can only be used if the operators involved have a representation in the Fourier domain. In Chapters 4 and 5 equation [3.19] have been solved in the Fourier domain, while the algorithm in Chapter 7 was solved in the image domain using a Krylov solver.

Solution of d

The optimal value of d can be found using shrinkage operators. A shrinkage operator is a soft thresholding defined as follows [94, 101]

$$\min_d \|d\|_1 + \frac{\lambda}{2}\|d - f\|^2$$
$$\text{shrink}(f, 1/\lambda) = \frac{f}{|f|} * \max\left(|f| - 1/\lambda, 0\right) \quad [3.20]$$

This solution can be easily verified. If we assume $\Theta(d) = \|d\|_1 + \frac{\lambda}{2}\|d - f\|^2$ by differentiating it equating to 0, we obtain $\Theta'(d) = \frac{d}{|d|} + \lambda(d - f) = 0$. The shrinkage can be verified just by substituting the following solution $d = d^*$

$$d^* = \begin{cases} \left(|f| - 1/\lambda\right)\frac{f}{|f|} & if \quad |f| > 1/\lambda \\ 0 & if \quad |f| \le 1/\lambda \end{cases} \quad [3.21]$$

Thus, the particular d subproblem in equation [3.17] can be solved with the following shrinkage operation

$$d^{k+1} = \text{shrink}(\nabla\left(u^{k+1}\right) + b^k, 1/\lambda) \quad [3.22]$$

3.4 An illustrative example

To illustrate the way Split Bregman solves the compressed sensing problem, the Shepp-Logan phantom [103] of size 256x256 was used to perform a compressed sensing reconstruction. To characterize the evolution of the reconstruction under real circumstances, Gaussian noise was added to the phantom. After that, data were undersampled following the random undersampling pattern illustrated in figure 3.1, such that only 30% of the original data were maintained.

Figure 3.1 shows the original Shepp-Logan phantom and a detail of the image used as reference to evaluate the Split Bregman reconstruction. If we undersample our data and then just fill with zeros the non-sampled data and perform a standard Fourier reconstruction, the effects of the random undersampling can be noticed as unstructured artifacts in the image. These artifacts are successfully removed with the Split Bregman reconstruction. To better observe the behavior of the system, Split Bregman parameters were chosen such that they provided slow convergence, $\lambda = 1, \mu = 0.01$. A total of 15000 iterations were used, recovering the image shown in figure 3.1 in 285 s with a relative error of 0.048. It is important to mention that a faster convergence can be obtained increasing the value of μ. Also, a perfect reconstruction can be achieved in absence of any additional noise in the data, in only 18 s.

Figure 3.1 also shows the evolution of the reconstruction error with the number of iterations, it is obvious how the error decreases fast in the first iterations, slowing down its evolution until the best solution is reached; and after that, a slight increase in the error appears. This error evolution coincides with three different stages in the reconstruction. In the first iterations the background in the image is recovered (fast error decrease). Later, the details of the image start being recovered (slower error decrease) and the algorithm converges at 7000 iterations. In the last iterations the solution is over-adjusted (increase in the error after 10000 iterations).

To better comprehend the way Split-Bregman solves this problem, there are two key steps to be understood, the role of the K operator and the evolution of the shrinkage's outcome.

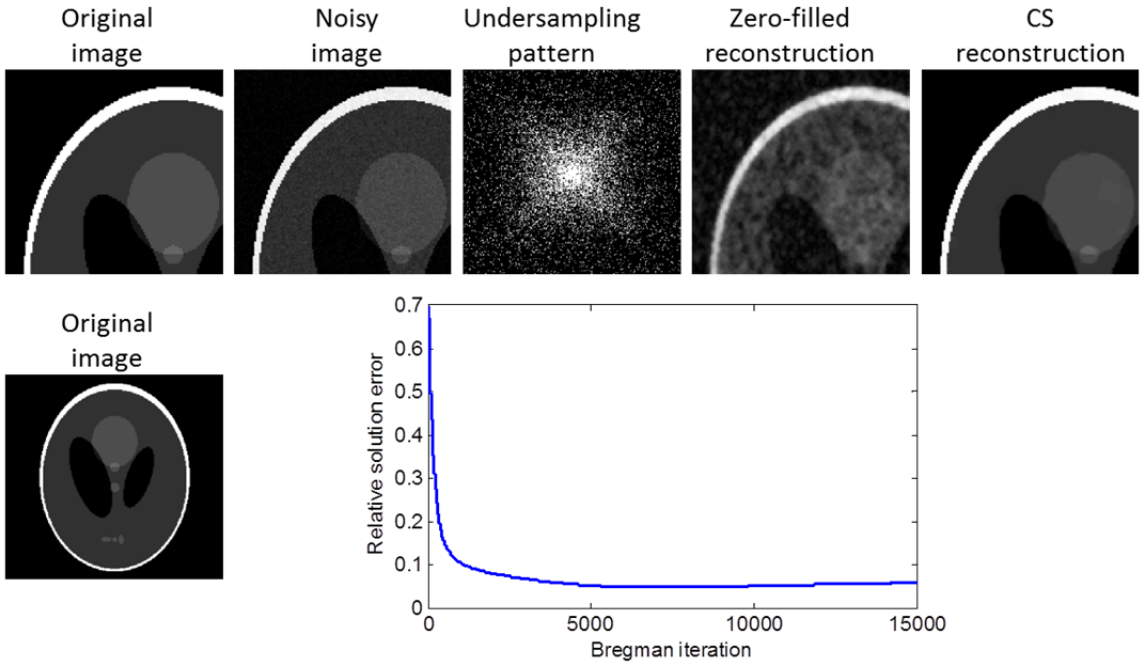

Figure 3.1. Details of the Shepp-Logan phantom under different circumstances of noise and undersampling. Unstructured artifacts present in the images due to the random undersampling are successfully removed in the compressed sensing reconstruction, in which the image is recovered with very low error

K operator

For each iteration, k, equation [3.19] is solved. In this equation the K operator provides a smooth version of the rhs term, which is proportional to the zero-filling reconstruction of the acquired data. The filtering role of this K operator can be easily appreciated in the first iterations of the algorithm, where u^k is clearly a smoother version of the rhs^k term, this is the effect of the L2-norm, as shown in figure 3.2.

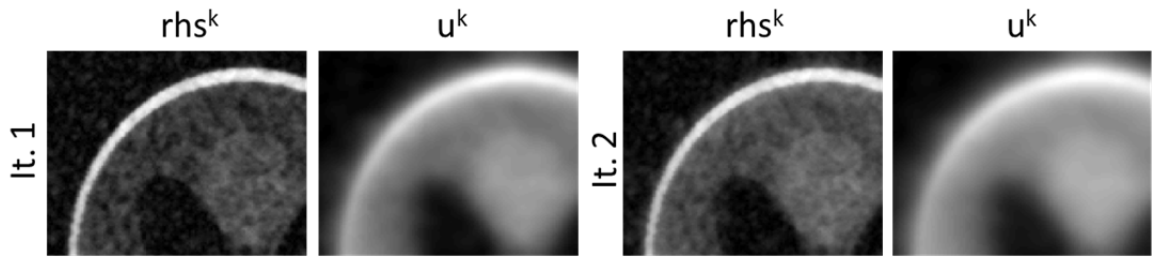

Figure 3.2. Details of u^k and rhs^k for the first two iterations of the Split Bregman reconstruction

Shrinkage operator

To understand how the convergence of the solution is reached by the Split Bregman algorithm is essential to understand the role of the shrinkage operator. Figure 3.3 shows the solution, u^k, and the result of the shrinkage, d^k, for different iterations. For simplicity, only x-related variables are presented, but results are analog in the y-direction.

During the first iterations of the algorithm, the recovered object is very smooth, only the contrast in the image is recovered; there are no details in the images obtained. This situation corresponds with the iterations in which the outcome of the shrinkage operator is zero, so we are basically observing the effect of the operator K in u^k. As the number of iterations increases, a higher amount of information pass the threshold provided by the shrinkage operator, this information is incorporated in the next iteration, u^{k+1}, and the details of the image start being recovered. This is the effect of the L1-norm.

In our example, information starts passing the shrinkage around the 50th iteration. Since that iteration, the details of the images start being recovered until they are almost completely recovered around iteration 2000th. However, if we let the algorithm to continue iterating, an over-adjustment of the details would be produced. In the latest iterations the noise has been adjusted, what does not correspond to the desirable solution. The best solution was provided at an intermediate number of iterations.

The understanding of the role of the K and shrinkage operators, and the way Split Bregman reaches the best solution, can also help to the proper selection of the algorithm's parameters. In a first approximation, Split Bregman parameters can be chosen such the behavior explained in this section is ensured; later, μ can be readjusted for a faster convergence of the solution.

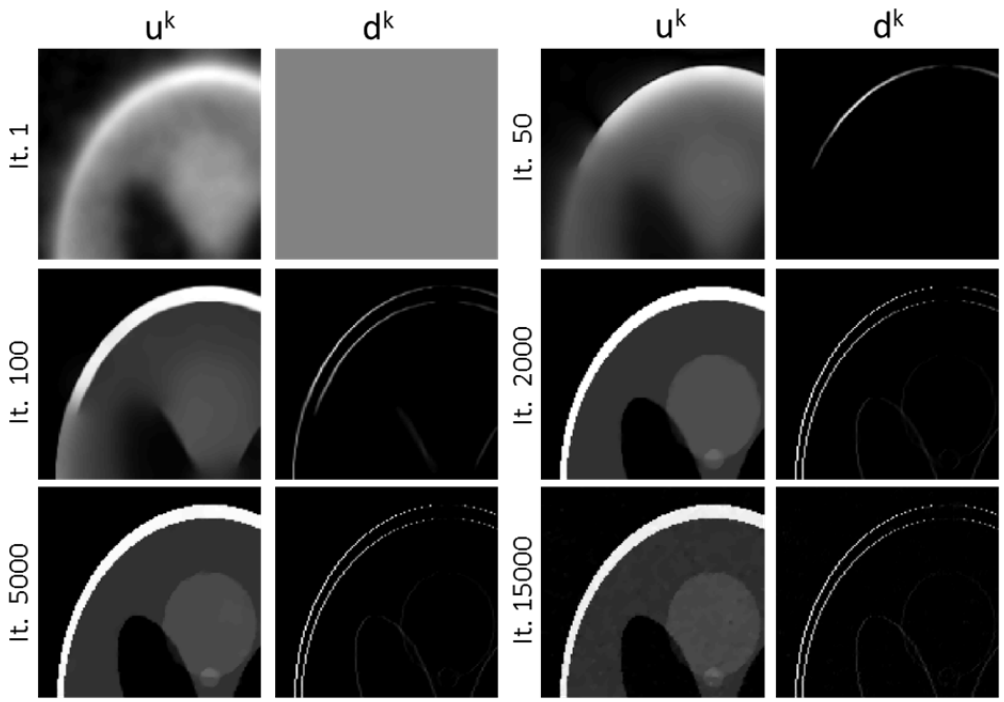

Figure 3.3 Solution u^k and the outcome of the shrinkage d^k for different Bregman iterations

4. Application of the compressed sensing technique to self-gated cardiac cine sequences in small animals

4.1 Introduction

Cardiac cine MRI sequences are widely used to assess cardiac function, evaluate heart motility, and quantify ejection fraction, both in clinical and preclinical applications. These cine sequences can use prospective or retrospective gating. With prospective gating, the ECG signal is used to synchronize image acquisition with the cardiac cycle, while the respiration signal is used to avoid motion artifacts by interrupting the acquisition at specific moments of the respiratory cycle. One drawback of prospective gating is that the use of electrodes at high fields is challenging and prone to artifacts, particularly in small-animal studies. Retrospective cardiac gating obviates the need for ECG by means of a continuous acquisition that is retrospectively sorted into different cardiac phases based on navigator echoes that allow generating cardiac and respiratory synchronism signals. IntraGateFLASH [30] is a self-gated FLASH (Fast Low Angle Shot), an example of a self-gated fast gradient echo sequence, in which a navigator echo is stored with each phase encoding line. According to its corresponding navigator signal, the different phase encodings are retrospectively sorted and averaged in order to arrange a number of complete k-spaces (Fig. 4.1).

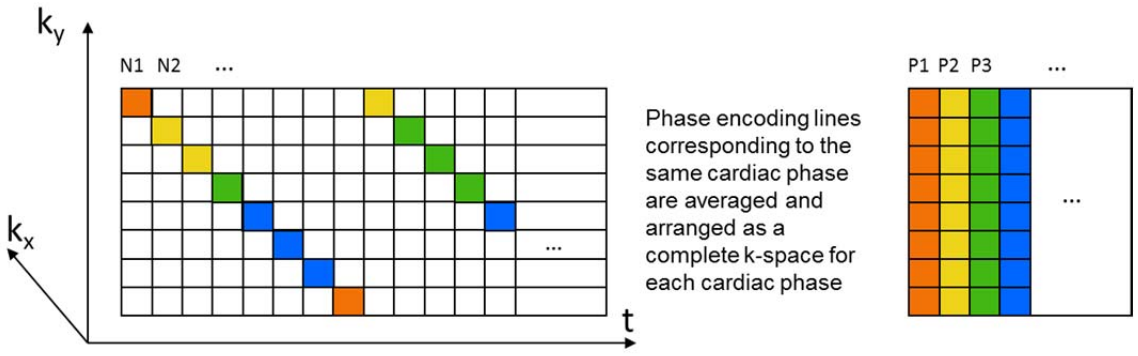

Figure 4.1. IntraGateFLASH acquisition scheme

In cardiovascular applications, acquisition time is directly related to the spatiotemporal resolution and signal-to-noise ratio (SNR) of the reconstructed images. Several acceleration methods enable faster acquisitions (or higher quality images, if acquisition time is maintained). In the last few years, good results for cardiac MRI have been reported with methods such as UNFOLD [61], k-t BLAST and k-t SENSE [64], PARADIGM [104], k-t SPARSE [105], k-t

FOCUSS [67], k-t PCA [65], PSF model based reconstruction [11, 106, 107], k-t ISD [93], and k-t SLR [74]. Many other methods have also been reported [1-7].

The compressed sensing (CS) paradigm states that an exact image reconstruction can be achieved from randomly undersampled data using an appropriate nonlinear approach, if we can assume that the image has a sparse representation in the pixel space or in any other transformed domain [85, 86]. The quality of the reconstruction depends on the degree and type of data undersampling, the degree of image sparsity, and on the particular nonlinear reconstruction algorithm used [51].

Some images may actually be sparse in terms of their spatial representation, as is the case in angiographic studies. In other situations, the most common approach is to use the image gradient as the transform domain. If a sparse solution exists, it can be found by minimizing the L1 norm of the image gradient, also known as total variation (TV). In dynamic applications (where a temporal dimension is involved), we can exploit both spatial and temporal sparsity, because consecutively acquired images are expected to show a strong correlation. Hence it is possible to minimize the TV across both the spatial and temporal dimensions, as we propose in this work.

For dynamic applications, the magnitude of the compressed sensing problem could increase considerably and require computationally intensive calculations. Among the wide variety of reconstruction algorithms available, the Split Bregman method and similar procedures [94, 98, 108, 109] have proved to be more computationally efficient than classic optimization methods for solving problems with L1-functionals, especially for the minimization of spatial TV. Although the Split Bregman methodology has already been successfully applied in static MRI images [110-113], the potential advantages of a spatiotemporal approach have not been yet evaluated.

Most previous dynamic compressed sensing approaches to human cardiac MRI focused on prospective cine acquisitions; only two included retrospective classifications [7, 67]. Few previous works are available on small-animal preclinical applications [4, 8-11] and only a very recent study has addressed the use of retrospective self-gated cine sequences [10].

The aims of this chapter are to apply the compressed sensing technique to IntraGateFLASH cardiac MRI studies on rats and to find the maximum acceleration factor achievable with this technique. One of the contributions of this work is to extend the Split Bregman formulation to minimize the TV in both the spatial and the temporal dimensions. In addition, a new framework for analyzing the effect of the undersampling pattern on the achievable acceleration factor is proposed.

4.2 Theory

4.2.1 Compressed sensing and Split Bregman

Compressed sensing formulates the following constrained optimization problem

$$\min_{u} \left\|\Psi u\right\|_1 \quad \text{such that } \left\|\tilde{F}u - f\right\|_2^2 < \sigma^2 \qquad [4.1]$$

where $\left\|\cdot\right\|_1$ is the L1-norm, Ψ denotes the linear operator that transforms the image from the pixel representation into a sparse representation, $\left\|\tilde{F}u - f\right\|_2^2 < \sigma^2$ is the data fidelity term, $\tilde{F}$ represents the undersampling Fourier operator, f represents the measured k-space, u is the image in the pixel representation and σ^2 is the variance of the signal noise. The undersampling Fourier transform can be expressed as the product of a full Fourier operator F and a matrix R, whose role is to select the points of k-space that will be sampled or preserved ($\tilde{F} = RF$).

If we use the spatial derivatives of the images as the transform domain, $\Psi = \nabla$, where $\nabla = (\nabla_x, \nabla_y)$ is the gradient, ∇_x and ∇_y are spatial derivatives, then in Eq. 1 it will be necessary to minimize the TV of the images. Spatial TV can be computed using an anisotropic TV model [94, 96, 100]

$$\left\|(\nabla_x u, \nabla_y u)\right\|_1 = \left\|\nabla_x u\right\|_1 + \left\|\nabla_y u\right\|_1 \qquad [4.2]$$

or using an isotropic TV model [94, 96, 100]

$$\left\|(\nabla_x u, \nabla_y u)\right\|_2 = \sum_{i,j} \sqrt{\left(\nabla_x u_{i,j}\right)^2 + \left(\nabla_y u_{i,j}\right)^2} \qquad [4.3]$$

As L1-based compressed sensing algorithms can be computationally intensive, there is increasing interest in novel algorithms that perform faster reconstructions, such as computationally efficient orthogonal matching pursuit [1], forward-backward splitting methods [3], and first-order approximations [114, 115]. Among these, the so-called splitting methods decouple L1 and L2 functionals and minimize them separately, allowing the L1 subproblem to be efficiently solved using shrinkage formulas and the L2 subproblem to be solved analytically. Bregman iteration technique makes the solution of unconstrained problems to optimally converge to equivalent constrained problems [94, 98, 99, 108]. Based on Bregman iteration method, Split Bregman solves the constrained problem exactly for convex non-differentiable functionals such as TV [94].

4.2.2 Extension of the Split Bregman technique to MRI spatiotemporal models

Based on the inherent similarity between frames in a cine acquisition, we extend the formulation from Eq. [4.1] to minimize the TV both in space and in time [116]. Using an isotropic spatial TV model, we obtain the following constrained optimization problem:

$$\min_{u} \left\|(\nabla_x u, \nabla_y u)\right\|_2 + \left\|\nabla_t u\right\|_1 \quad \text{such that } \left\|RFu - f\right\|_2^2 < \sigma^2 \qquad [4.4]$$

where ∇_t is the temporal derivative (see Fig. 4.2) and $\left\|\nabla_t u\right\|_1$ is the temporal TV.

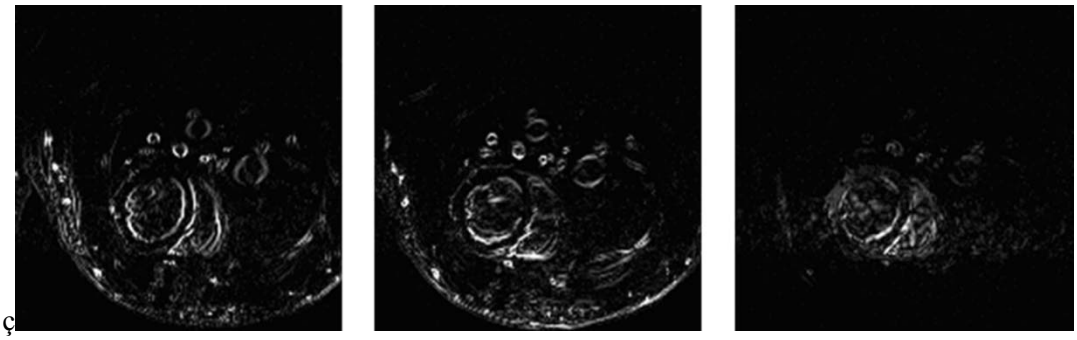

Figure 4.2. Spatial and temporal gradients: from left to right |Dx|, |Dy|, and |Dt|

Taking the spatial formulation introduced by Goldstein [94] as our starting point, we can expand the Split Bregman formulation to both spatial and temporal domains. We introduce the new complex-valued variables d_x, d_y, and d_t that allow the splitting of L1 and L2 functionals. Making the replacements $d_x \leftarrow \nabla_x u$, $d_y \leftarrow \nabla_y u$, and $d_t \leftarrow \nabla_t u$ the problem in Eq. [4.4] is reformulated as:

$$\min_{d_x, d_y, d_t, u} \left\|(d_x, d_y)\right\|_2 + \left\|d_t\right\|_1 \text{ such that } \left\|RFu - f\right\|_2^2 < \sigma^2, \quad d_i = \nabla_i u, \quad i = x, y, t \qquad [4.5]$$

This constrained problem can be solved by using an equivalent unconstrained problem based on Bregman iterations [94]. By applying the Bregman iterations, represented by b_i^k and f^k b_i^k and f^k, the following unconstrained formulation converges iteratively to the constrained problem in Eq. [4.5].

$$\begin{aligned}\min_{d_x, d_y, d_t, u} \left\|(d_x, d_y)\right\|_2 + \left\|d_t\right\|_1 + \frac{\mu}{2}\left\|RFu - f^k\right\|_2^2 + \frac{\lambda}{2}\left\|d_x - \nabla_x u - b_x^k\right\|_2^2 + \\ + \frac{\lambda}{2}\left\|d_y - \nabla_y u - b_y^k\right\|_2^2 + \frac{\lambda}{2}\left\|d_t - \nabla_t u - b_t^k\right\|_2^2\end{aligned} \qquad [4.6]$$

where λ is a constant penalty weighting parameter for the TV constraints and μ is a constant penalty weight parameter for the data fidelity term.

At each iteration k, Bregman iterations define a new problem in which the variables u^k and d_i^k are updated and exactly solved; constraints are imposed by adding the error back into the constraint in each iteration:

$$\begin{aligned} b_i^{k+1} &= b_i^k + \left(\nabla_i u^{k+1} - d_i^{k+1}\right) \\ f^{k+1} &= f^k + f - RFu^{k+1} \end{aligned} \qquad [4.7]$$

For a large number of iterations, and for parameters λ and μ sufficiently small, the constraints are imposed iteratively in a smooth way and the Bregman iterations lead to a sequence of solutions u^k that will get monotonically close to a solution of the original constrained problem, u, while the data fidelity term monotonically decreases to zero [98].

In fact, as long as the weighting parameters are small, and the number of iterations is large, the influence of these parameters is small [94, 99]. Thus, there is no need to carefully optimize the weighting parameters, as opposed to unconstrained optimization problems, where regularization parameters have to be cautiously selected (for example with the L-curve method). This is an additional advantage of the Split Bregman formulation. The most important of these two parameters is μ, that weights the data constraint and thus affects the convergence speed. Higher values of μ speed up convergence, although it must remain sufficiently small to guarantee convergence [99]. Usually λ and μ are chosen empirically [94].

As u and d_i are independent (see Eq. [4.6]), they can be split into two subproblems and solved separately. We address first the solution of u which is obtained by solving the following L2-norm subproblem:

$$u^{k+1} = \min_{u} \frac{\mu}{2}\left\|RFu - f^k\right\|_2^2 + \frac{\lambda}{2}\left\|d_x^k - \nabla_x u - b_x^k\right\|_2^2 + \frac{\lambda}{2}\left\|d_y^k - \nabla_y u - b_y^k\right\|_2^2 + \frac{\lambda}{2}\left\|d_t^k - \nabla_t u - b_t^k\right\|_2^2 \qquad [4.8]$$

As this subproblem is differentiable, by differentiating with respect to u u u and setting the result equal to zero, we obtain the update rule,

$$K \cdot u^{k+1} = r^k \qquad [4.9]$$

where

$$K = \left(\mu F^T R^T RF + \lambda \nabla_x^T \nabla_x + \lambda \nabla_y^T \nabla_y + \lambda \nabla_t^T \nabla_t\right) \qquad [4.10]$$

And

$$r^k = \mu F^T R^T f^k + \lambda \nabla_x^T \left(d_x^k - b_x^k \right) + \lambda \nabla_y^T \left(d_y^k - b_y^k \right) + \lambda \nabla_t^T \left(d_t^k - b_t^k \right) \qquad [4.11]$$

Eq. [4.9] can be further simplified by means of $\nabla^T \nabla = -\Delta$ for a definition of ∇ including all the derivatives $\nabla = \left(\nabla_x, \nabla_y, \nabla_t \right)$ $\nabla = \left(\nabla_x, \nabla_y, \nabla_t \right)$ $\nabla = \left(\nabla_x, \nabla_y, \nabla_t \right)$ leading to the following expression:

$$\left(\mu F^T R^T R F - \lambda \Delta \right) u^{k+1} = r^k \qquad [4.12]$$

This involves solution of the linear system in the image domain $K(x,t)u(x,t) = r(x,t)$. This approach is computationally very expensive, as it requires the inversion of a matrix K of size $\left(N_x N_y N_t \right)^2$. To avoid this inversion Eq. [4.12] can be rewritten in the Fourier domain as done in [94, 96], $\hat{K}(k,\upsilon)\hat{u}(k,\upsilon) = \hat{r}(k,\upsilon)$. This only requires a pixel-by-pixel operation of size $N_x N_y N_t$ and three Fourier transforms, two 3D FFT for inverting the linear system and one slice-by-slice 2D FFT to compute the first term of the right-hand side of Eq. [4.11]. The Fourier formulation can only be implemented when all the mathematical operators in Eq. [4.12] have a Fourier representation. In our case, since all the derivative operators are analytical functions in the Fourier domain, we can take advantage of working in the Fourier domain and thus substantially reduce the computational burden of the problem. While the previous Fourier formulation has been shown to be computationally efficient in 2D [94], the present study is the first to show the greater benefit obtained in 3D problems.

The Fourier 3D formulation can be implemented by representing all variables and mathematical operators in 3D (size $N_x N_y N_t$) and solving Eq. [4.12] as

$$u^{k+1} = F_{3D}^{-1} \left[F_{3D}(r^k) \Big/ \hat{K}_{3D} \right] \qquad [4.13]$$

where $\hat{K}_{3D}$ in the Fourier domain is represented as

$$\hat{K} = \mu R - \lambda \hat{\Delta}_{3D} \qquad [4.14]$$

where R represents $F^T R^T R F$ in the Fourier domain and $\hat{\Delta}_{3D}$ is the 3D spatial Laplacian operator in the Fourier domain. $\hat{\Delta}_{3D}$ can be implemented by taking a 3D FFT of the discrete Laplacian kernel written in the following form:

$$\text{first plane} = \begin{pmatrix} 0 & -1 & 0 \\ -1 & 6 & -1 \\ 0 & -1 & 0 \end{pmatrix} \quad \text{second plane} = \begin{pmatrix} 0 & 0 & 0 \\ 0 & -1 & 0 \\ 0 & 0 & 0 \end{pmatrix} \quad \text{last plane} = \begin{pmatrix} 0 & 0 & 0 \\ 0 & -1 & 0 \\ 0 & 0 & 0 \end{pmatrix} \quad [4.15]$$

This implementation is an extension from the 2D version of the Split Bregman method provided by Goldstein's code (Split Bregman, http://tag7.web.rice.edu/Split_Bregman.html).

On the other hand, splitting variables d_i can be derived from Eq. [4.6] and solved using generalized shrinkage formulas [96, 108]

$$d_t^{k+1} = \min_{d_t} \|d_t\|_1 + \frac{\lambda}{2}\left\|d_t - \nabla_t u^{k+1} - b_t^k\right\|_2^2 \quad [4.16]$$

$$d_t^{k+1} = \text{shrink}(\nabla_t u^{k+1} + b_t^k, 1/\lambda) \quad [4.17]$$

$$\text{shrink}(x,\gamma) = \frac{x}{|x|} * \max\left(|x| - \gamma, 0\right) \quad [4.18]$$

In the case of d_x^{k+1}, d_y^{k+1} we use an isotropic shrinkage formula

$$(d_x^{k+1}, d_y^{k+1}) = \min_{d_x, d_y} \left\|(d_x, d_y)\right\|_2 + \frac{\lambda}{2}\left\|d_x - \nabla_x u^{k+1} - b_x^k\right\|_2^2 + \frac{\lambda}{2}\left\|d_y - \nabla_y u^{k+1} - b_y^k\right\|_2^2 \quad [4.19]$$

$$d_x^{k+1} = \max\left(s^k - 1/\lambda, 0\right)\frac{\nabla_x u^{k+1} + b_x^k}{s^k} \quad [4.20]$$

$$d_y^{k+1} = \max\left(s^k - 1/\lambda, 0\right)\frac{\nabla_y u^{k+1} + b_y^k}{s^k} \quad [4.21]$$

$$s^k = \sqrt{\left|\nabla_x u^{k+1} + b_x^k\right|^2 + \left|\nabla_y u^{k+1} + b_y^k\right|^2} \quad [4.22]$$

The complete algorithm that solves the constrained optimization problem in Eq.[4.4], for given values of λ and μ, is shown below:

Initialize: $f^0 = f$, and $d_x^0 = d_y^0 = b_x^0 = b_y^0 = 0$

$\hat{K} = \mu R - \lambda \hat{\Delta}_{3D}$

While $\left\| RFu^k - f \right\|_2^2 > \sigma^2$

Loop N times

$$r^k = \mu F^T R^T f^k + \lambda \nabla_x^T \left(d_x^k - b_x^k \right) + \lambda \nabla_y^T \left(d_y^k - b_y^k \right) + \lambda \nabla_t^T \left(d_t^k - b_t^k \right)$$

$$u^{k+1} = F^{-1} \left[\hat{r}^k \Big/ \hat{K} \right]$$

$$d_t^{k+1} = \text{shrink} \left(\nabla_t u^{k+1} + b_t^k, 1/\lambda \right)$$

$$b_t^{k+1} = b_t^k + \left(\nabla_t u^{k+1} - d_t^{k+1} \right)$$

$$s^k = \sqrt{\left| \nabla_x u^{k+1} + b_x^k \right|^2 + \left| \nabla_y u^{k+1} + b_y^k \right|^2}$$

$$d_x^{k+1} = \max \left(s^k - 1/\lambda, 0 \right) \frac{\nabla_x u^{k+1} + b_x^k}{s^k}$$

$$d_y^{k+1} = \max \left(s^k - 1/\lambda, 0 \right) \frac{\nabla_y u^{k+1} + b_y^k}{s^k}$$

$$b_x^{k+1} = b_x^k + \left(\nabla_x u^{k+1} - d_x^{k+1} \right)$$

$$b_y^{k+1} = b_y^k + \left(\nabla_y u^{k+1} - d_y^{k+1} \right)$$

end

$f^{k+1} = f^k + f - RFu^{k+1}$

end

Different values of N were tested, ranging from 1 to 50, where N is the number of iterations of the inner loop in charge of imposing the TV restriction. N=1 proved to be empirically optimum [117].

In conclusion, Split Bregman divides the reconstruction problem into two subproblems: a quadratic problem that is exactly and efficiently solved in the Fourier domain; and a second problem that includes all the L1-norm functionals solved using shrinkage operations. To our knowledge, we presented the first implementation of a compressed sensing method extending the Split Bregman formulation to spatiotemporal domains in dynamic MRI studies.

4.3 Methods

4.3.1 Datasets

The results presented in this chapter were obtained by simulating different undersampling patterns over real acquired data from small-animal MRI studies (rat cardiac cine sequences).

The original datasets were acquired with a 7 T Bruker BioSpec 70/20 scanner using a linear coil resonator for transmission and a dedicated four-element cardiac phased array coil for reception. The IntraGateFLASH sequence used had the following parameters: TE = 2.43 ms, TR = 8 ms, number of total repetitions = 200, number of frames = 8, matrix size = 192x192, FOV = 4.8x4.8 cm, and slice thickness = 1.2 mm. A total of 192x200 correlative phase encodings were acquired in a total time of 5 min 7 s. Although a TR of 8 ms could theoretically lead to 15-16 frame cine movies, the retrospective character of our acquisition allowed us to decide *a posteriori* the number of cardiac frames during the reconstruction process. After several experiments and reconstructions, and based on a reasonable acquisition time and SNR values, we decided that 8 was the optimal number of frames for our study.

After the simulated undersampling patterns were applied to the complete datasets, the phase encodings were retrospectively classified into 8 complete k-spaces, one for each desired time frame. The reconstructions were performed separately for each element of the phased array and subsequently combined with a sum of squares.

Data from six female Wistar rats (weight ranging from 250 g to 350 g) were used for the assessment of feasible acceleration factors: four healthy animals and two animals with surgically-provoked myocardial infarct. Animals were treated according to the European Communities Council Directive (86/609/EEC) and with the approval of the Animal Experimentation Ethics Committee of Hospital General Universitario Gregorio Marañón.

4.3.2 Undersampling pattern

An appropriate selection of undersampling patterns intended for each application is essential. First, it is important to consider the specific timing of the sequence involved. For the IntraGateFLASH sequence, acquisition time is directly proportional to the number of acquired phase encodings; therefore, to achieve a reduction in acquisition time, it is necessary to remove complete phase encoding lines from the acquisition scheme. In addition, a random

undersampling scheme fulfills the requirement of producing incoherent artifacts, as required by the compressed sensing theory [51].

Lustig et al. suggested to make use of quasi-random patterns following a Monte Carlo procedure based on a variable probability density function [51]. By adapting their methodology to the requirements set out above, we created a polynomial probability density function (Eq. [4.23]) that assigned different sampling probabilities to different regions of k-space. Two user-selectable parameters make it possible to choose a number of lines in the center of the k-space, which will always be sampled, and to select the probability decay rate with which the remaining phase encodings will be sampled, as a function of its distance to the center of the k-space (Fig. 4.3-A).

$$\begin{cases} (1-r)^p & if \quad |r| \geq rad \\ 1 & if \quad |r| \prec rad \end{cases} \qquad [4.23]$$

Lustig et al. suggested the use of the TPSF (Transform Point Spread Function) to select appropriate undersampling patterns [51]. Since TPSF measures propagation error, the best patterns are those with a low TPSF. Lustig et al. proposed repeating the generation process several times to create different undersampling patterns and to select that with the lowest TPSF. In our work, we go beyond TPSF criterion, which alone is not robust enough to select good undersampling patterns.

For our IntraGateFLASH application, we tested and compared two undersampling patterns, k_x-k_y and k-t.

k_x-k_y pattern

The k_x-k_y pattern is the simpler of the two. Randomization is performed only in the phase encoding direction (Fig. 4.3-B), and the same phase encoding lines are removed throughout the acquisition period. Thus, this approach is equivalent to applying the same k_x-k_y undersampling pattern to all the final cardiac frames.

Before selecting the undersampling patterns, we tested whether the TPSF criterion alone was adequate for our k_x-k_y patterns. To this end, we generated 500 patterns using a function from Lustig's original undersampling code [51]. Each call to this function generates 10 random patterns and returns the one with the lowest TPSF value. We repeated the call 500 times to produce the 500 undersampling patterns used in our work.

We also tested whether the suitability of the undersampling patterns was independent from the cardiac frame we were working with. Therefore, 50 different patterns were applied over the two most different cardiac frames, namely, those corresponding to the cardiac diastole and systole. The errors obtained over these two different frames were compared.

k-t pattern

In this case, the undersampling pattern applied during the acquisition changes randomly over time, thus making it possible to perform randomization both in the phase encoding and in the temporal dimensions (Fig. 4.3-C). After undersampling, the data are classified according to their navigator signals and averaged into the final cardiac frames; this approach is equivalent to using a different random k_x-k_y pattern (Fig. 4.3-B) for each final frame. Figure 3.1 illustrates how each line of the final k-spaces is the average of a specific number of actually acquired k-space lines; the number of averaged lines depends on the navigator signal, which in turn depends on cardiac movement during acquisition. Therefore, we are only able to establish the undersampling k-t pattern that will be executed during the acquisition, whereas the resultant k_x-k_y patterns obtained after the averaging step cannot be determined in advance.

One advantage of this kind of pattern combined with the IntraGateFLASH sequence is that, thanks to the data averaging step, the percentage of nonzero data in the final k-space of each frame will be higher than the percentage actually applied during acquisition. As an example, one of the undersampling patterns we tested preserved only 15% of the original acquired data; however, after sorting and averaging, the percentage of nonzero data in the eight final k-spaces filled 27% of the eight final frames. Henceforth, the term "data percentage" refers to the percentage of data actually acquired which correlates with the reduction in acquisition time, and does not reflect the final percentage of the k-space that is zero-filled.

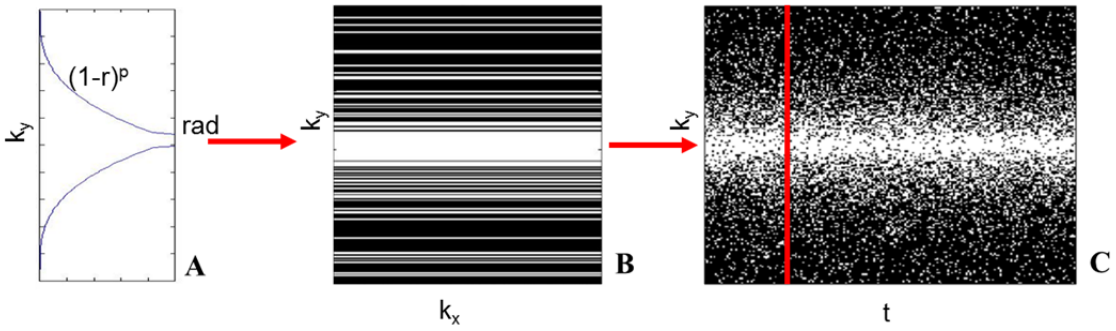

Figure 4.3. A) Probability density function. B) k_x-k_y undersampling pattern. C) k-t undersampling pattern

As in our IntraGateFLASH application the final k_x-k_y undersampling patterns cannot be predicted in advance, the only possibility of optimization is to vary the parameters of the probability density function used to generate the k-t undersampling pattern. We studied the influence of three parameters: the percentage of original data preserved, the exponent of the probability decay rate, and the radius, which defines the number of lines around the k-space center, which will always be fully sampled (Eq.[4.21]). We performed simulations by varying the percentages of maintained original data from 10% to 40%, the exponent ratio from 3 to 9, and the radius (expressed as normalized distance to the center) from 0 to 0.1. These ranges were determined by excluding those values that clearly showed bad results after a coarse assessment of the undersampling patterns.

4.3.3 Maximum acceleration factor achievable

The ultimate goal of this work was to find the maximum acceleration factor achievable for the cardiac cine application using our compressed sensing approach. Different reconstructions using k_x-k_y and k-t undersampling patterns were obtained by maintaining the percentages of the original data from 5% to 40%, in 5% steps.

In order to evaluate the influence of the number of frames (and thus indirectly the influence of the SNR level) on the acceleration factor achievable, the same dataset with k-t undersampling patterns was also reconstructed to give 16 final frames. For our fully-sampled dataset using 16 frames instead of 8 implies an SNR reduction of 1.65 times.

Also, to better understand the benefits of compressed sensing, we compared it to other simple strategies that would also lead to reduced acquisition times. First, we compared compressed sensing reconstructions to simply zero filling the missing k-space lines and performing a standard Fourier transform. We used the same undersampling patterns in both cases, with 10% (R=10) and 7% (R=14%) of the original data. Secondly, we compared compressed sensing reconstruction to a fully-sampled image with a reduced number of accumulated repetitions such the total acquisition time is the same for both strategies. The number of repetitions of the fully-sampled acquisition was thus decreased 10 and 14 times, respectively.

All the tests mentioned above were performed on the four healthy subject datasets. Once the limits of compressed sensing accelerations in healthy animals were established, those accelerations were also evaluated in two animals with myocardial infarct.

All reconstructions were implemented in MATLAB (MathWorks, MA, USA) on a Dell Precision T5500 with Intel Xeon, using 8 CPUs (2.4 GHz and 12 GB RAM). As for the values of the weighting parameters λ and μ, we empirically tested a range from 10^{-2} to 10.

4.3.4 Quality criteria

The following quantitative criteria were used to assess image quality:

1. Reconstruction error, calculated from a region of interest (ROI) of 120x120 pixels around the heart, referenced to the fully sampled image

$$error = \frac{\sqrt{\sum_{i,j}\left| I_{\substack{rec \\ i,j}} - I_{\substack{full \\ i,j}} \right|^2}}{\sqrt{\sum_{i,j}\left| I_{\substack{full \\ i,j}} \right|^2}} \qquad [4.24]$$

2. Intensity profiles from an interface region over the myocardium (Fig. 4.9)
3. Presence of artifacts and temporal blurring in the images-
4. To assess temporal blurring, we calculated the mean value over time of a 5x5 pixel ROI and represented a y-t intensity profile containing both blood and myocardium (Fig. 4.10).
5. Impact of compressed sensing acceleration on representative functional heart measurements [118]. Specifically, the following single-slice measurements were performed:
   - Percentage difference between end-diastolic and end-systolic volumes

$$\%\ volume\ difference = \frac{EDV - ESV}{EDV} \qquad [4.24]$$

   where EDV and ESV are the end-diastolic and end-systolic volumes respectively
   - The left ventricle mass measured in diastole

$$Slice\ mass = \rho * (Epicardium\_area - Endocardium\_area) * slice\_thickness \qquad [4.24]$$

   ρ=1.055 g/cm^3 is the estimated density of the myocardium.
6. Finally, image quality was qualitatively assessed by an experienced cardiac MRI specialist who was blind to the method used.

The complete analysis described above was performed on the first small-animal dataset analyzed. Based on these quality criteria, a range of compressed sensing acceleration factors

was determined as feasible. To verify its reproducibility, those acceleration factors were also tested on the total of six small-animal datasets and the above-mentioned functional measurements were performed. All the hearts were manually segmented by an experienced specialist.

To define an acceptance range for these functional parameters, we firstly estimated the intraobserver variability for the healthy subjects through the standard deviation of three measurements obtained from the fully-sampled image of the first animal analyzed. The acceptance range was defined as ±2 intraobserver standard deviations from the fully-sampled values (roughly, the 95% confidence interval). .

4.4 Results

The following solutions were obtained using $\lambda = 1$ and $\mu = 4$, values that appeared to be empirically optimal.

4.4.1 Undersampling pattern

k_x-k_y pattern

Figure 4.4 shows the relative reconstruction error yielded by the 500 patterns with low TPSF. The positive skewness of the histogram (0.71) suggests that most of the randomly generated patterns lead to low reconstruction errors. However, 24% led to an error greater than 0.17, which we considered too high.

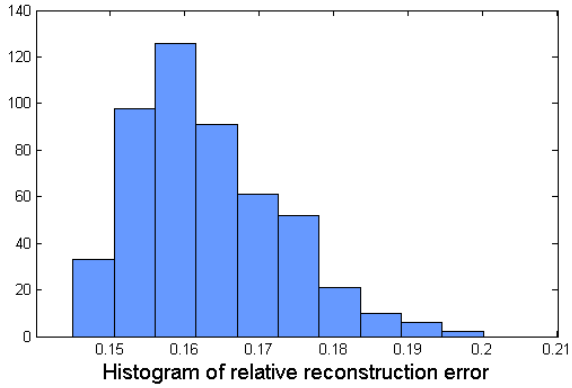

Figure 4.4. Histogram of the reconstructed error of 500 random patterns, maintaining 20% of the original data

Figure 4.5 shows the relative reconstruction errors of the 50 patterns measured over the systolic and diastolic frames. Although these frames differ in the image domain, they show a similar

trend in the reconstruction error, thus indicating that the selection of optimal patterns is frame-independent.

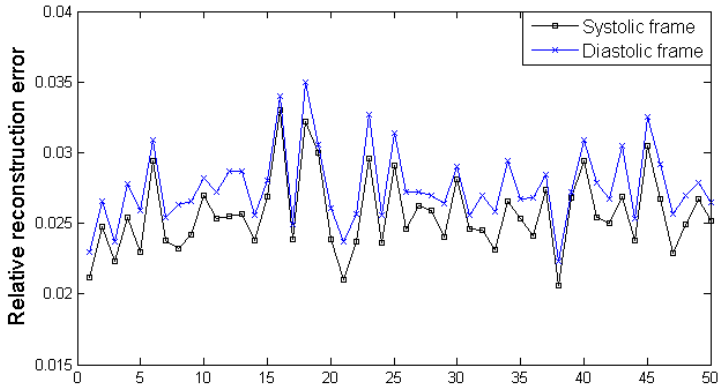

Figure 4.5. Reconstruction error using 50 different single-frame patterns in systolic and diastolic frames

k-t pattern

Figure 4.6 shows relative reconstruction errors expressed as a function of the three eligible parameters of the probability density function implemented, namely, the percentage of original data preserved, the decay exponent, and the radius. The reconstruction error does not change significantly with the exponent or the radius. The results seem to depend mainly on the percentage of data, as long as we choose reasonable values for the other parameters (not a large radius for example).

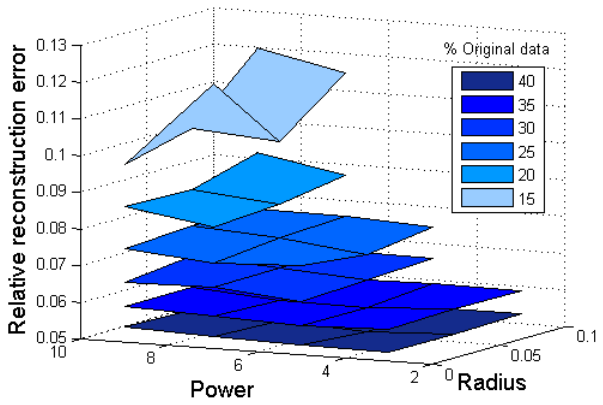

Figure 4.6. Relative reconstruction error as a function of the percentage of original data maintained, the decay exponent, and the radius.

4.4.2 Maximum acceleration factor achievable

Figure 4.7 shows the mean squared error of reconstructed images calculated over a ROI around the myocardium for different acceleration factors and undersampling pattern types.

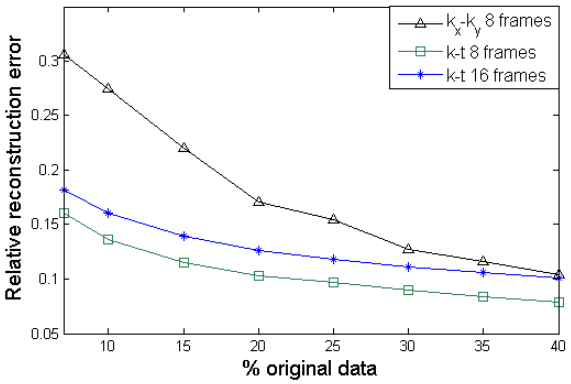

Figure 4.7. Mean squared error as a function of the percentage of original data maintained

The end of systole frame corresponding to the maximum acceleration factors (preserving good quality image) of each pattern type are presented in figure 4.8. compressed sensing reconstructions for 16 frames datasets are also shown in the last raw of figure 4.8. All images have the same scale but difference images are displayed with an amplification factor of 5 in order to make more conspicuous the differences and the presence of artifacts.

Figure 4.8 shows compressed sensing reconstructions maintaining 30% (R=3.3) and 20% (R=5) of the original data, using k_x-k_y undersampling patterns. Beyond these accelerations, image quality was inadequate. Images with R=3.3 shows good quality and only small differences are present in the border of the myocardium. However, for R=5 some details of the image are missing, reconstruction is slightly blurred and artifacts appeared in the myocardium tissue, as the difference image shows.

In the case of k-t undersampling types, we can obtain higher accelerations. Reconstructions preserving 10% (R=10) and 7% (R=14) of the original data are displayed for both 8 and 16 frames. Image quality for R=10 is good, myocardium is well defined, high frequency information is preserved and there are no noticeable artifacts. For R=14, images are slightly blurred, although a good delineation of the myocardium is still possible for both 8 and 16 frames.

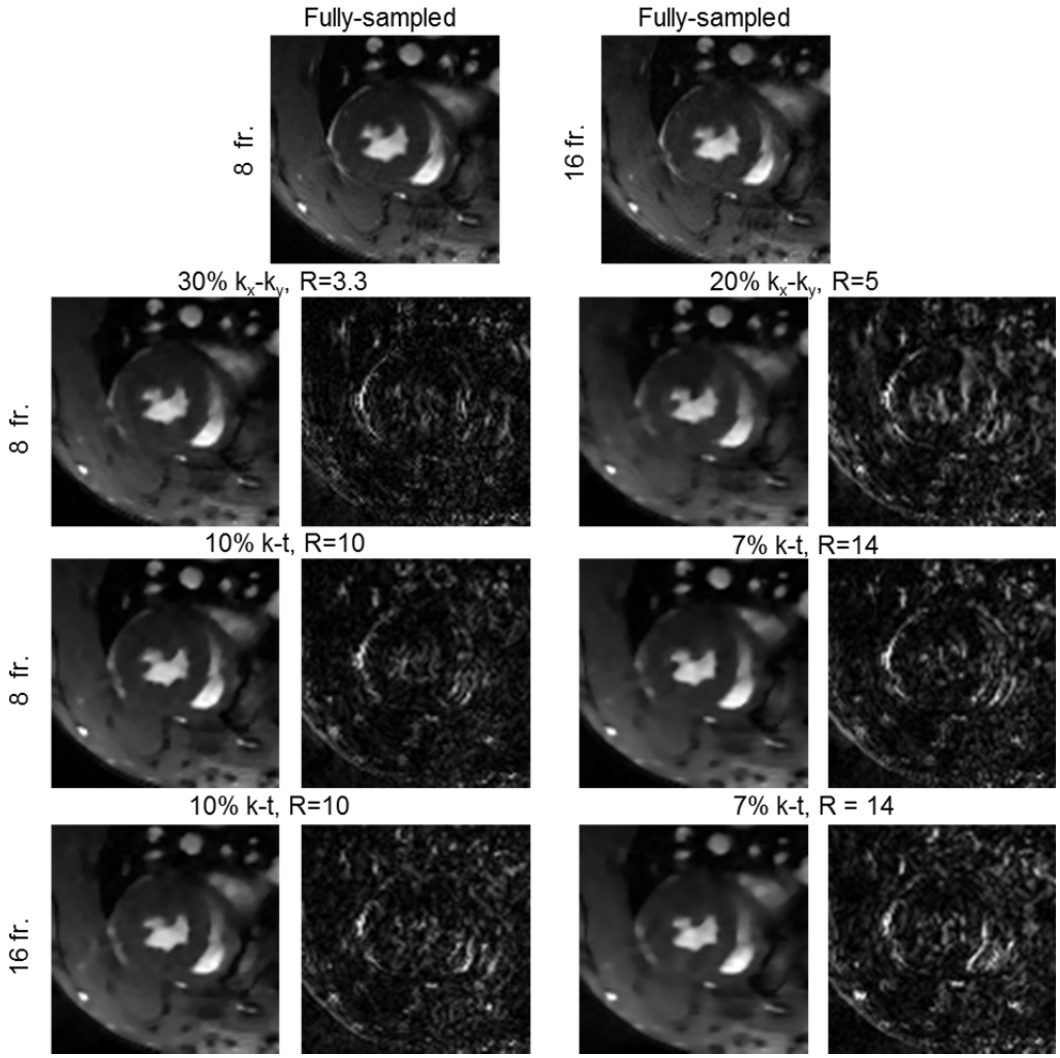

Figure 4.8. Reconstructed and difference images (with an amplification factor of 5) for different undersampling patterns, acceleration factors (R) and different number of frames. End of systole frame is shown.

Figure 4.9 shows compressed sensing results compared with other acceleration strategies at similar acquisition times. As mentioned before, the use of random undersampling causes the apparition of incoherent artifacts in the image domain. These unstructured artifacts are present in the zero-filled reconstruction; however it is easily appreciated how those artifacts are completely removed when performing the proposed compressed sensing reconstruction. On the other hand, the fact of reducing the number of repetitions to decrease the total acquisition time has a complete different effect. In this case, less data are acquired and averaged; this implies lower signal intensity and also the presence of motion artifacts, as we can notice in the difference images. The only acceleration strategy that offers good quality results, without motion or incoherent artifacts, is the proposed compressed sensing methodology.

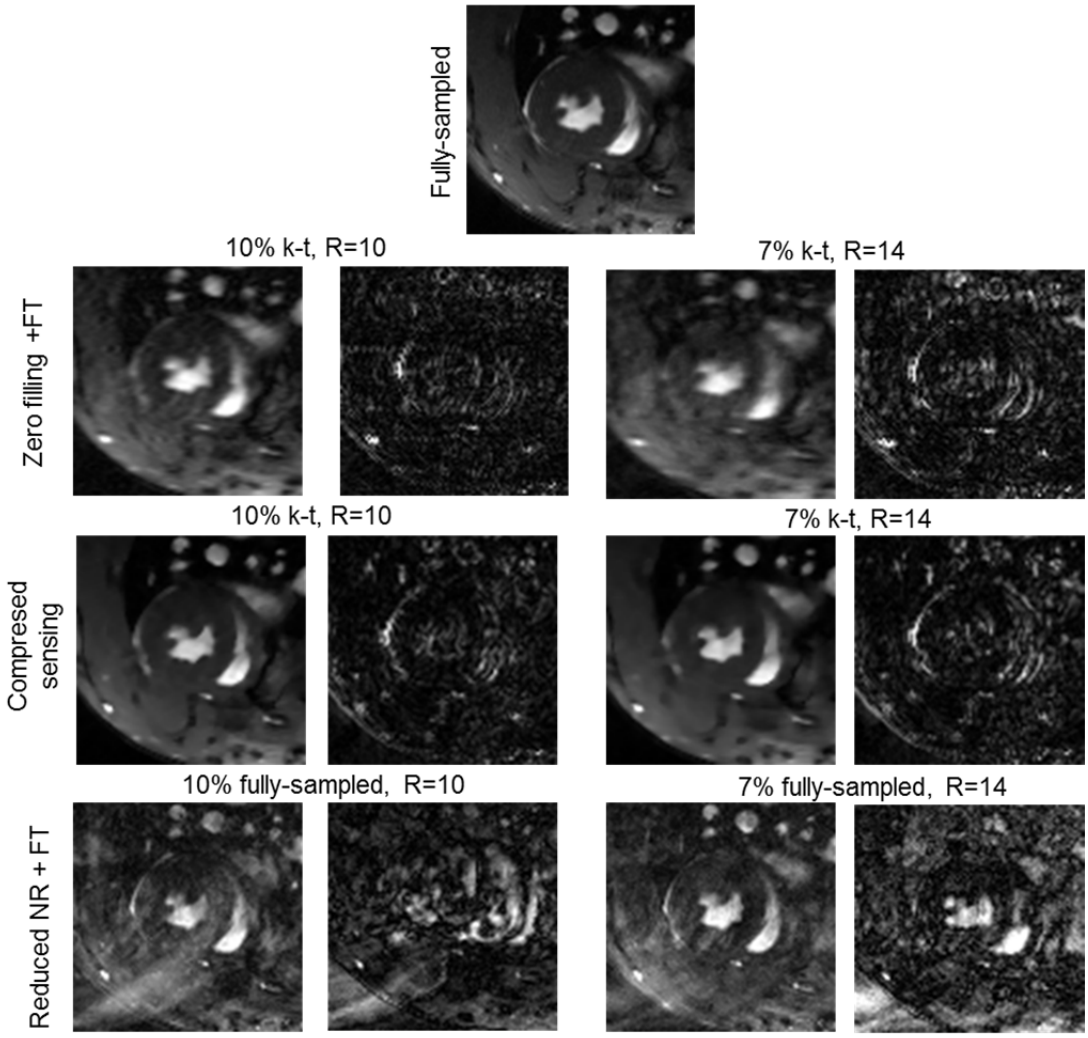

Figure 4.9. Reconstructed and difference images (with an amplification factor of 5) for different acquisition and reconstruction strategies with equivalent acquisition times. Randon undersampling is zero filled and reconstructed with a standard Fourier transform and also reconstructed with compressed sensing. Results are compared to a fully sampled with a reduced number of repetitions, reconstructed with standard Fourier transform.

To complete the image quality assessment, spatial blurring was evaluated drawing intensity profiles over the boundaries of the myocardium (Fig. 3.10). As we accelerate, sharp intensity changes in the images become smoother. However, for the highest accelerations shown, R=5 for a k_x-k_y patterns and R=14 for k-t patterns, intensity changes due to tissues changes are still distinguishable.

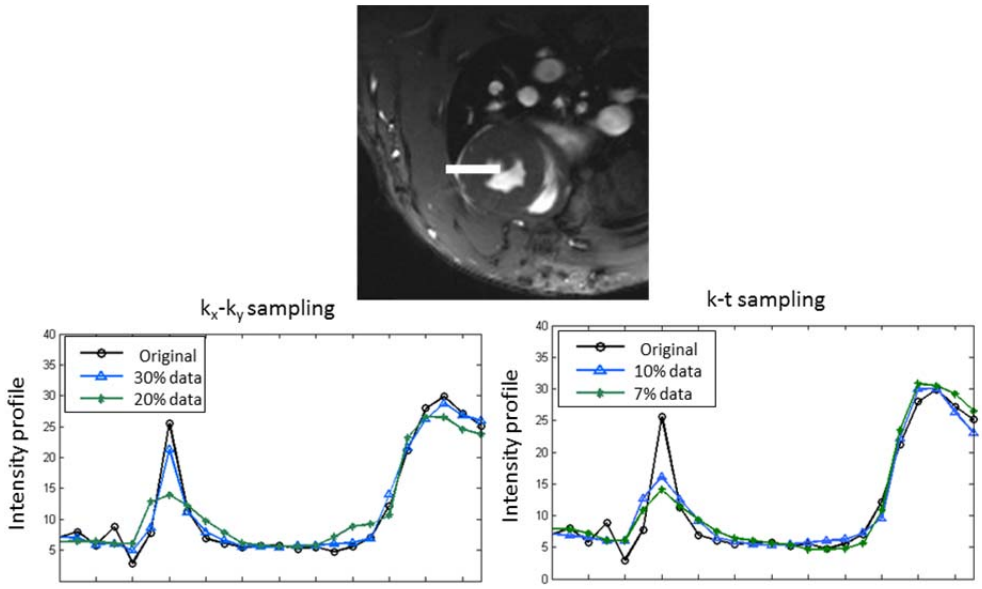

Figure 4.10. Intensity profiles. A) k_x-k_y undersampling patterns with 30% (R=3.3) and 20% (R=5) of the original data . B) k-t undersampling pattern with 10% (R=10) and 7% (R=14%) of the original data

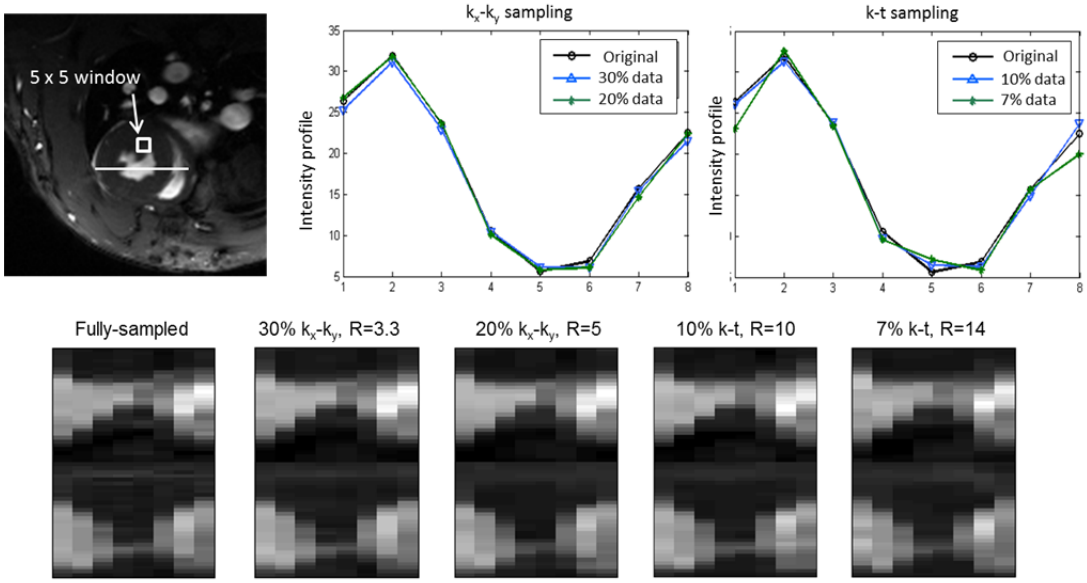

Figure 4.11. Assessment of temporal blurring. Top row: mean value in a 5x5 pixels ROI- Bottom row: y-t intensity profile containing both blood and myocardium

Both functional parameters measured for all the images reconstructed with higher acceleration factors were within the acceptable range for the four subjects analyzed. The Table 1 shows the actual values for the four animals studied, for both the fully-sampled and the reconstruction preserving only 7% of the data (R=14).

Animal	Control 1		Control 2		Control 3		Control 4	
Type of reconstruction	FS	CS	FS	CS	FS	CS	FS	CS
% V_diff	72.3	73.1	71.8	70.33	72.41	74.03	71.64	74.96
LVM (mg)	62.8	68.34	60.07	56.56	54.42	55.54	54.75	58.56

Table 4.1. Percentage difference between end-diastolic and end-systolic volumes (%V_diff) and within-slice left ventricle mass (LVM) for the four control small-animal datasets, for both the fully-sampled image (FS) and the compressed sensing (CS) images reconstructed with k-t patterns and 7% of the preserved data (R=14)

Figure 4.12 shows reconstructed and difference images preserving only 10% (R=10) and 7% (R=14) of the original data, for the two animals that underwent cardiac surgery. As in the case of healthy animals, delineation of the myocardium and general image quality are good for R=10. For R=14, images are blurred and more artifacts are present in the image, as can be appreciated in the difference image.

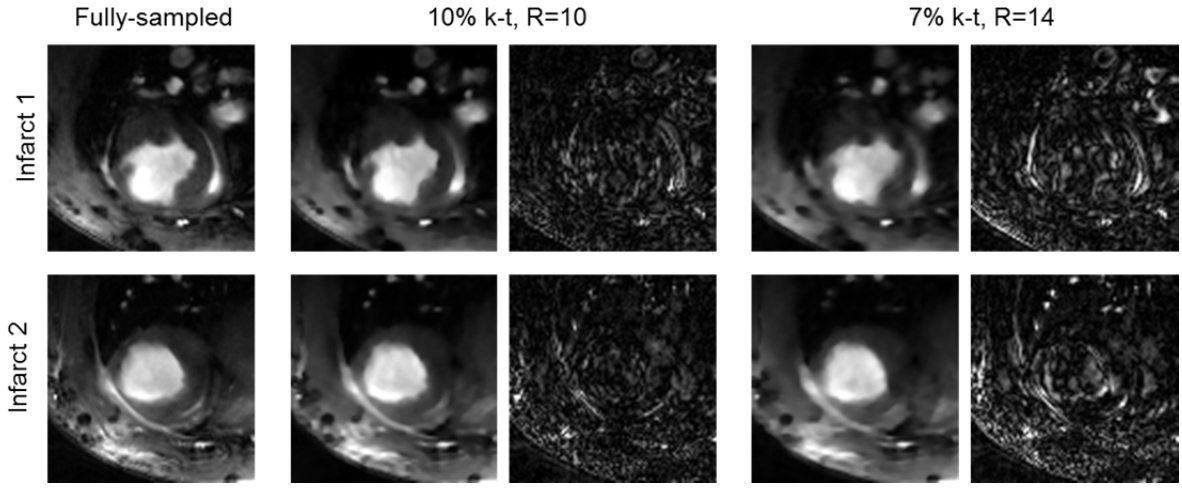

Figure 3.12. Reconstructed and difference images (with a zoom factor of 5) for the two infarcted animals at different acceleration rates.

As in the case of healthy animals, functional measurements were also evaluated for the higher acceleration rates (10 and 14). Due to the variability in image quality, three intraobserver measurements were obtained from the fully-sampled image for each of the animals. These measurements were used to set the threshold at ±2intraobserver standard deviations, that was established as an acceptable deviation range from the fully-sampled image. Table 3.2 shows the functional measurements for the two animals, for both the fully sampled dataset and the compressed sensing reconstruction for a 10% of the data (R=10). For the highest acceleration rate,

R=14, %V_diff for Infact1 and LVM for Infarct2 were out of the range considered as acceptable.

Animal	Infarct 1		Infarct 2	
Type of reconstruction	FS	CS	FS	CS
% V_diff	30.4	32.0	36.1	35.3
LVM (mg)	64.7	64.89	54.49	48.71

Table 4.2. Percentage difference between end-diastolic and end-systolic volumes (%V_diff) and within-slice left ventricle mass (LVM) for the two infarcted small-animal datasets for both the fully-sampled image (FS) and the compressed sensing (CS) images reconstructed with k-t patterns and 10% of the preserved data (R=10)

4.5 Discussion

In this chapter we proved that Split Bregman reconstruction based on the minimization of the TV across both space and time is a suitable and efficient method for applying the compressed sensing technique to self-gated cardiac cine MRI sequences in rats. Undersampling patterns with randomized sampling over time enabled us to achieve acceleration factors of up to 14 before significant image degradation occurred in healthy animals. In the case of animals that underwent cardiac surgery, the attainable acceleration was more moderate. These results suggest that accelerations around 10 are feasible for routine application of compressed sensing in cardiac cine studies.

4.5.1 Selection of undersampling pattern

Regarding the selection of k_x-k_y undersampling patterns, we found that using purely random patterns leads to a wide range of reconstruction errors (32% difference between the lowest and the highest error, Fig. 4.4), even though they comply with the low TPSF criterion. Thus, we complemented the TPSF criterion by testing the specific undersampling patterns over sample images. As shown in figure 4.5, the frame-independent behavior of undersampling patterns allows us to safely extrapolate from sample images to future cardiac studies.

For the k-t pattern, the most influential parameter is the undersampling percentage. The fact that final k-spaces are obtained from averaged data seems to alleviate the influence of a high decay exponent or the radius of the probability density function.

4.5.2 Maximum acceleration factor achievable

As expected, k_x-k_y undersampling patterns lead to lower acceleration factors (around 3) than a randomization performed over time (between 10 and 14). A key fact of our implementation is that the benefits of using randomization over time are boosted by the data-averaging step, as the percentage of nonzero data in the final k-space of each frame is higher than the percentage actually applied during acquisition.

Selection of the optimal undersampling percentage is very dependent on the tolerance to artifacts in the final image. The k-t pattern with a factor of 14 still led to good quality reconstructions, although the intensity profiles over the myocardium were sharper for lower acceleration factors (Fig. 4.10). As for temporal behavior, some blurring appears at accelerations higher than 3 for the k_x-k_y patterns and 7 for the k-t patterns. However, the presence of some artifacts due to high undersampling rates (R=10-14), does not necessarily alter the end diastolic and end systolic volumes neither the endocardium and epicardium areas measured in the images. According to the subjective assessment of an expert, factors of up to 5 produced no noticeable change in the images. Beyond this point, image quality decreased with the undersampling percentage, although it was still considered acceptable for factors up to 10 or 14. This statement is reinforced by the functional measurements on four animals, which were still in agreement with the values obtained from its respectively fully-sampled images.

Regarding the influence of the number or frames (or SNR) on the final achievable acceleration factor, figure 4.7 shows how as the SNR decreases, the reconstruction error increases. This can be also seen in figure 4.8, where the presence of artifacts is slightly more noticeable for 16 frames than when using 8 frames, although the quality for 16 frames is still acceptable. Accordingly, it seems that the final acceleration factor must be selected *ad hoc*, depending on the quality vs. acquisition time requirements for each application and user.

The benefits of compressed sensing compared to other simple strategies that would also reduce acquisition time, were illustrated in figure 4.9. If we just undersample the data with a random pattern and then zero fill the missing data and perform a standard reconstruction, incoherent artifacts appear in the reconstructions and they clearly impair the delineation of the myocardium. On the other hand, if we decrease the number of repetitions of a fully-sampled acquisition to reduce acquisition time, the SNR level is severely reduced and considerable motion artifacts appear in the images. The proposed compressed sensing methodology

successfully eliminates all these incoherent artefacts produced by the undersampling, and, at the same time, circumvents the presence of motion artifacts and SNR reduction, allowing the proper quantification of the images at high acceleration rates.

Regarding the infarcted animal studies, for the highest acceleration rate, R=14, the quality of the images was slightly worse compared to the case of the healthy animals. The images look smoother, which can be appreciated both in the reconstructions and in the difference image, where the error is not limited to the edges of the myocardium, as it was in the case with healthy subjects. These results suggest that accelerations over 10 are not advisable when working with pathological subjects. This idea is confirmed by the functional measurements, which were out of the acceptable range for the highest acceleration. These differences between healthy and pathological animals might be due to the different initial image quality. When animals had undergone a cardiac surgery, the motion of the myocardium is restricted, therefore the motion pattern of the heart is different and the classification of phase encoding lines into different frames might be more difficult, even in the case of fully sampled acquisition.

The literature contains several findings on compressed sensing algorithms applied to cardiac cine sequences. Some have been applied in simulations and others to real data of human cine images, although few have been tested with small animal studies. A wide range of acceleration factors has been reported: in human cardiac studies they range from 3 [7] to 16 [3]; most are around 6 or 9 [67]. For small animals, reported acceleration factors are about 3 [4, 10] or 9 when combined with GRAPPA [8]; our acceleration factor of 15 is clearly an improvement on these results. We expect to obtain even higher acceleration factors in future versions of our algorithm by combining compressed sensing with parallel imaging strategies or coil spatial information.

Interestingly, a simple straight comparison of acceleration factors between methods is not completely fair owing to differences in field strength, in the spatiotemporal resolution of the original images, and differences in the quality pursued in the final images. Another source of disparity is the potential difference between using prospective or retrospective cine sequences. Depending on the reconstruction used, retrospective cine sequences provide images with a higher SNR than prospective ECG cardiac cine sequences in the same acquisition time (or with the same SNR for a lower acquisition time) [30].

The only previous study that made use of retrospective cine in small-animal studies reported an acceleration factor of 3 [10], which is much lower than that achieved with our approach. We used the same basic MRI sequence and the same sparse transform, although important

differences were recorded between both approaches. Motaal et al. used undersampling patterns randomized over time, but they did not apply variable density functions to generate them. In addition, the approach of Motaal et al. applies to the very specific case of high-frame-rate cine sequences, whereas our work is concerned with the more common case of low-frame-rate cines with higher quality images. The acquisition parameters in both works, and therefore the quality of the original fully sampled images, are very different. In our case, the higher quality of the original images enabled higher acceleration factors, thus explaining in part the large difference in the acceleration factors achieved.

4.5.3 Efficiency of the reconstruction algorithm

In our algorithm we used temporal and spatial TV as regularization functionals. However, other regularization terms can be easily used in the Split Bregman formulation [94]. For spatial regularization, spatial TV [3] and wavelet transform or a combination of both [51] are the most widely used. It is known that spatial TV removes noise and incoherent artifacts and provides stability to the reconstruction algorithm [94]. For this reason it has been suggested to combine TV with other sparsity transforms, such as wavelet or curvelet transforms [119] or dictionary learning [120]. With regard to temporal regularization, temporal TV [10], nuclear norm [5, 74, 121], non-local TV [122] or B-splines to estimate motion [71] have also been proposed.

In general, spatial and temporal TV lead to sparse representation and provides good acceleration factors, as presented in this paper. However, other spatial and temporal transforms that lead to sparser representations may provide even higher acceleration factors, although sparsity is not the only requirement to get better results.

In dynamic applications, the compressed sensing problem requires computationally expensive calculations when using classic constrained and even unconstrained optimization methods. However, Split Bregman solves the constrained problem exactly and efficiently by using a splitting framework that leads to a quadratic equation (solved in the Fourier domain) and to shrinkage operations. The advantages of our reconstruction algorithm include the fact that derivative operators are analytical functions in the Fourier domain and thus allow us to avoid selecting and using a regularization parameter inherent to unconstrained problems. One of the contributions of our work is to extend and validate the benefits of the spatiotemporal Split Bregman formulation.

Our results showed that a number of approximately 500 iterations is enough to achieve a reasonable quality in reconstructed images, for $\lambda = 1$ and $\mu = 4$. With our entire dataset (32 images, 8 frames, 4 coil elements) the reconstruction was completed in 90 seconds on a Dell

Precision T5500 with Intel Xeon, using 8 CPUs (2.4 GHz and 12 GB RAM). Our computing time per frame was competitive with the fastest method found in the literature [1] and is lower than most [4], thus confirming the computational advantages of using the Split Bregman method for spatiotemporal applications. The number of iterations, and so the reconstruction time, depends on the values of λ and μ. In our work the values chosen were obtained after an empirical assessment. As in other studies [94, 99] the accuracy of the solution was not very sensitive to the actual value of these parameters, yet the value of μ affects the reconstruction time. It is possible that the optimum value might be different for other type of studies (for instance, different anatomical localization or spatiotemporal resolution).

4.5.4 Limitations and future work

It is important to note that the results of this work were based on simulations performed using real data, in which the undersampling patterns were applied *a posteriori* over the fully sampled acquired data. To conclusively assess the acceleration factor advisable for routine preclinical studies, a more detailed study with a higher sample of subjects must be carried out. This study should cover whole heart cine acquisitions on both healthy and unhealthy animals with different physiological characteristics (such as different motility or different cardiac frequency). Whole ventricle ejection fraction (EF) and left-ventricle mass measurements (LVM) should be performed and analyzed on this wide range of acquisitions. Also, the study must be performed over datasets acquired directly in a compressed sensing regimen, with directly undersampled acquisitions.

4.6 Conclusions

We successfully applied the compressed sensing technique to self-gated cardiac cine acquisition in small animals. For that purpose, we developed a modification of the Split Bregman reconstruction algorithm based on the minimization of TV in both spatial and temporal dimensions. The introduction of a time-varying random sampling clearly improved the efficiency of the undersampling schemes. For the specific case of IntraGateFLASH cardiac cine acquisition, the compressed sensing methodology described enabled us to obtain accelerations factors of 10-14 with almost unnoticeable image degradation in healthy animals. The evaluation of animals with myocardial infarction indicated that an acceleration factor of 10 is more adequate than 14 for routine applications that involve animals under different pathophysiological conditions.

5 Compressed sensing for cardiac MRI cine sequences: a real implementation on a small-animal scanner

5.1 Introduction

In Chapter 4 it was shown how compressed sensing techniques can be applied to accelerate cardiac magnetic resonance studies in small animals. Self-gated cardiac cine sequences were proved to be highly accelerated by exploiting the intrinsic temporal sparsity of cine images minimizing the total variation across both the spatial and temporal dimensions (ST-TV). The compressed sensing methodology detailed in Chapter 4 pointed that accelerations up to 10-14 were feasible for IntraGateFLASH sequences. However, these statements, as in most of compressed sensing works, were based on simulations in which undersampling patterns were retrospectively applied on previously acquired fully-sampled data.

Despite the great amount of compressed sensing works published in the past years, very few in the literature report compressed sensing accelerations based on actually undersampled acquired data [84, 123, 124] and they do not focus on the comparison between simulation results and real compressed sensing acquisitions. Besides, none of them is focused on cardiac small-animal datasets.

The aim of this chapter is to verify the feasibility of the previously reported compressed sensing acceleration factors in routine acquisitions, by implementing a direct compressed sensing acquisition for self-gated cardiac cines in a 7 T Bruker BioSpec 70/20 scanner.

5.2 Material and methods

5.2.1 Implementation of the compressed sensing acquisition

The acquisition in compressed sensing regimen was implemented in a 7 T Bruker BioSpec 70/20 scanner provided with software ParaVision 5.0. In Bruker scanners, sequences are defined by means of programmable components called methods; each method consists of a set of files that provide and assign adequate values to the different acquisition and reconstruction parameters.

Among those files, it is especially important the pulse program file (.ppg), which describes the execution of the pulse sequence by means of appropriate pulse program commands. Pulse program statements are meant to control the pulse sequence timing, RF pulse generation, data acquisition, data flow and hardware units, as the magnetic field gradients. These programs follow C-programming language standard and can be changed and re-complied to generate a new or a modified sequence.

Figure 5.1 shows an example of a visual representation of the tasks that the pulse program is in charge of.

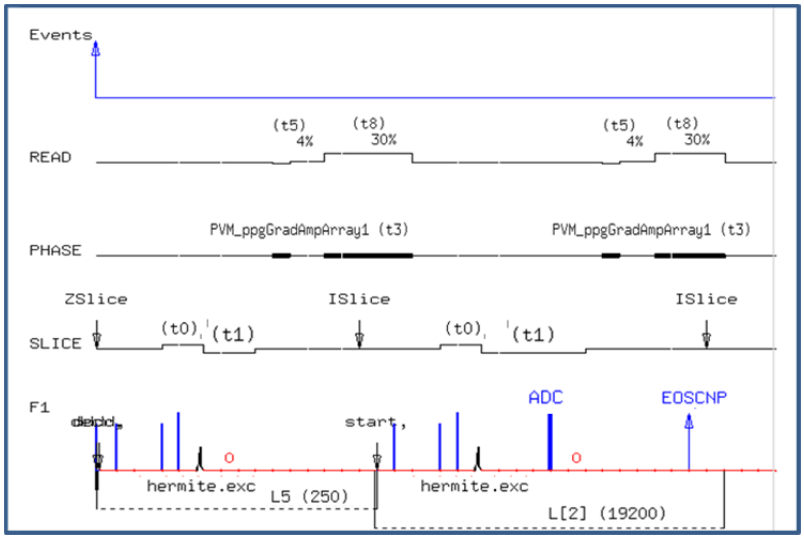

Fig. 5.1 Pulse program display of an IntraGateFLASH sequence. The pulse program commands will determine the duration and amplitude of the gradients and the different RF pluses applied

The compressed sensing acquisition was implemented as a modification of a standard IntraGateFLASH pulse program. In pulse programs, each phase encoding line to be acquired has a corresponding amplitude that needs to be applied in the different magnetic field gradients. Those amplitudes are stored in memory as lists that are iteratively evaluated during the data acquisition. For the compressed sensing implementation, undersampling patterns were codified as a new variable, a binary list in which 0's are meant for skipped phased encoding lines and 1's are meant for phase encoding lines to be acquired. During acquisition both undersampling and gradient amplitude lists are evaluated, thus, when a certain phase encoding line has to be skipped, the corresponding gradient amplitude is also skipped. Such the actual gradient amplitudes applied are no longer linear but correspond to the quasi-random undersampling pattern specifically selected.

Before evaluating the compressed sensing acquisition *in vivo*, and in order to verify the correct sequence implementation, we acquired images from a $CuSO_4$ phantom. In first place, the phantom was acquired fully-sampled and later it was acquired in compressed sensing regimen

with different undersampling patterns. Real compressed sensing acquisitions were compared to the application of the same undersampling patterns retrospectively over the fully-sampled dataset.

5.2.2 Undersampling patterns

As in Chapter 4, the undersampling patterns were created based on a variable probability density function that gives higher probability of being preserved to lines according to its distance to the k-space center (see Figure 5.3). The benefits of including randomization across time in the undersampling patterns have been well shown in the previous chapter, so the undersampling patterns applied vary in both time and phase encoding direction.

Same k-t undersampled patterns as in Chapter 4 were also used in this chapter for the cardiac cine acquisitions. However, in the case of the real acquisition, due to implementation restrictions, the number of different temporal undersampling patterns actually used in acquisition was limited to 20 k_x-k_y patterns, that were repeated over time, as it can be seen in Figure 5.2. The repetition rate of these patterns did not correlate with the same frequency of frame assignation in such a way that, after data sorting and averaging, each frame had a different undersampling pattern, so temporal randomization was still preserved.

5.2.3 Acquired datasets

Initial compressed sensing acquisitions were performed on a cylindrical water phantom, within which there were four syringes full of water doped with different $CuSO_4$ concentrations such they give different signal intensities. A fully-sampled FLASH sequence was acquired with a volume coil and the following acquisition parameters: TE = 6 ms, TR = 100 ms, number of frames = 1, matrix size = 128x128, FOV = 4x4 cm, NA = 1, and slice thickness = 1 mm, acquisition time = 12 s. Using the same acquisition parameters, several compressed sensing acquisitions were performed, maintaining different percentages of the original data, from 50% (R=2) to 20% (R=5).

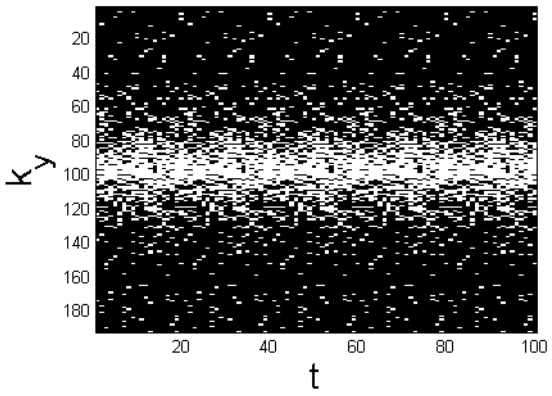

Fig. 5.2 Undersampling pattern generated from a variable probability density function (20% data, R=5). Black lines represent eliminated or non-acquired phased-encoding lines from the original complete data

Regarding the *in vivo* small-animal acquisitions, the cardiac cine IntraGateFLASH sequence used the same acquisition parameters as in Chapter 4: TE = 2.43 ms, TR = 8 ms, number of frames = 8, matrix size = 192x192, FOV = 4.8x4.8 cm, and slice thickness = 1.2 mm. In the case of the fully sampled image, the number of phase encoding repetitions was 200, acquired in a total time of 5 min 7 s. Images were acquired using a linear coil resonator for transmission and a dedicated four-element cardiac phased array coil for reception. After a fully-sampled acquisition, compressed sensing data at different rates of undersampling were acquired. Previously stored undersampling patterns were used such the levels of undersampling rated from 30% (R=3.3) to 5% (R=20) of the complete data.

Two different healthy rats (n=2) were acquired and evaluated in this chapter.

5.2.4 Reconstruction algorithm

Same reconstruction algorithm based on Split Bregman formulation as in section 4.2 was applied: the spatiotemporal gradient as sparsifying transform that, according to the compressed sensing formulation, leads to the minimization of spatiotemporal TV subject to a data constraint:

$$\min_u \left\|(\nabla_x u, \nabla_y u)\right\|_2 + \left\|\nabla_t u\right\|_1 \quad \text{such that } \left\|RFu - f\right\|_2^2 < \sigma^2 \qquad [5.1]$$

5.2.5 Quality measurements

In Chapter 4 both undersampling patterns and reconstructions were retrospectively tested over a fully sampled dataset, thus the gold standard image was available to perform error measurements. However, in this chapter no fully-sampled gold standard image is available for the assessment of cardiac cine reconstructions. Despite a fully-sampled image was acquired to be used as reference, the high variability in the respiration and heart beat rate in rats make that consecutive acquisitions, even though they have the same acquisition parameters, can show a high (relatively) variability between them. This fact prevents us from using a previous fully-sampled image as gold standard, thus we used it just as a reference. Quality in the images acquired directly in compressed sensing regimen was evaluated visually, paying special attention to the texture, the heart motility and the presence of artifacts in the reconstructed images.

It also has to be mentioned that, again opposite to Chapter 4, the lack of a gold standard fully-sampled image forces us to find a different stopping criterion for the iterative reconstruction algorithm. Thus, for this chapter, we reconstructed the images for different fixed numbers of iterations, and the best reconstructed image was assessed based on visual inspection.

In order to compare the effects of real compressed sensing acquisitions against simulated compressed sensing, the same undersampling patterns used in acquisition were also retrospectively applied to the fully-sampled image of each of the subjects. As mentioned before, in the scanner implementation we used only 20 different k_x-k_y patterns, while accelerations claimed in Chapter 4 were assessed using 200 different k_x-k_y patterns. The use of only 20 different k_x-k_y undersampling patterns instead of only 200 might lead to a lower temporal randomization of compressed sensing data. To discard this as a possible cause influencing on the achievable the acceleration factors, acquired data was compared against simulated data with both 200 and 20 different k_x-k_y patterns. All results were compared for similar cardiac phases.

5.3 Results

The compressed sensing acquisition was successfully implemented. Experiments confirmed the feasibility of the technique, and the forecasted reduction in acquisition times corresponding to each acceleration factor was positively verified.

In figure 5.3 a compressed sensing reconstruction with real undersampled acquisition and its equivalent compressed sensing reconstruction with retrospective simulated undersampling are

compared for the static phantom acquisition. Both compressed sensing real acquisition and compressed sensing simulated data were filled with zeros and reconstructed with standard Fourier reconstruction, the difference image between the two reconstructions is shown in figure 5.3. Also, difference image between the compressed sensing reconstruction of the really acquired undersampled data and the original fully-sampled image is shown in figure 5.3-E.

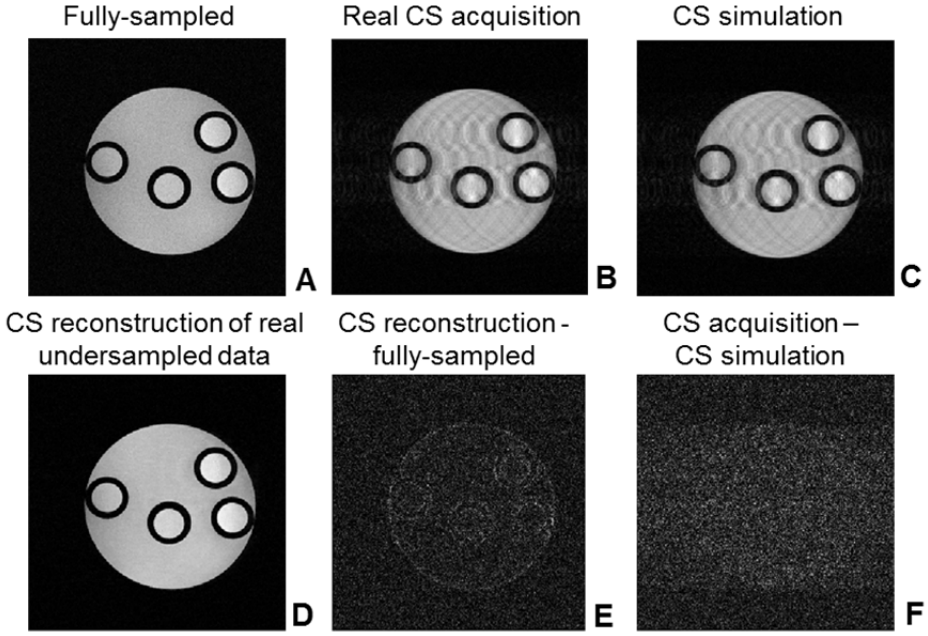

Figure 5.3. A) Fully-sampled acquisition. B) Compressed sensing (CS) acquisition of a 45% of original data, plus zero filling and Fourier transform reconstruction. C) Retrospectively undersampled image, plus zero filling and Fourier transform reconstruction, same undersampling as in B was applied. D) Compressed sensing reconstruction of image B. E) Difference image between fully-sampled, A, and the compressed sensing acquisition plus compressed sensing reconstruction D. F) Difference image between B and C.

Figure 5.4 shows cardiac cine images acquired with real compressed sensing undersampling for percentages of undersampled data from 20% (R = 5) to 7% (R =14). It must be pointed out that for real data acquisitions the correspondence between frames of different images cannot be perfect because they belong to different acquisitions, and thus the matching among frames is only approximate. Motion artifacts are present for the higher acceleration rates (R=10 and R=14). For the highest acceleration rate, R=14, the image quality is inadequate as the presence of motion artifacts hampers a proper myocardium delineation.

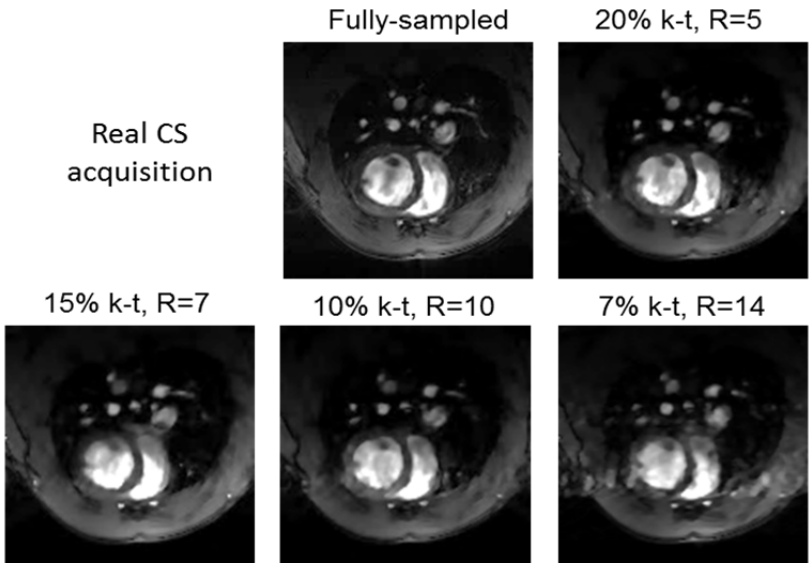

Fig. 5.4 Reconstructed images for different undersampling patterns and acceleration factors experimentally acquired.

Figures 5.5 and 5.6 show the fully sampled images that was retrospectively undersampled with 200 and 20 different k_x-k_y patterns, respectively. Images were reconstructed for the same percentages as in figure 5.4.

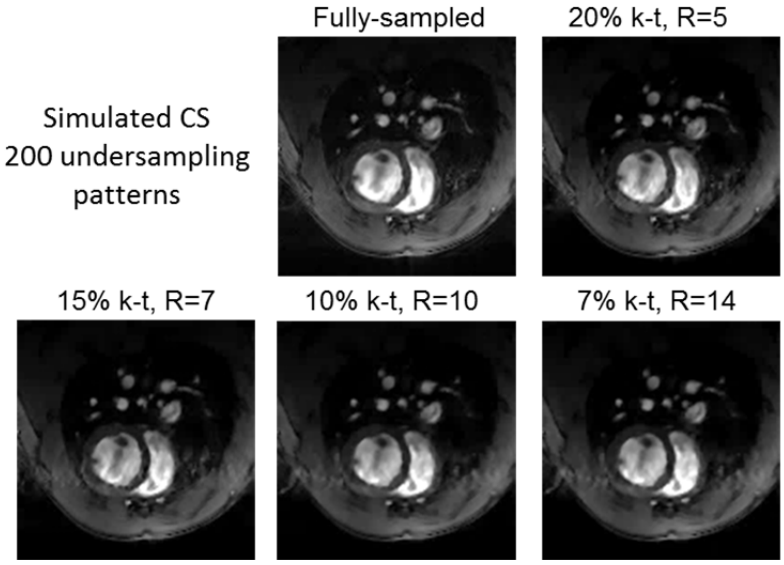

Fig. 5.5 Reconstructed images for different undersampling patterns and acceleration factors in retrospectively simulated study. 200 different kx-ky patterns were used in the undersampling

In both cases image quality decreases as the acceleration rate increases and some artifacts appear for the higher acceleration factors, however the delineation of the myocardium is still possible at the highest acceleration rates.

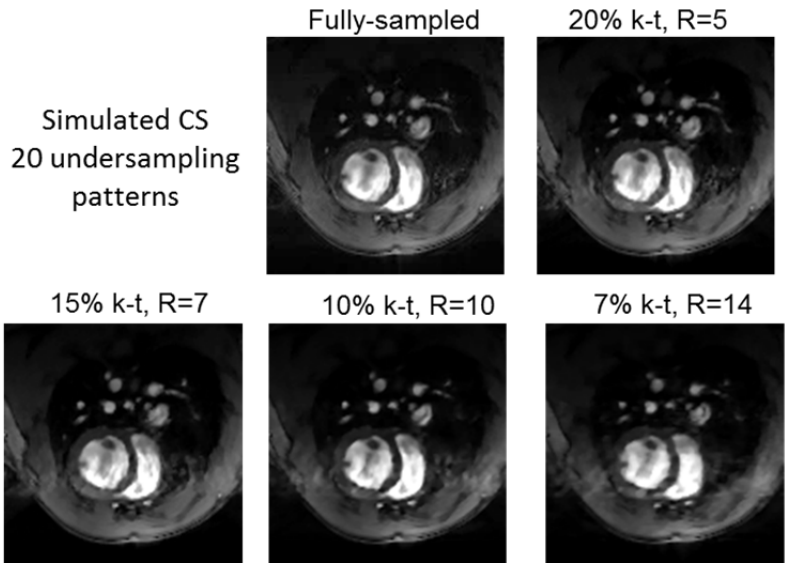

Fig. 5.6 Reconstructed images for different undersampling patterns and acceleration factors in retrospectively simulated study. 20 different k_x-k_y patterns were used in the undersampling

5.4 Discussion

The feasibility of implementing a compressed sensing acquisition for cardiac cine MRI sequences was successfully proven in this work; this is the first step to successfully incorporate compressed sensing acquisitions in routine applications for cardiac MRI in small animals.

Phantom experiments proved the correct compressed sensing implementation. We found no significant differences between a real compressed sensing acquisition and a simulated compressed sensing approach with retrospective undersampling (Fig. 5.3). Both compressed sensing strategies were zero filled and reconstructed with a Fourier transform, the image difference between both compressed sensing strategies is in the level of noise (Fig. 5.3-F). This is the expected result when scanning a static object, confirming the straight equivalence between prospectively and retrospectively undersampled compressed sensing reconstructions.

Regarding cardiac cine acquisitions, in Chapter 4 acceleration factors up to 10 or 14 were claimed as feasible for retrospectively simulated undersampled data. In the case of actually acquired undersampled data (figure 5.4) acceleration factors around 7-10 seem achievable; accelerations of 14 resulted in images with conspicuous artifacts that make them incompatible with daily practical routine.

Comparing simulated and real compressed sensing, for equivalent acceleration rates, quality in the retrospectively simulated undersampled images was, in general, slightly better than in the case of real compressed sensing acquisition. In the case of the simulated compressed sensing, some artifacts are present for the highest acceleration rates (R=10, R=14), however, they do not alter greatly the delineation of the myocardium, which has direct influence on the diagnostic value of the images [118]. However, in the case of real compressed sensing acquisitions and the artifacts and smoothness present for the higher acceleration rates, alters the limits of the myocardium and thus would alter the functional measurements. In general, the degradation in image quality as the percentage of undersampling increases is more noticeable in the case of real compressed sensing acquisition than in the case of using simulated retrospective undersampling.

A reduced temporal randomness in the acquired data could be a factor influencing in the lower acceleration factors achieved in practice. However, as figures 5.5 and 5.6 show the difference between using 20 or 200 is almost is almost negligible, being only noticeable at the highest acceleration rate, R=14. Hence, this lower temporal randomization is discarded as the main cause of lower acceleration factors in practice.

The difference in image quality between retrospectively and prospectively undersampled compressed sensing reconstructions for the cardiac cine acquisitions might be explained by differences in their sensitivity to motion. It is important to note that simulated and real undersampling might be influenced by motion in different ways, especially when lower percentages of data are preserved. Let's assume that a certain motion event occurs and that its influence cannot be completely eliminated by the navigator processing (such there is some residual motion in our acquisition). In the case of real compressed sensing acquisition, consecutive acquired phase encoding lines would be affected in a similar way by that residual motion event. Those consecutive phases would potentially belong to the same final k-space frame; what would make that particular frame to be highly influenced by that particular motion event, which could be translated as artifacts in the reconstructed images.

However, if we retrospectively apply a simulated undersampling to our data, 'virtually' consecutive phase encoding lines were not really consecutive in the acquisition, so they will not be affected the same way by any particular motion event. And moreover, as the navigator classification is done retrospectively, those 'virtually' consecutive phase encoding lines would potentially correspond to different cardiac frames in the reconstruction. So there might be no

correlation (or it would be very low) in the way 'virtually' consecutive acquisition lines are affected by the same motion event.

This chapter demonstrates the feasibility of using compressed sensing acquisitions in practical routine in small-animal scanners. However there are some limitations that still remain to be overcome.

From the implementational point of view, we have to overcome the limitation in the number of different patterns that can be stored; other ways of data storage must be explored. Also, we should consider the options of making the undersampling patterns user-selectable and the compressed sensing reconstruction on line.

In terms of validation, before including compressed sensing acquisitions in preclinical routines, we should carry out a more detailed study. This study should include the evaluation of different undersampling patterns in a larger number of subjects, both healthy and unhealthy subjects under different physiological conditions. Compressed sensing acquisitions must also include whole-heart acquisitions and functional measurements have to be evaluated before claiming that a certain acceleration factor is feasible for *in vivo* routine in small-animal studies. As a reference, we can cite the work of Vicenti et al. [82] where a complete study for the validation of single breathold cardiac compressed sensing cine in humans was carried out. This work can serve as a guideline to plan a complete and large-sample small-animal detailed study.

5.5 Conclusions

This chapter proves that compressed sensing acquisitions are feasible for cardiac cine acquisitions in routine small-animal scanners. Acceleration factors around 10 seem achievable in practice, close to those obtained in previous simulations. However, there are some small differences between the compressed sensing acquired data and the retrospectively undersampled ones. These differences motivate a large-sample and a more complete study in order to find the most suitable acceleration factor attainable for routine applications *in vivo*.

6 Motion, Resolution and Noise Thresholds for the Accurate Classification of Human Coronary Atherosclerotic Plaque by MRI

6.1 Introduction

The majority of acute coronary syndromes are triggered by the rupture of non-occlusive atherosclerotic plaques. The accurate assessment of plaque composition, and consequently the risk of plaque rupture, is thus of critical importance [39]. At present, CT remains the most widely used approach to image the coronary wall [125, 126]. Despite the spatial resolution of CT is excellent, its soft tissue contrast is poor. Recent experience in the characterization of carotid plaque by magnetic resonance (MR) has been very encouraging [15-19]. However, this success has not been replicated in the heart, where MR imaging of the coronary wall has been limited to isolated studies of wall thickening, delayed enhancement and intraplaque hemorrhage [12-14].

The presence of calcification in coronary atherosclerotic plaque is an important feature and has provided further impetus to image the coronary arteries with CT. However, in a recent *ex vivo* study, multicontrast MR including ultrashort TE (UTE) imaging for calcium was shown to robustly classify human coronary atherosclerotic plaques [20]. The study was performed on *ex vivo* donor hearts with extensive coronary artery disease. Figure 6.1 shows a representative *ex vivo* imaging of a calcified lipid-rich atherosclerotic plaque. T1-weighted MR image shows signal hypointensity in the calcified portion of the plaque (fig. 6.1A), what strongly agrees with the histological section of the plaque stained with Movat's pentachrome (fig. 6.1C). In the case of CT image, performed with the same spatial resolution as the T1-W image (250 μm isotropic), the calcification is overestimated due to blooming artifacts.

Nevertheless, the ability to image plaques in coronary artery walls *in vivo* will be markedly determined by SNR, resolution achievable and motion artifacts and yet it remains unknown what these thresholds are. The aim of this chapter is to determine the SNR, resolution and motion limits required for the accurate assessment of human coronary plaque *in vivo*. With that purpose, raw k-space data of the previously mentioned *ex vivo* study were saved to provide a high SNR and high spatial resolution (250 μm) ground truth dataset.

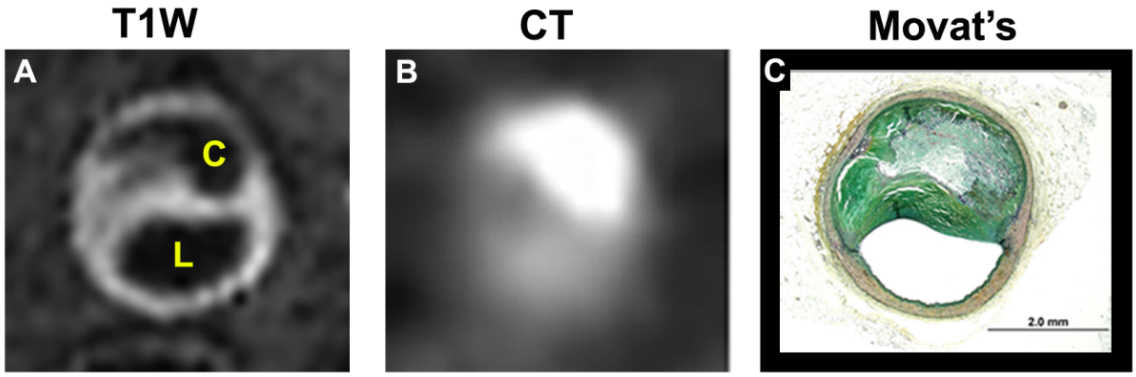

Figure 6.1: Cross section of a calcified atherosclerotic plaque of a human coronary artery. (A) T1-weighted image with 250-µm isotropic spatial resolution. (B) High definition CT with comparable 250-µm spatial resolution. (C) Histological stain with Movat's pentachrome

The raw data of seven complex coronary plaques were reconstructed under varying levels of SNR and spatial resolution. In addition, motion profiles of the coronary artery were obtained in 11 healthy adults and patients with suspected cardiac disease, and were used to characterize the impact of coronary motion. We hypothesized that the principal challenge limiting MRI of human coronary plaque *in vivo* would be posed by motion, rather than by resolution. To the best of our knowledge, this study was the first to systematically assess the requirements for the accurate characterization of coronary plaque *in vivo* using real coronary motion data and actual MR images of complex human coronary atherosclerotic plaques.

6.2 Material and Methods

6.2.1 Dataset

Seven atherosclerotic plaques from donor hearts with extensive coronary artery disease were analyzed. The specimens were immersed in a fluorcarbon matching medium (Fomblin, Ausimont, NJ) in order to eliminate the signal from the vessel lumen, and imaged on a 9.4 T horizontal bore MRI scanner (Biospec, Bruker) using a transmit-receive birdcage coil. We chose to perform our analysis on the k-space data of the T1 weighted images because of the sharp morphological features produced by plaque calcification in these images, see figure 6.1. The acquisition parameters of the T1 weighted 3D FLASH data were as follows: FOV = 64x48x24 mm^3, matrix size = 256x192x96, isotropic resolution of 250 µm, α = 45º, TR/TE = 30/2.5 ms with fat suppression and 1 average [20]. The fully sampled k-space data were considered as "ground truth" and were reconstructed under varying conditions of resolution, SNR and motion.

All reconstructions were implemented in MATLAB (MathWorks, MA, USA) and compared to the ground truth original image (250 μm true resolution, zero motion).

6.2.2 Modification of Spatial Resolution and SNR

The true resolution of the reconstructed images was modified cutting the k-spaces along all three axes, such as they gave isotropic resolutions of 0.35, 0.5 and 0.7 mm. To facilitate direct comparison with the original image, those k-spaces were zero-padded to give a final interpolated resolution of 0.25 mm. We used a Hamming window in the transition to avoid Gibbs artifacts Based on preliminary evaluations, and since a resolution of 0.5 mm is by far more attainable *in vivo* than 0.25 mm, all the consequent experiments, regarding both SNR and motion evaluations, were performed over the data with a true isotropic resolution of 0.5 mm interpolated to a 0.25 mm final resolution.

The impact of noise was assessed by adding varying levels of Gaussian noise to the real and imaginary parts of the base image [127, 128]. SNR in a complex image can be defined as the ratio of the average signal (S) to the standard deviation of background noise (σ)

$$SNR = \frac{S}{\sigma} \qquad [6.1]$$

In the real and imaginary parts of an MR image, noise can be assumed to follow a Gaussian distribution with variance σ^2. Though, if SNR is measured in a magnitude image the distribution of background noise is no longer Gaussian: In low SNR (background) regions of a magnitude image, noise is governed by a Rayleigh distribution with variance

$$\sigma_M^2 = \left(2 - \pi/2\right)\sigma^2 \qquad [6.2]$$

Where σ_M^2 is the noise variance measured in the magnitude image. In high SNR regions of the magnitude image, the mean pixel intensity measured M , can be approximated by

$$M = \sqrt{S^2 + \sigma^2} \qquad [6.3]$$

Thus,

$$S \approx \sqrt{\left|M^2 - \sigma^2\right|} \qquad [6.4]$$

$$\sigma = 1/0.655 \cdot \sigma_M \qquad [6.5]$$

SNR was measured in the magnitude image without any additional noise; M was measured in a ROI with high SNR, and σ_M in a ROI in the image background that was free of artifacts. Following the equations in **¡Error! No se encuentra el origen de la referencia.** and [6.5], the true mean image intensity S and the true noise variance σ^2 were calculated. As mentioned, additional levels of Gaussian noise, with standard deviation σ_A, were added to the real and imaginary parts of the original image, such that the new true noise deviation was given by $\sigma' = \sqrt{\sigma^2 + \sigma_A^2}$. SNR values with added noise were calculated using σ' according to equations [6.4] and [6.5].

6.2.4 Corruption of K-space Data by Motion

The impact of coronary motion was assessed in two ways: Firstly, through the use of simulated motion profiles and secondly, through the use of actual coronary motion profiles obtained in the healthy volunteers and patients (n=11). Translational motion was introduced into the images by applying the Fourier shift theorem.

To mimic a real *in vivo* study, several assumptions were made regarding the acquisition scheme. We assumed an acquisition window of 100 ms per heartbeat. According to the state-of-the-art acquisition parameters for *in vivo* studies [129], this duration would correspond to 15 k-space lines acquired per heartbeat. We modeled the acquisition order as central encoding for the first phase encoding direction and linear for the second one.

6.2.4.1 Simulated motion

Experiment A

Four patterns of coronary motion were modeled: 1) Motion with both fixed frequency and amplitude, 2) motion with random frequency but fixed amplitude, 3) motion with fixed frequency but random amplitude and, 4) motion with both random frequency and amplitude. Fixed coronary motion was modeled as occurring every 1, 3, 5 or 10 beats and having an amplitude of 0.75, 1.5, 2.25 or 3mm in all directions. Random coronary motion was modeled with displacements ranging between ±1.5 or 0-3mm, in all directions, and a period of 0-10 heart beats. For those cases in which random amplitude motion was used, three different realizations were averaged to give the final error measurements.

Experiment B

In a clinical scenario, motion will be present every heartbeat, but its great impact on image quality can be reduced using appropriate acquisition strategies. With that purpose, we simulated a new data acquisition scheme. This new scheme consists in dividing k-space into two different regions with different acquisition properties [7]. The central portion of k-space, inner k-space, is assumed to be sampled during a simulated 25s breathold (during which motion was assumed to be zero), and only the outer portion of k-space was sampled during free-breathing and thus motion is expected. The percent of Breathold Inner K-space Sampling (BIKS), which refers to the percent of phase encoding lines in both directions sampled during the simulated breathold, was set at 0, 10, 20 or 30%.

A theoretical motion correction algorithm was applied to the free-breathing data (*ex-vivo* data plus motion). This correction was assumed to be imperfect thus resulting in some degree of residual motion, where a perfect correction of coronary motion would result in 0% residual motion. The percentage of residual motion after motion correction was modeled from 2-50%, as a multiplicative reduction factor applied in each of the three spatial directions.

We introduced random motion every heartbeat to the outer portion of the k-spaces, the portion corresponding to the free-breathing part of the acquisition. To evaluate the influence of the inner k-space size and the percent of residual motion varying values of BIKS and residual motion were evaluated

6.2.4.2 In vivo motion

Real motion profiles were acquired by placing three orthogonal pencil-beam navigators on the heart directly adjacent to the proximal right coronary artery (RCA) in 11 adult subjects, both patients and volunteers. This motion profiles were incorporated to the *ex vivo* datasets. The spatial direction with the largest displacements was always assigned to the head-foot acquisition direction. The direction with the second largest displacements was assigned in a 50% of the cases to the right-left direction, and in the remaining 50% of the cases it was assigned to antero-posterior direction.

A common strategy used to alleviate the effect of motion consists in placing an acceptance navigator window positioned around the end of the expiration of the head-foot direction [130]. We simulated this acceptance window placed in the head-foot direction, which reflects the impact of respiratory motion on the RCA, with sizes 3 or 5 mm.

Navigator data showed that translational motion was by far the largest in the head-foot direction; even though, it measured at least 1-2 voxels in all directions. This fact posed the question whether correcting motion only in the head-foot direction might be enough for proper plaque visualization. As with the simulated motion data, the central portion of k-space was assumed to be sampled in a breathold, and the outer portion of k-space was sampled during free breathing. Images were reconstructed with varying percentages of BIKS (0, 10, 20 or 30%) and residual motion (from 2 to 50%), also the impact of motion correction in only the head-foot direction was compared with motion correction in all three directions.

6.2.5 Statistical analysis

Statistical analysis was performed using the R environment for statistical computing (R Foundation for Statistical Computing, Vienna, Austria). Analysis of variance followed by a Tukey post-test was used to evaluate differences between 3 or more groups with Gaussian distributions. An unpaired t-test was used for comparisons involving two groups. All distributions, other than the sharpness data, were Gaussian. The equation used to calculate image sharpness, however, produced a non-Gaussian distribution of values. Wall sharpness was thus evaluated with a Kruskal-Wallis test followed by a Wilcoxon test with Bonferroni p-correction. Gaussian data are reported as mean ± standard deviation. Non-Gaussian data are reported as median with the interquartile range in parenthesis.

6.2.6 Quality measurements

Those portions of the vessel with significant plaque were manually segmented and the following measurements were calculated:

RMSE

Root Mean Squared Error (RMSE) between the original and reconstructed images was calculated according to the formula:

$$RMSE = \sqrt{\frac{\sum_{x=1}^{M}\sum_{y=1}^{N}\left|I_{recon}(x,y) - I_{orig}(x,y)\right|^2}{MN}} \qquad [6.5]$$

Sharpness

Wall sharpness was calculated as previously described [131], over both the vessel wall and the outer part of the plaques. One representative slice of each plaque was chosen to perform the measurements. Images were magnified four times using bilinear interpolation; and radial intensity profiles (3 voxels width) starting at the vessel centroid were drawn every 40º (see Figure 6.8-A). The 20% and 80% points between the maximal and background signal intensities were calculated for each side of the radial intensity profiles. The inverse of the averaged distance (in millimeters) between the two points of each side was used as sharpness measurement.

Calcification area

Segmentation of the plaque into calcified and non-calcified regions was performed using a k-means clustering approach. Calcification area was calculated in the same slice as the sharpness. According to its intensity, the algorithm classifies the plaque in two groups; the one with lower intensity corresponds to plaque calcification. Calcification area was computed and errors in the size of the calcification area detected were used as a quantitative measurement.
The iterative k-means algorithm used works as follows:

1. Compute the intensity distribution of the images
2. Initialize the centroids of the two clusters with k random intensities
3. Assign each pixel in the image to the cluster that minimizes the L1 distance between the
pixel and the cluster centroids
4. Compute the new centroid for each of the clusters
5. Steps 3 and 4 are repeated until there is no change in the new clusters computed

6.3 Results

6.3.1 Spatial resolution and SNR limits

Figure 6.2-A shows the impact of true resolution on plaque characterization. Plaque morphology could be well characterized with a true resolution of 500 μm, interpolated to 250 μm. This 500 μm true resolution maintained all important features present in the original resolution of 250 μm, and produced an average RMS error of only 0.11 ± 0.02. A true resolution of 700 μm produced inadequate image quality. All further analyses, including the impact of simulated and real coronary motion, were thus performed with a true resolution of 500 μm.

The impact of SNR over images with 0.5 mm true spatial resolution, in absence of motion, is illustrated in figure 6.2-C. While SNR values <10 resulted in poor image quality, no significant difference in RMS error was seen between an SNR of 11 and 30.

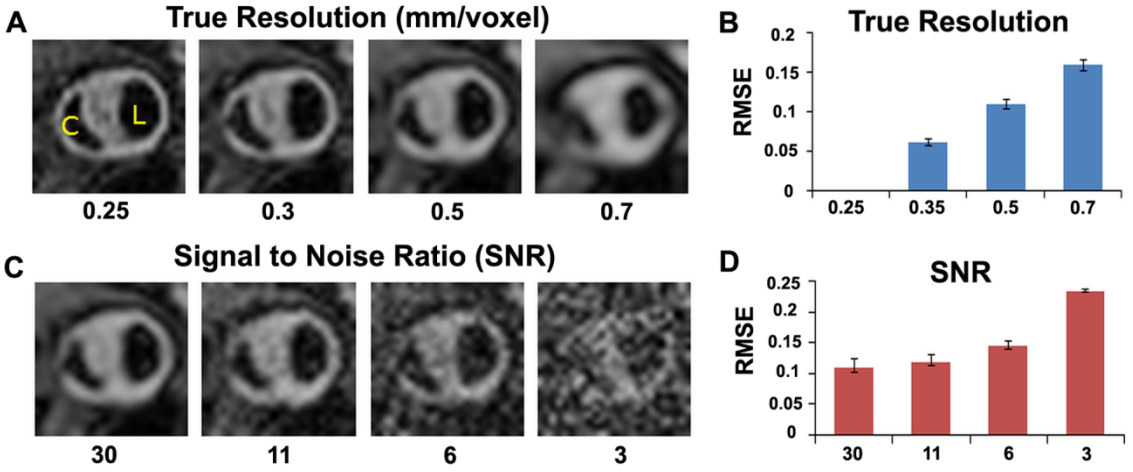

Figure 6.2: Impact of spatial resolution and signal to noise ratio (SNR) on plaque characterization. C denotes calcification in the plaque and L indicates the lumen of the vessel. (A) All images were interpolated from varying true resolution values to a final resolution of 0.25 mm. (B) Average RMSE for different true resolutions. (C) Images with 0.5 mm resolution and increasing levels of noise. (D) Average RMSE values for different SNR levels.

6.3.2 Impact of motion

6.3.2.1 Simulated motion

Experiment A

Figure 6.3 illustrates the effects of synthetic motion; in figure 6.3-A-D a schematic description of the motion events simulated is offered. The frequency of motion had a far bigger effect on image quality than the amplitude of motion. RMSE increased from 0.14 ± 0.01 with 3mm of motion every 10^{th} heartbeat to 0.46 ± 0.07 when motion was introduced every heartbeat. For a given frequency of motion, RMSE was lower when the simulated displacement was random (non-fixed) versus fixed. Also, for the same absolute displacement, motion with random positive and negative displacements produces lower error than motion with equivalent fixed positive displacement

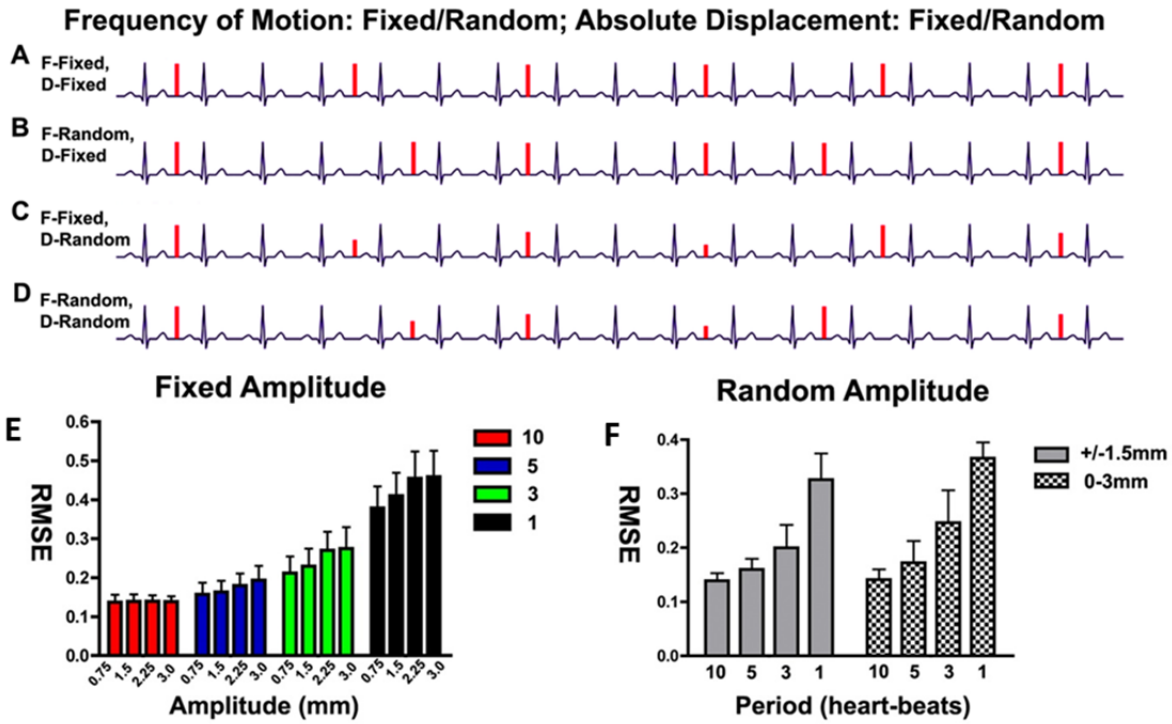

Figure 6.3: Simulation of the effects of coronary motion on the ability to resolve plaque morphology. 4 types of motion were simulated: (A) motion with fixed frequency and displacement, (B) motion with random frequency and fixed displacement, (C) motion with fixed frequency and random displacement and (D) motion with random frequency and random displacement. (E-F) Effect of frequency and amplitude on RMSE values.

Experiment B

The impact of imperfect motion correction, as well as the improvement obtained by acquiring the inner k-space in breathold regimen, is illustrated in figure 6.4. Figure 6.4-A offers a matrix of images for varying degrees of residual motion and inner k-space size. Both images and RMSE bars (fig. 6.4-B) confirmed that, for a certain level of residual motion, as the percentage of BIKS increased, image quality improved. And, as expected, at a given level of residual motion, image quality improved as the percentage of BIKS increased. The motion simulation revealed an inflection point in RMSE above 25% residual motion (fig. 6.4-B). This is also shown in figure 6.4-C, where RMSE has been plotted for varying degrees of residual motion and either 10 or 30% BIKS. The results of the simulation thus suggested that motion correction with an efficiency of >75% in all three directions is needed for accurate plaque characterization *in vivo*.

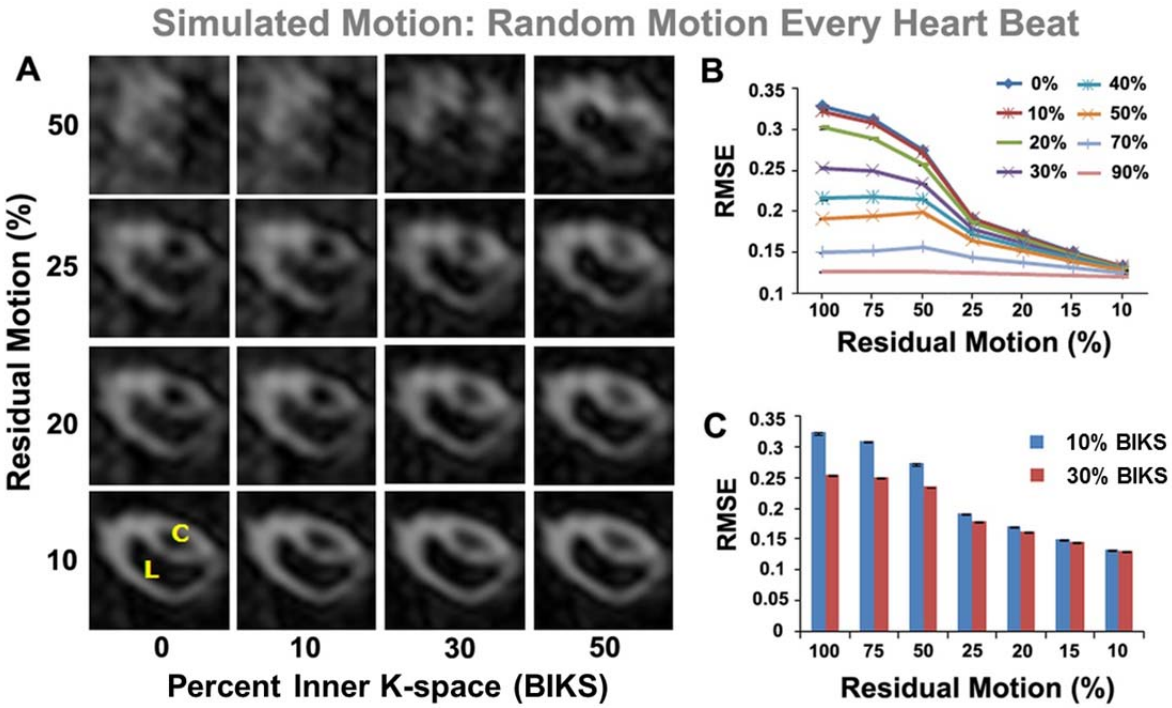

Figure 6.4: Simulation of motion correction with inner k-space sampled in a breathold; synthetic motion with random amplitude was introduced every heartbeat. (A) Matrix of images for varying percentages of residual motion and inner k-space sampled in a breathold. (B-C) RMSE values for different BIKS and RM percetages.

6.3.2.2 In Vivo motion

Typical in vivo motion profiles are shown in Figure 6.5. Three distinct types of coronary motion could be identified. Type 1 motion was seen in 5/11 cases and was characterized by predominant motion in one direction, the head-foot direction. Type 2 motion was also seen in 5/11 cases and was characterized by substantial periodic motion in more than one direction. Type 3 motion was seen in 1 patient and involved abrupt (non-periodic) motion in all directions, consistent with patient movement during the acquisition.

The motion profiles are shown before (fig. 6A-C) and after (fig. 6D-F) filtering with a 5mm navigation window. The mean absolute displacement in the head-foot direction (the axis of navigator acceptance window) was 0.77 ± 0.63 mm for a 3 mm acceptance window and 1.17 ± 0.93 mm for a 5 mm acceptance window. Mean displacements were 0.79 ± 1.07 and 0.85 ± 1.26 mm along the orthogonal axes. Thus, even with navigator-filtered Type 1 profiles, displacement in all 3 directions was substantially larger than 500 μm, the minimum true resolution needed for plaque characterization.

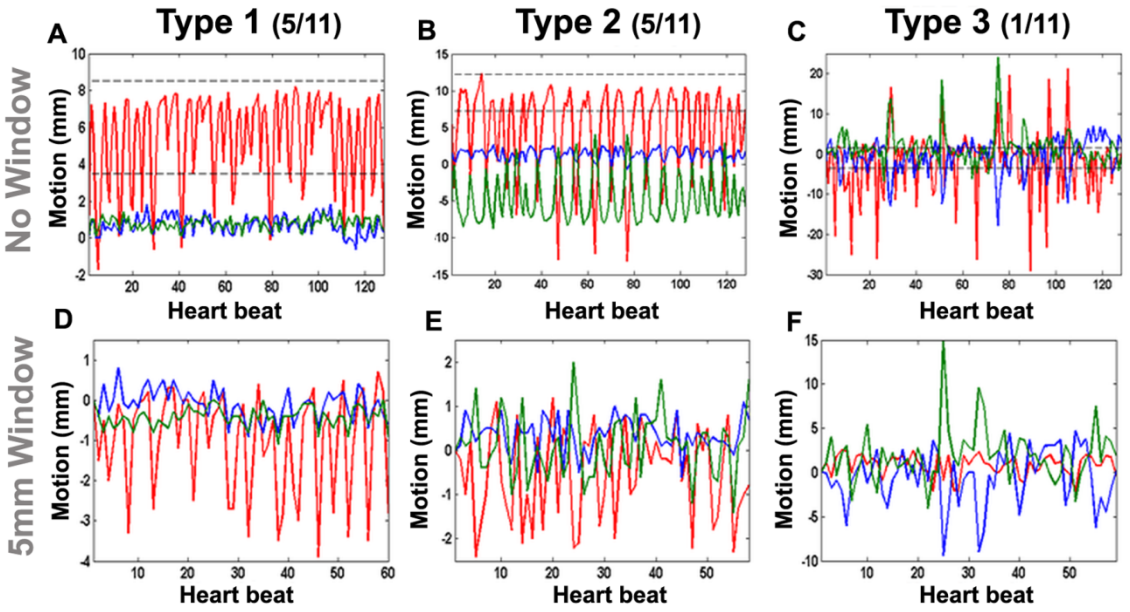

Figure 6.5: Motion profiles acquired on the right coronary artery of 11 volunteers and patients; 3 different types of motion were identified. (A) Type 1, predominant motion in only one direction, head-foot direction. (B) Type 2, large degree of motion in two spatial directions. (C) Type 3, substantial and broad motion in all 3 spatial directions. (D-F) Motion profiles are shown after being filtered with a 5 mm navigator window placed in the head-foot direction

The importance of performing motion correction in all three spatial directions is demonstrated in figure 6.6. Motion correction in only one direction (the head-foot direction), even when almost perfect (with only 2% of residual motion), did not allow plaque morphology to be resolved. Likewise, motion correction in all three directions but with 50% residual motion was associated with poor image quality. Motion correction with < 25% residual motion in all 3 directions was needed for adequate plaque visualization. The impact of true coronary motion was thus well predicted by the simulation, and showed that the tolerable level of residual motion in each direction cannot exceed 25%.

The benefits of reducing the acceptance window from 5 to 3 mm, as well as the degree of motion tolerance, depended on the type of motion profile applied, as figure 6.7 shows. For type 1 motion, image quality with a 3 mm or 5 mm window was similar and, in both cases, 25% residual motion was tolerable. With type 2 motion profiles, 25% residual motion was acceptable for a 3 mm window, while 15% was tolerable for a 5 mm window. With type-3 motion, less than 10% residual motion was required in all cases. The average RMSE with 25% residual motion , taking all 11 motion profiles into account, was 0.21 ± 0.04 with the 5 mm window, and 0.19 ± 0.04 with the 3 mm window. An abrupt increase in RMSE was seen with residual motion values >25%, in strong agreement with the predictions of the simulation.

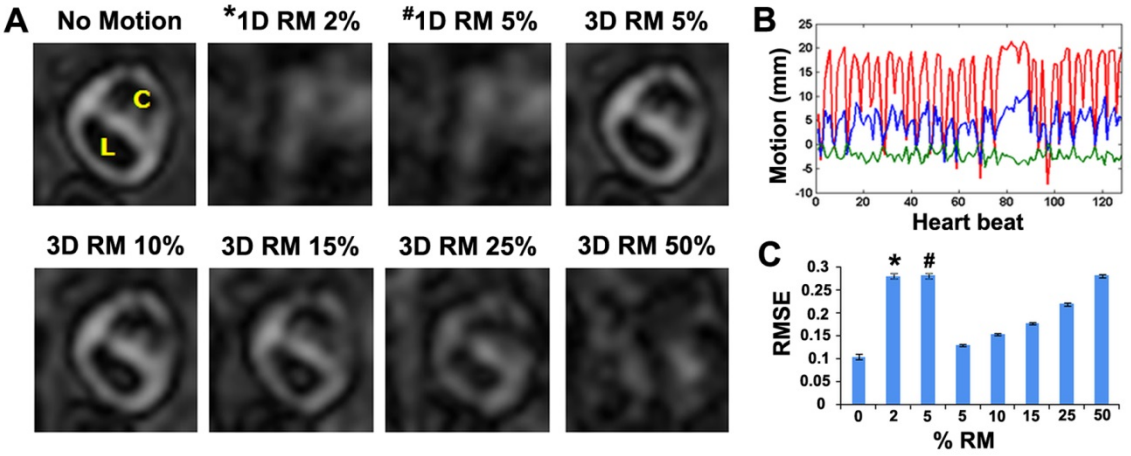

Figure 6.6: Impact of motion profiles and degree of motion correction on plaque morphology. RM residual motion Images shown in (A) were derived from the motion profile shown in (B). (C) Impact of all 11 motion profiles on 7 plaques (n=77)

The benefits of reducing the acceptance window from 5 to 3 mm, as well as the degree of motion tolerance, depended on the type of motion profile applied, as figure 6.7 shows. For type 1 motion, image quality with a 3 mm or 5 mm window was similar and, in both cases, 25% residual motion was tolerable. With type 2 motion profiles, 25% residual motion was acceptable for a 3 mm window, while 15% was tolerable for a 5 mm window. With type-3 motion, less than 10% residual motion was required in all cases. The average RMSE with 25% residual motion , taking all 11 motion profiles into account, was 0.21 ± 0.04 with the 5 mm window, and 0.19 ± 0.04 with the 3 mm window. An abrupt increase in RMSE was seen with residual motion values >25%, in strong agreement with the predictions of the simulation.

The effect of vessel motion on image sharpness and the detection of plaque calcification is depicted in figure 6.8. Overall wall sharpness in the vessel wall was 3.5 (3.18-3.76) mm^{-1} without the introduction of any motion, 2.7 (2.28-3.06) mm^{-1} with motion correction in 3 directions (30% BIKS, 15% residual motion) and 1.24 (0-2.28) mm^{-1} with motion correction in 1 direction (30% BIKS, 2% residual motion). Sharpness values specifically within the plaque were 3.5 (2.65-3.95) mm^{-1} without motion, and 2.59 (2.0-3.06) mm^{-1} and 0 (0-2.28) mm^{-1} with motion correction in three and one directions, respectively. The difference in sharpness between motion correction in one and three directions reached significance ($p< 0.05$) for both the entire vessel wall and within the plaque. Motion correction limited to one direction introduced significant error into the detection of plaque calcification (fig. 5.8-G). The average error in the area of calcification increased from 1.13 ± 0.98 mm^2 with motion correction in 3 directions to 1.81 ± 1.40 mm^2 with correction in only one direction. It is worth to mention the case of plaque sharpness with 0 as median. We observed that when we performed motion correction in only

one direction, the definition of the plaque was completely lost for certain motion profiles due to the severe degradation suffered by images, and thus the delineation of its sharpness, scored with 0 in those circumstances.

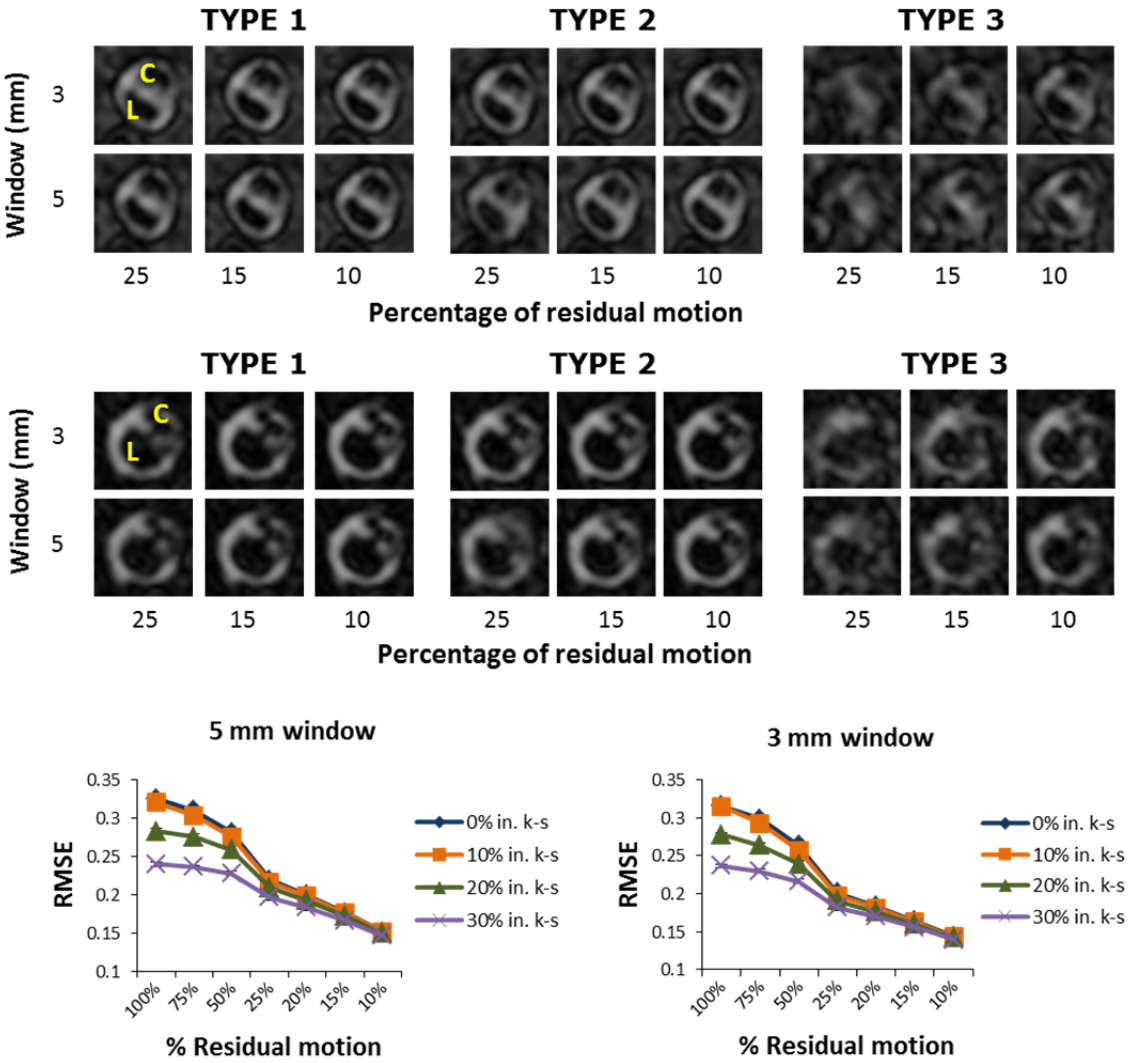

Figure 6.7: Impact of motion profile type and navigator window size on plaque characterization. (A-B) Examples of 2 plaques processed with three different motion profiles for different values of navigator window and percent of residual motion; all images were simulated with 30% of inner k-space sampled in breathold and motion corrected in all three directions. (C-D) Impact of navigator window, inner k-space size and percentage of residual motion for all motion and plaques (n=77).

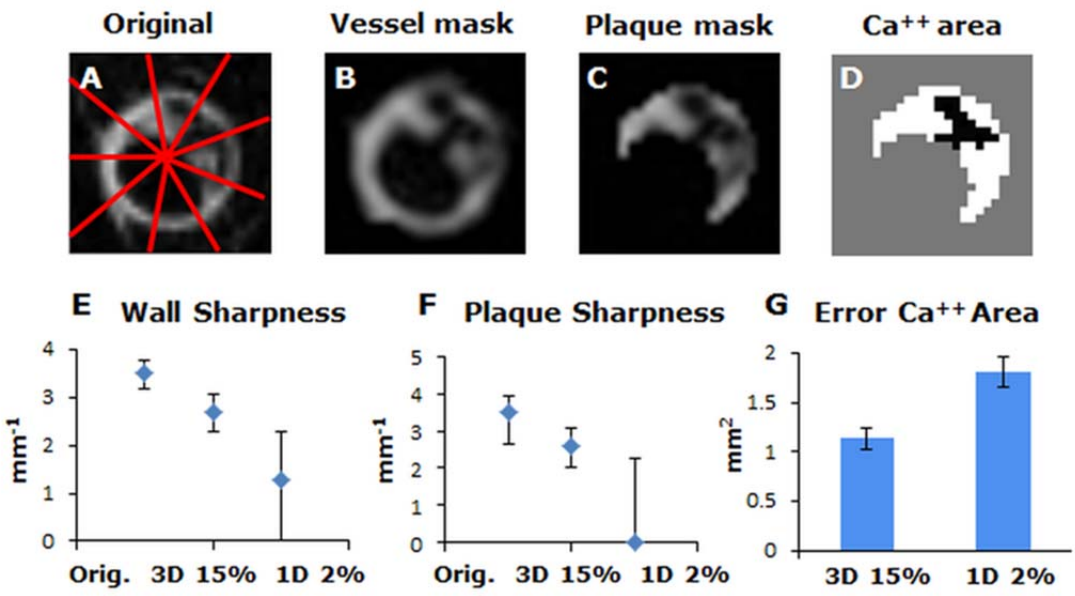

Figure 6.8: Impact of motion correction on image sharpness and quantification of calcification area. (A) Original image with a resolution of 250-µm, radial lines used to calculate sharpness are superimposed on the image. (B) Vessel mask at 500-µm resolution used to compute the radial profiles. (C) Plaque mask at 500-µm resolution used to calculate the calcification area. (D) Result of plaque segmentation, black region corresponds to calcification area. (E-F) Vessel wall and plaque sharpness. G) Error in the measurement of calcification area.

6.4 Discussion

Atherosclerotic plaque in human coronary arteries has a highly complex composition, which can be robustly characterized with *ex vivo* MRI [20]. MR of the coronary wall *in vivo*, however, has yet to reach its full potential. While diffuse thickening [13], hemorrhage [12], and the delayed washout of gadolinium [14] have been detected *in vivo*, detailed characterization of coronary plaque has not been feasible. In this chapter, we elucidate the factors underlying the current limitations of coronary wall MRI: Resolution, SNR and motion limits for the accurate classification of atherosclerotic plaque by MRI are defined. This assessment is based on simulation experiments performed by modifying a high resolution *ex vivo* coronary artery data. *In vivo* motion profiles obtained by placing navigators directly on volunteers and patients' hearts were used to determine the impact of real motion on the characterization of plaque features.

Our data suggest that, while improvements in spatial resolution are helpful, a true resolution of 500 µm is adequate for the characterization of human coronary plaque. However, at this resolution, motion correction in all three Cartesian directions is vital, and it is the principal

impediment to MR-based characterization of coronary atherosclerotic plaque *in vivo*. Cross sectional MRI of the coronary arteries *in vivo* has been performed with a true resolution of 350x350x1000 μm^3 [129], which produces a voxel size almost identical to an isotropic resolution of 500 μm. Thus the true resolution needed for accurate plaque characterization, 500 μm, is within reach. Furthermore, ongoing improvements in receive arrays, inner volume excitation, parallel acquisition and high field systems have the potential to improve image quality even further.

Experiments based on adding synthetic motion to the ground truth data show that, in absence of any motion correction, the frequency of motion is the key feature of motion, with effects more notorious than the ones produced by the values of motion amplitude evaluated. These simulation experiments also demonstrate that motion correction is indeed necessary when motion is present every heartbeat (which corresponds with the real-motion case). As expected, it was proved that with the acquisition scheme proposed, the larger the inner k-space is been sampled in breathold regimen, the better the image quality obtained.

Regarding *in vivo* motion profiles, it was seen that the motion of the coronary arteries is complex and can differ markedly from patient to patient, also displacement values observed were quite high in terms of our pixel size. The results also showed that the degree of motion correction can be imperfect and substantial amounts of residual motion are well tolerated. As an example, a residual motion of 20% in the three directions (with 5 mm window and 30% inner k-space size) would imply that we can tolerate average motion values of 0.22, 0.17 and 0.15 mm in the different spatial directions, respectively.

The amounts of residual motion tolerated differed slightly depending on the type of motion and the size of the gating window used. At this regard, it has to be taken into account that the use of navigators requires a compromise to be made between scan efficiency and accuracy. With the motion profiles used here, scan time would be approximately 1.5 times longer, on average, with a 3mm window compared to a 5mm window. While this reduction in efficiency was associated with improved image quality with Type 2 motion, it produced little benefit with Type 1 motion. The width of the navigator acceptance window should thus ideally be tailored to a specific patient's coronary motion profile.

With regard to more specific quality parameters analyzed in this chapter, a good level of sharpness and calcification delimitation is maintained for 15% of residual motion when

correcting motion in three directions. On the contrary, when motion correction is performed in only one direction, even though the motion correction is almost perfect, the sharpness and calcification area are severely degraded.

The use of real motion profiles measured directly on the heart to evaluate the impact of motion is indeed one of the main contributions of this work. There are some previous works studying the motion of coronary arteries [132-135] and also few works focused on visualization *ex vivo* plaque imaging [136, 137] but, to the best of our knowledge, this is the first work evaluating the impact of motion, measured directly on coronary arteries, on the accuracy of *in vivo* characterization of coronary atherosclerotic plaques.

The high precision needed in motion correction, and thus in motion estimation, required for plaque feature classification discards the use of traditional techniques, such as the use of diaphragm motion corrected by a multiplicative factor to estimate motion in the heart [138, 139]. A proper estimation of the motion measured directly in the heart and in the three orthogonal directions has to be implemented. Latest advances in navigator acquisition strategies and motion correction algorithms may help to the consecution of those requirements [70, 134, 140-142], although it is likely that methods specifically developed or tuned for the plaque visualization must be implemented.

The analysis in this study involved T1 weighted images of atherosclerotic plaque. The relevance of the findings in UTE and T2 weighted images will need to be further studied. In particular, the impact of noise on the T2 weighted images, which have a far lower signal, could be less forgiving. On the other hand, the radial nature of the UTE acquisition could render it less vulnerable to the effects of motion. It should be noted that none of the plaques evaluated in this study showed signs of hemorrhage, and gadolinium could not be given to delineate the fibrous cap. In addition, the effects of rotational motion were not examined.

In the clinical setting, cross sectional MRI of the coronary wall will need to be targeted to the most concerning segments in an individual patient. Screening approaches using computed tomography or MRI of the entire coronary tree will thus need to be developed. Nowadays, CT may be better suited to this and can detect thick, eccentric and non-calcified plaque, all of which have been associated with a higher risk of rupture [39]. However, the ability of MRI to

characterize plaque morphology is unmatched, and may be improved even further with the advent of integrated MR-PET scanners. Considerable effort should thus be spent on addressing the challenges, defined in this study, that currently limit the accuracy of MRI in the coronary arteries.

6.5 Conclusions

This work offers valuable information to face future *in vivo* coronary atherosclerotic MRI plaque studies, proposing a new acquisition scheme and establishing the thresholds required for accurate plaque classification. Motion is, indeed, the highest difficulty to overcome for the consecution of *in vivo* coronary atherosclerotic plaque imaging. Improved motion estimation and motion correction strategies are required for the proper coronary plaque characterization.

7. Impact and limits of acceleration techniques for the visualization of human coronary atherosclerotic plaques *in vivo*

7.1 Introduction

As mentioned before, nowadays, CT remains the standard imaging technique when studying coronary atherosclerotic plaques. At the present time, the MRI state of the art is not developed enough to scan coronary atherosclerotic plaques, but there is no doubt about the potential benefits that coronary plaque visualization by MRI would provide [40]. For that to happen there are still many challenges to overcome, mainly imposed by coronary motion and the need of very high resolution images in a reasonable acquisition time. However, recent works proving the feasibility of MRI to classify and to analyze coronary plaques are encouraging.

Recent *ex vivo* studies have pointed that multi-contrast MRI can serve to accuratly characterize human coronary atherosclerotic plaques [20]. Also, the limits of SNR, motion and resolution required for the accurate classification of plaques have been determined in Chapter 6 [143]. These limits have been established based on simulations of *ex vivo* data merged with real *in vivo* motion coronary profiles. These results pointed out that an isotropic true resolution of at least 500 μm an SNR of at least 10 are required for the proper visualization of plaques. Also, it was found that, despite small values of residual motion are tolerated, motion correction in the 3 orthogonal spatial directions proved to be mandatory for coronary plaque imaging. Furthermore, a hybrid acquisition scheme, in which the inner part of the k-space is sampled during breathold, was proposed as an effective strategy to reduce the impact of motion in coronary images.

The 500 μm above-mentioned resolution can theoretically be achieved, but it would involve unacceptably long scan durations if reduced field-of-view (FOV) imaging is not used. Scanners with parallel transmission capabilities, supporting inner volume imaging, are now available and constitute an excellent tool for coronary atherosclerotic plaque MRI. On top of that, acceleration strategies, such as parallel imaging and the more recent compressed sensing have been successfully used to reduce acquisition time in coronary MRI [60, 83, 144]. In this work we hypothesize that the use of acceleration techniques might help not only to reduce acquisition

time of potential coronary plaque acquisitions, but also to make coronary atherosclerotic plaque imaging more robust against motion.

The aim of this chapter is to determine the impact and limits of acceleration techniques on the imaging of coronary plaque under conditions of physiological motion and reduced FOV ($64\times48\times24mm^3$). Reconstruction techniques such as GRAPPA [56], SENSE [57], a modification of SENSE including a TV penalty, and a multichannel compressed sensing reconstruction [80] have been analyzed under different conditions of SNR, motion and acceleration rates.

7.1 Methods

7.1.1 Dataset

As described in Chapter 6, seven atherosclerotic plaques from donor hearts with extensive coronary artery disease were analyzed (see figure 7.1-A). The specimens were imaged on a 9.4 T horizontal bore MRI scanner (Biospec, Bruker, Ettlingen, Germany) using a transmit-receive birdcage coil. 3D FLASH T1 weighted images with the following acquisition parameters were used: FOV = 64x48x24 mm^3, matrix size = 256x192x96, isotropic resolution of 250 μm, α = 45º, TR/TE = 30/2.5 ms with fat suppression and 1 average [20]. The fully sampled k-space data were saved and used to simulate the effects of motion, SNR and accelerated acquisitions through retrospective modifications of k-spaces.

Based on the conclusions of Chapter 6, 0.5 mm isotropic resolution was established as the target resolution; thus, raw data were reconstructed as having an isotropic true resolution of 0.5 mm. As in Chapter 6, high resolution k-spaces were cut around their centers to simulate an acquired resolution of 0.5 mm, and afterwards they were zero-padded to obtain an interpolated resolution of 0.25, to facilitate comparisons with the ground truth data. The impact of motion was modeled through the use of real *in vivo* motion profiles, acquired with 3 orthogonal navigators placed on the left ventricle of 10 healthy adults and patients. Motion was modeled as translational and incorporated into the data using the Fourier shift Theorem. Also, a hybrid acquisition scheme was simulated such that the inner part of the k-space was acquired in one breathold (equivalent to 30% of the non-zero phase encoding lines in each direction) and the outer part in free

breathing regimen, using a 5 mm gating window. Assuming that a perfect correction of coronary motion is not feasible, and based on previous results, a value of residual motion of 25% was assumed for motion profiles showing high displacements in one spatial direction, and 15% residual motion for motion profiles with high displacements in more than one spatial direction. Residual motion is expressed as a percentage, and is modeled as a multiplicative reduction factor applied to motion displacements in each of the three spatial directions. An example of those motion profiles can be seen in figure 7.1-B.

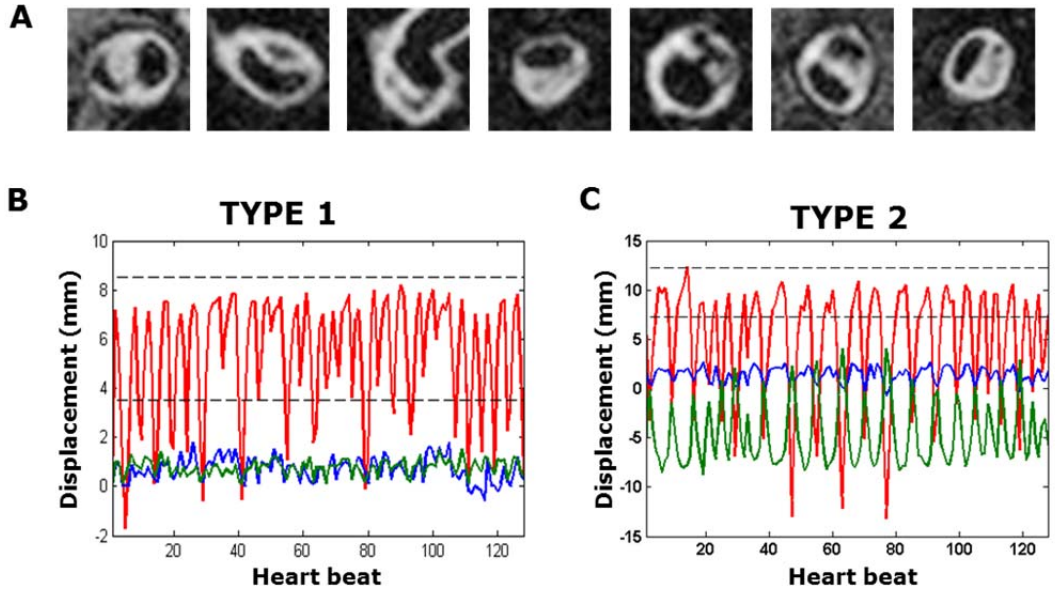

Figure 7.1. Original data. A) Seven *ex vivo* atherosclerotic plaques, 0.5 mm isotropic true resolution interpolated to 0.25 mm. B) *In vivo* motion profile with largest displacements in one spatial direction. C) *In vivo* motion profile showing large displacements in more than one spatial direction.

7.1.2 Simulation of a clinical scenario

To simulate a realistic clinical scenario, we simulated the use of a multi-channel receive coil array by using the coil sensitivity maps of a 34-element thoracic array. Those sensitivity maps were acquired on a commercial 3 T scanner (Skyra, Siemens Medical); experimental setup is shown in figure 7.2.

The mentioned sensitivity maps were incorporated to the 0.5 mm isotropic-resolution image to generate the data basis of this work. Varying levels of Gaussian noise were added to these data in order to simulate two different scenarios, a high SNR scenario (without any additional noise) and a more realistic low SNR scenario (SNR = 15).

Different acceleration factors were retrospectively simulated and images were reconstructed with different algorithms (see details in section 7.2.4). All simulations, processing and reconstructions were implemented and performed in MATLAB (MathWorks, MA, USA).

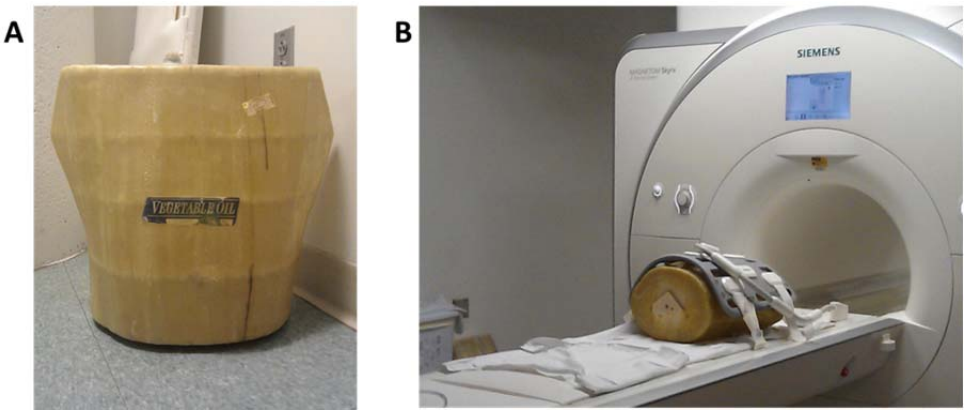

Figure 7.2. A) Torso phantom filled with vegetable oil. B) Experimental setup, cardiac coil with 18 elements in the anterior part plus a spine phased-array with 16 elements in the posterior part

7.2.3 Coil sensitivity maps

A torso phantom filled with vegetable oil was scanned using a combination of a spinal and a cardiac coils in reception, giving a total of 34 channels or coil elements. Two consecutive gradient echo (GRE) sequences were acquired with both the body coil (BC) of the scanner and the phased array (PA) combination mentioned. The sequences had the following parameters: Matrix size = 88x256x208, FOV = 48.8x43.3x31.2 cm^3, TR/TE= 9/2.43 ms, flip angle: 15º, NR_{PA}=1, NR_{BC}=3.

Coil sensitivity maps were extracted following a standard procedure [57]

1. Division of the image obtained with the phased array by the image obtained with the body coil
2. Elimination of regions of pure noise by masking the torso by thresholding
3. Fitting of the point-by-point ratio obtained in step 1 to a 3D complex polynomial to obtain smooth maps inside the area delimited by the mask
4. Sampling the FOV of interest (64x48x24 mm^3) inside the torso. We selected an area centered-towards the left part of the torso as our FOV of interest (an approximate location for coronary vessels). Full-torso sensitivity maps were evaluated at this FOV of interest and interpolated to match the spatial resolution of our data.

Coil configuration was analyzed performing a Singular Value Decomposition (SVD) of the sensitivity maps and calculating the *geometry factor* maps (*g*-factor maps) for different acceleration factors [57]. SVD served to evaluate the independency among elements of the coil and *g*-factor maps were indicative of the SNR reduction that is expected due to an acceleration rate (R) when standard parallel imaging is applied, see equation 7.1.

$$SNR_{\rho}^{red} = \frac{SNR_{\rho}^{full}}{g_{\rho}\sqrt{R}} \qquad [7.1]$$

To evaluate the impact of FOV volume, SVD of sensitivity maps in the full torso FOV was compared against SVD of sensitivity maps in our small FOV of interest (64x48x24 mm^3). Also, the performance of the small FOV sensitivity maps was evaluated at different levels of added Gaussian noise.

g-factor maps were computed according to the following expression:

$$g_{\rho} = \sqrt{\left[\left(C^{t}\Psi^{-1}C\right)^{-1}\right]_{\rho,\rho}\left(C^{t}\Psi^{-1}C\right)_{\rho,\rho}} \qquad [7.2]$$

where C represents the coil sensitivity profiles, Ψ the noise covariance matrix and ρ denotes the voxel under consideration. A prescan noise measurement, Ψ, was acquired and used according to equation 7.2. To evaluate the influence of FOV size and resolution on noise amplification, *g*-factor maps were evaluated at different FOV sizes and resolutions:

- Full-torso FOV: 488x433x312 mm^3 and 1.69x1.69x1.5 mm/pixel resolution
- Intermediate FOV low resolution: 244x216.5x156 mm^3 and 1.69x1.69x1.5 mm/pixel
- Intermediate FOV high resolution: 244x216.5x156 mm^3 and 0.845x0.845x0.75 mm/pixel
- Small inner FOV low resolution: 64x48x24 mm^3 and 0.5x0.5x0.5 mm/pixel
- Small inner FOV high resolution: 64x48x24 mm^3 and 0.745x0.75x0.75 mm/pixel
- Small inner FOV off-centered: 64x48x24 mm^3 and 0.5x0.5x0.5 mm/pixel resolution

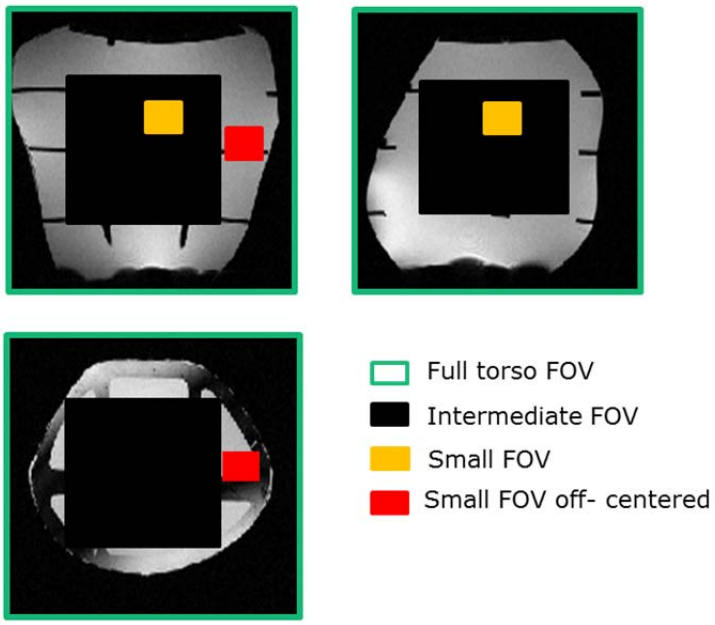

Figure 7.3. Schematic representation of the different FOV tested for the *g*-factor map analysis

7.2.4 Acceleration techniques evaluated

As pure parallel imaging reconstructions, GRAPPA [56] and SENSE [57] were evaluated. The GRAPPA reconstruction used a 3D kernel and 12x24 auto-calibration lines. SENSE was resolved with a least squares iterative implementation. This SENSE algorithm was also tested with a TV regularization term incorporated (SENSE+TV) [145, 146].

To evaluate the performance of compressed sensing, we implemented a 3D multichannel compressed sensing version of the TV-based Split Bregman methodology was implemented [34]. This approach incorporates the knowledge of the coil sensitivity maps to provide a solution of compressed sensing combined with SENSE, such that the joint sparsity of coils is exploited giving only one final image that represents the combination of all coils [80].

$$\min_u \left\|(\nabla_x u, \nabla_y u, \nabla_z u)\right\|_2 \quad \text{such that} \quad \left\|\sum_i \left(RFC_i u - f_i\right)\right\|_2^2 < \sigma^2 \qquad [7.3]$$

Where F represents the Fourier operator, R the undersampling matrix, f_i represents the measured k-spaces, σ^2 is the variance of the signal noise, ∇_j the spatial derivatives, C_i the coil sensitivity profiles and u the sensitivity weighted combination of the phased-array images:

$$u = \sum_i \frac{u_i C_i^*}{C_i^2} \qquad [7.4]$$

Split-Bregman implementation was similar to the one detailed in Chapter 4; although in this case we have to incorporate the summation term and the sensitivity-weighted coil combination into the formulation, thus the following replacements have to be done in equations [4.7],[4.10] [4.11] and [4.12]

$$F^T R^T f \quad \Rightarrow \quad \frac{\sum_i C_i^* F^T R^T f_i}{\sum_i C_i^2} \qquad [7.5]$$

$$RFu \quad \Rightarrow \quad RF\sum_i C_i u \qquad [7.6]$$

Besides, for this formulation u^k cannot be solved in the Fourier domain, thus the system $K(x,t)u(x,t) = r(x,t)$ has to be solved in the image domain. For that purpose, we used a Stabilized Biconjugate Gradient Krylov solver.

For the compressed sensing reconstruction, 3D undersampling patterns were created based on the method described in [51], such that the total acceleration rate was equivalent to the ones used in parallel imaging simulations.

7.2.5 Simulations performed

In the first place, the effect of SNR in the reconstruction was evaluated in absence of motion: 2x1 and 2x2 acceleration rates were simulated for both high SNR and low SNR cases. Acceleration rates are expressed as R_1xR_2 where R_1 is the acceleration rate applied to the first phase-encoding direction and R_2 the acceleration applied to the second phase-encoding direction.

After that, motion was incorporated in the *ex-vivo* data, simulating different values of residual motion and acceleration rates. Residual motion values of 15% and 25% were considered as a representative case. Those datasets were reconstructed for 2x1 and 2x2 accelerations for both high SNR and low SNR cases. The performance of the best reconstruction algorithms was also evaluated assuming higher values of residual motion, 35% and 25% respectively.

It is important to notice that, as we increase the acceleration rate, less data are acquired and thus a higher range of spatial frequencies can be acquired in the 25 s breathold (without motion). Figure 7.4 shows a representation of a 3D k-space and a representation of how the extension of the BIKS is modified depending on the amount of undersampling. As we maintain the same number of phase-encoding lines acquired during breathold, when the rate of undersampling increases, the extension of BIKS, in terms of spatial frequencies, also increases.

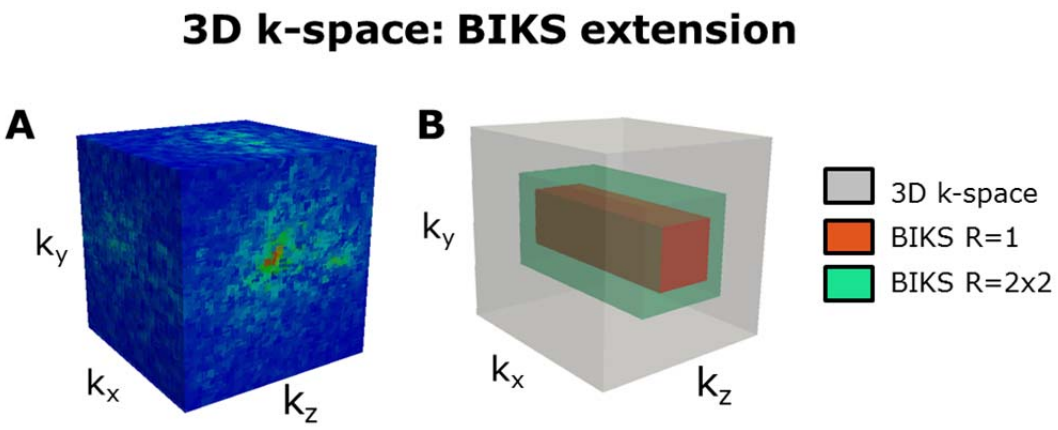

Figure 7.4. Representation of a 3D k-space and extension of BIKS. A) Colormap of a 3D k-space. Higher intensity values are located in the k-space center. B) Representation of the BIKS extension in terms of k-space phased encoding lines. BIKS determines the percentage of phased encoding lines acquired in breathold regimen. When undersampling rates are applied, the extension of BIKS increases: Higher frequencies are acquired

7.2.6 Quality criteria

Ground truth data for the comparisons was obtained as a sensitivity-weighted combination of no-accelerated and no-motion 0.5 mm resolution images. The portions of the vessel with significant plaque features were manually segmented, and normalized root-mean squared error (nRMSE) between the ground truth and reconstructed images was calculated in those segments (average nRMSE ± SE are indicated in all figures). Also, a Jaccard index [147] was computed as a similarity index between original and accelerated plaques.

7.3 Results

A 3D representation of the vegetable-oil torso acquired with the body coil can be seen in figure 7.5-A, small inner FOV is highlighted in black. Figure 7.5-B shows the coil sensitivity maps of the 34 coil elements, evaluated in the full torso FOV and in our small FOV of interest. For each coil element, there is a huge intensity variation across the FOV. On the contrary, in the small FOV case, the intensity variation for each element of the coil is almost constant.

SVD of the coils sensitivity maps is shown in figure 7.5-C. It is easily appreciated that full-torso SVD represents a well-conditioned system; this is an indicative of the independency of the sensitivity maps among different elements. However, when evaluated in the small FOV, singular values obtained are much lower, corresponding to an ill-conditioned system. While in the full-torso case singular values decay two orders of magnitude, in the small FOV case they

decay six orders of magnitude. Despite the small singular values in the latter case, if no perturbation is added to the system, the system can be inverted and the reconstruction process can be done. However, when additional noise is added to the data, as the red and green lines show, the lower singular values are completely masked by the noise, dramatically lowering the number of functional different elements of the coils that we can be used for the reconstruction. This reduction in the number of functional elements of the coil influences directly on the acceleration factor attainable with this coil configuration. This points out that expected acceleration rates will be lower for the small FOV case, as compared with the full torso FOV case.

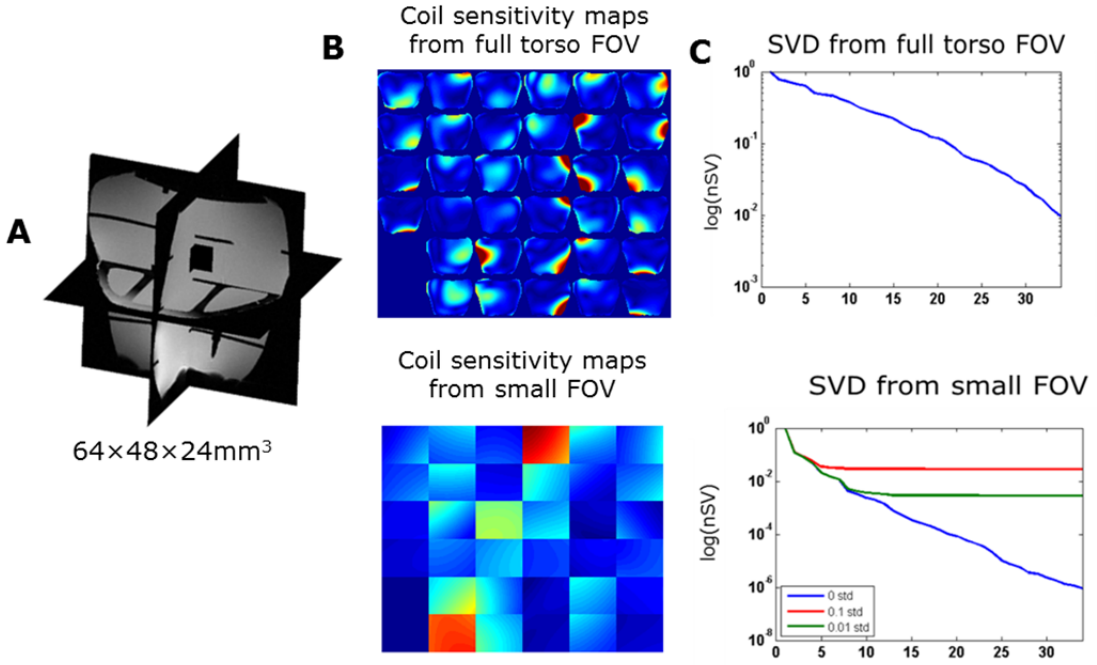

Figure 7.5. A) 3D representation of the vegetable oil torso acquired with a body coil, FOV of interest is marked in black. B) Coil sensitivity maps of the 34 coil elements evaluated in the full torso FOV and in the small FOV of interest. C) SVD representation of the coil sensitivity maps shown in B. While the full torso shows a well-conditioned system, the small FOV reveals that sensitivity maps are ill-conditioned, greatly sensitive to noise. In presence of noise, the number of functionally different coil elements is greatly decreased.

As a complementary measurement, 1/*g*-factor maps are shown in figure 7.6, *g*-factor mean and maximum values are also indicated. This figure clearly illustrates the impact of FOV size and resolution for the different acceleration rates, *g*-factor greatly increases as the FOV is decreased. The higher the *g*-values, the higher the noise amplification will be produced in the accelerated images. As an example, for 3x2 acceleration when the FOV was reduced to its half (intermediate FOV), mean *g*-value changed from 1.1 to 3.6. The difference is even more

dramatic in the case of the smallest FOV; despite its localization it can be seen how the noise will be greatly amplified when accelerating over 2x1, with *g*-factor mean values greater than 20 in all cases.

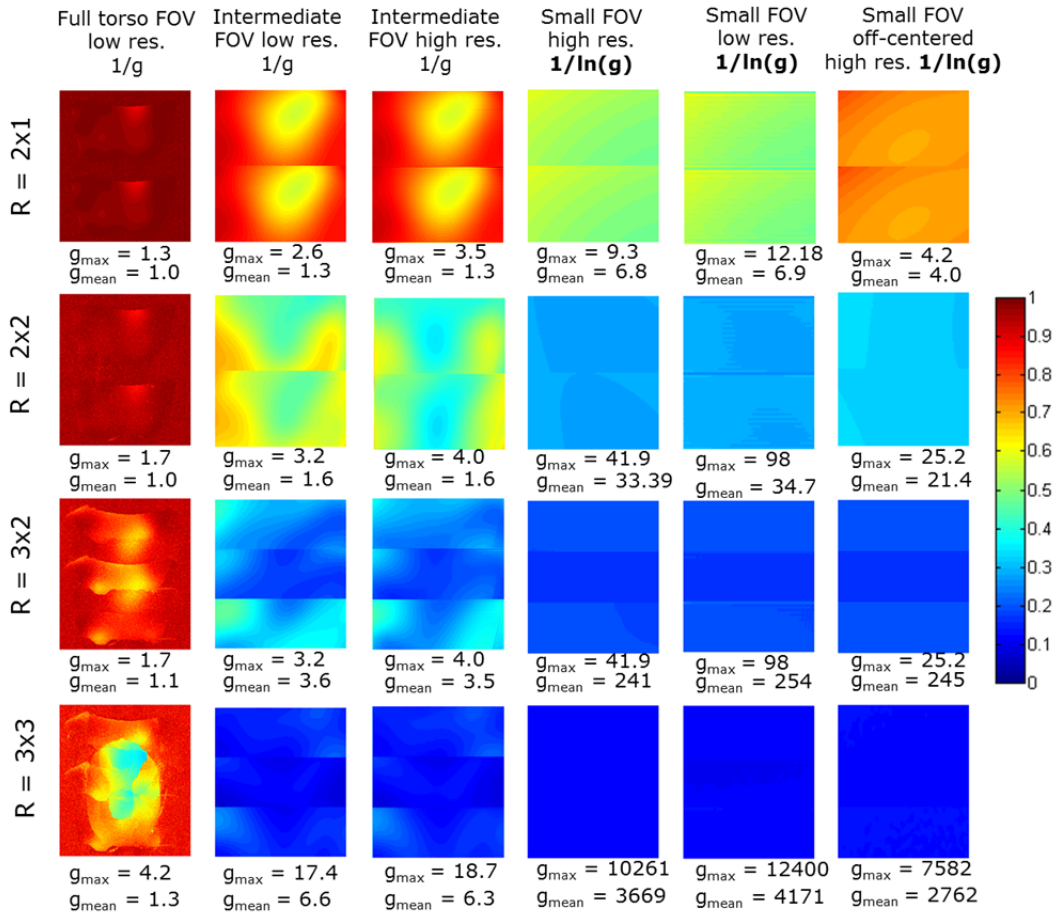

Figure 7.6. Sagittal $1/g$- factor for different FOV, resolution values and acceleration rates

Figure 7.6 also illustrates that resolution has no significant impact on the *g*-factor values; this fact is in agreement with figure 7.7, where the histogram of the different maps is shown for 2x2 accelerations. The range of values of the histogram is different depending on the FOV size, however, it is similar for different resolutions but same FOV.

Figure 7.8 shows the effects of noise and acceleration in absence of coronary motion. It is remarkable the great difference of results between high SNR and low SNR cases. High SNR images are perfectly reconstructed with all the reconstruction techniques, for the two acceleration rates shown. However, differences among the reconstruction algorithms appeared at low SNR. Also, a great difference was found between accelerations 2x1 and 2x2. In this latter case, compressed sensing and SENSE+TV provided the only acceptable reconstructions; SENSE and GRAPPA showed too high noise levels for an accurate plaque visualization.

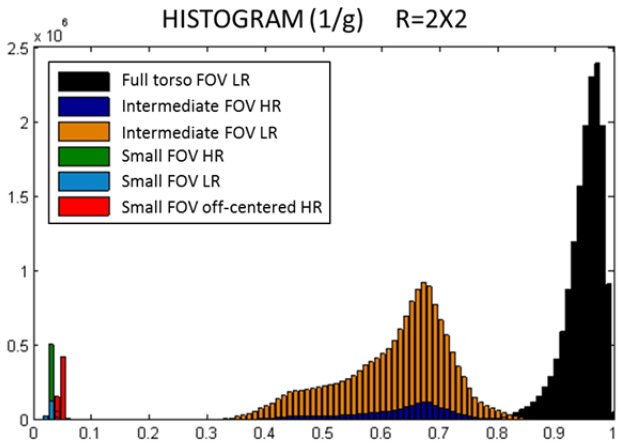

Figure 7.7. Histogram of $1/g$- factor maps for an R=2x2 and different FOV sizes and resolution values. HR: high resolution. LR: low resolution. 1/g values distribution is highly depending on the size of the FOV. However, it is similar for different resolutions but same FOV.

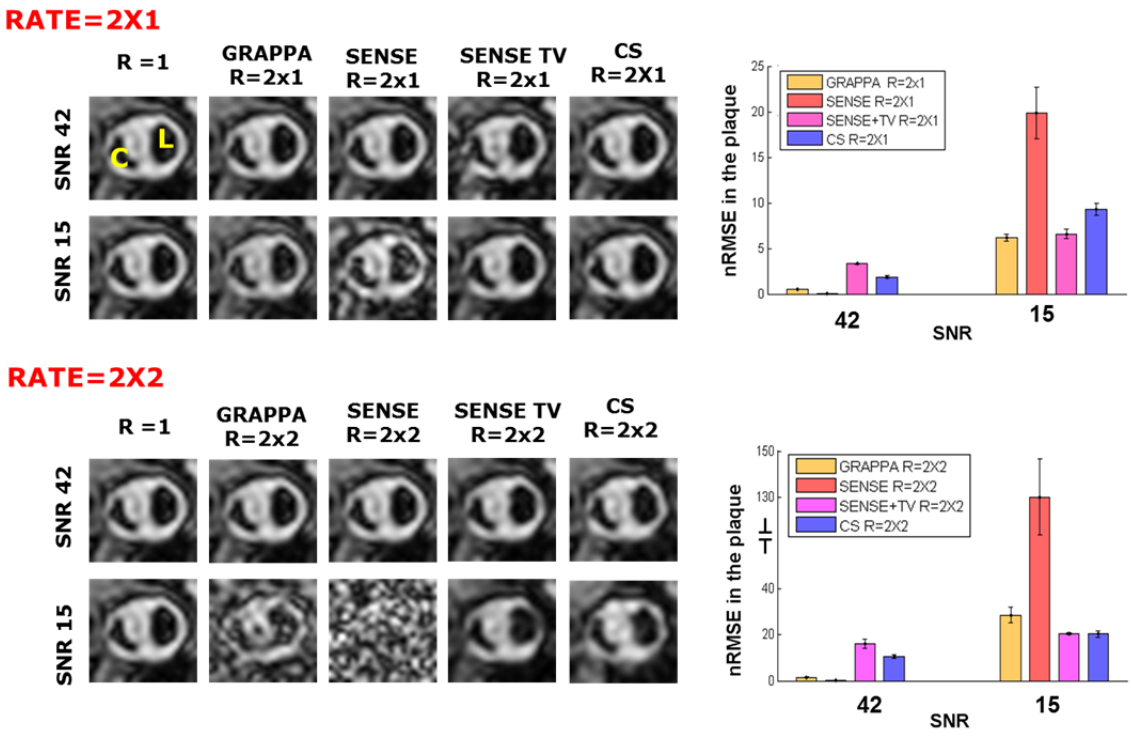

Figure 7.8. A) Impact of acceleration and noise on plaque morphology in absence of coronary motion. The hypointense area on the left (C) is an area of plaque calcification. The vessel lumen is the larger hypointense area on the right (L). With high SNR, 2×2 acceleration is possible with minimal reduction in image quality. However, at a SNR of 15 only 2×2 SENSE+TV and CS (compressed sensing) produces acceptable image quality.

Figure 7.9 presents the result of a 2x1 acceleration rate evaluated in presence of motion, using the 10 *in vivo* motion profiles and the seven atherosclerotic plaques available (n=77). In the high

SNR case, all reconstruction algorithms performed quite similarly, with the exception of compressed sensing that improved the rest, as indicated by both nRMSE values and plaque morphology.

In the low SNR case, it is noticeable how GRAPPA, SENSE+TV and compressed sensing reconstructions make the accelerated images less sensitive to motion; plaque morphology is better defined compared with the image with motion but without any acceleration. Also, a lower nRMSE and a higher Jaccard index indicate that reconstructed images are closer to the original one (without any motion or acceleration). nRMSE decreases from 34 ± 0.92 in absence of acceleration to 31.9 ± 0.94, 31.78 ± 0.92 and 24.77 ± 0.76 for the 2x1 acceleration with GRAPPA, SENSE+TV and compressed sensing respectively.

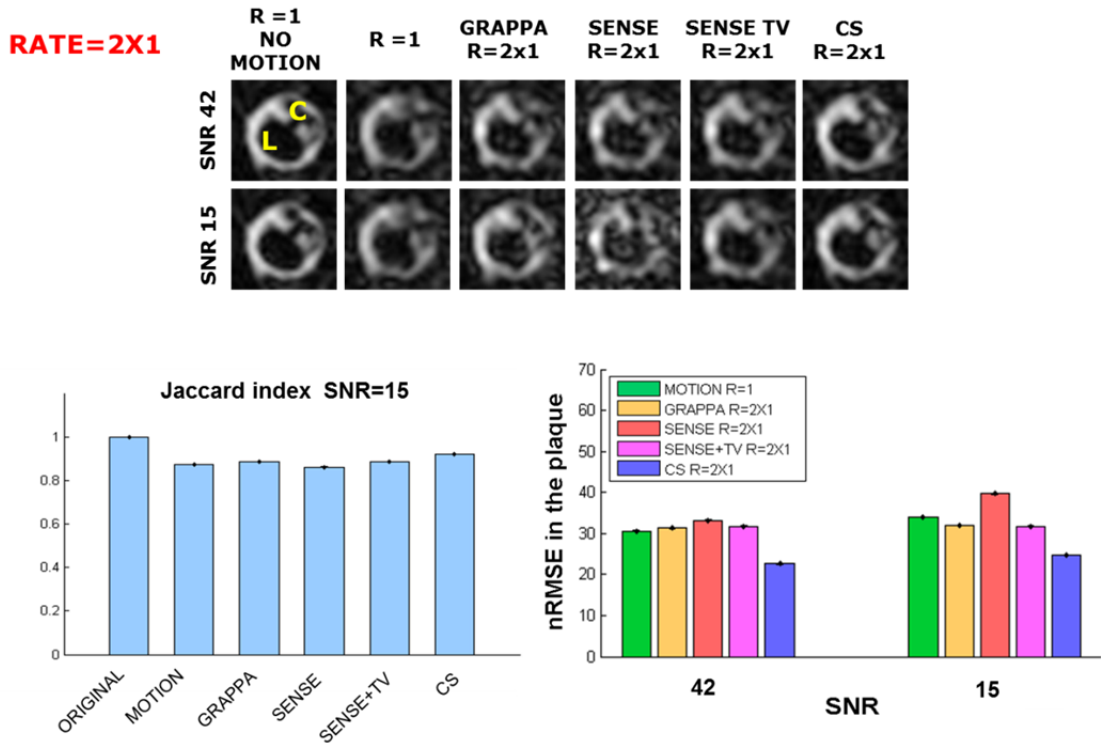

Figure 7.9. Results of a 2x1 acceleration rate, evaluated in presence of coronary motion. For high SNR, compressed sensing (CS) improves the reconstruction of the images without acceleration but with motion. In the low SNR case, accelerated images reconstructed with GRAPPA, SENSE+TV and CS are better than the image with motion but without acceleration. This improvement in motion sensitivity is also reflected in the images and the Jaccard index.

However, the benefits that acceleration techniques potentially have on this particular type of coronary imaging are not present for 2x2 acceleration rate, as can be observed in figure 7.10. For the high SNR case, image quality is just maintained for all the reconstruction techniques. For the more realistic scenario, low SNR, only compressed sensing and SENSE+TV maintain

image quality, with nRMSE values of 33.14 ± 1.43 and 34.95 ± 0.76 respectively, while GRAPPA and SENSE failed in the reconstruction.

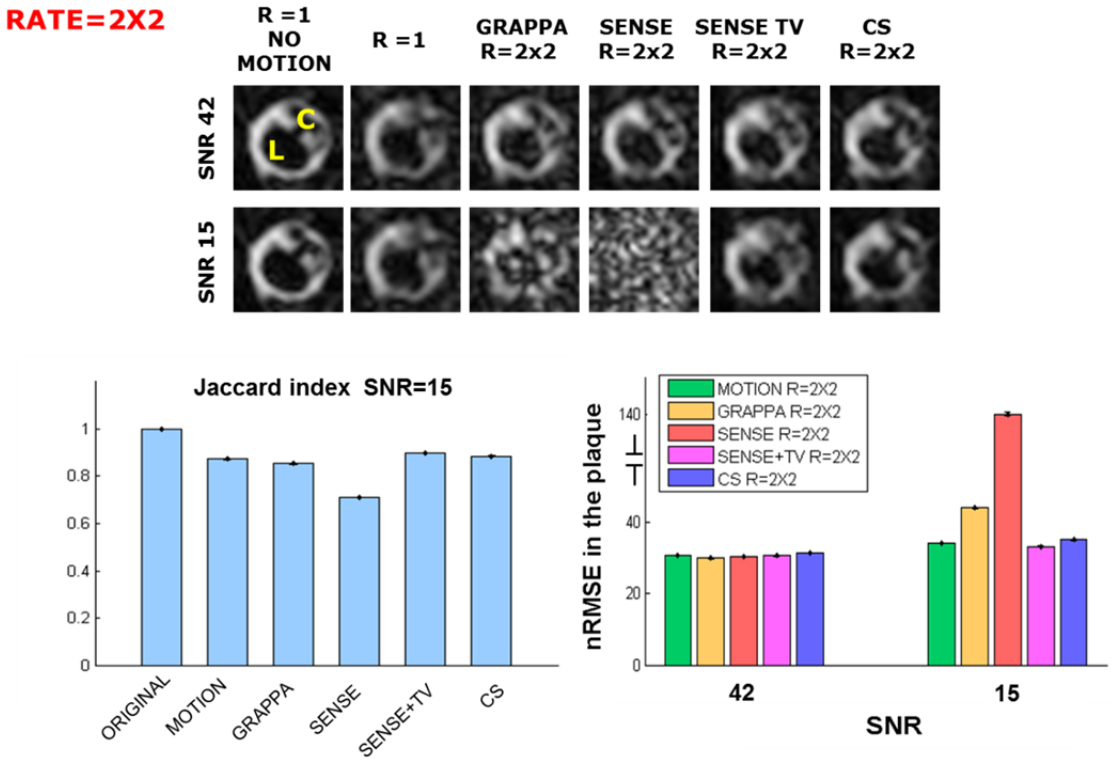

Figure 7.10 Results of a 2x2 acceleration rate evaluated in presence of motion. For high SNR, image quality is maintained for all reconstructions. In the low SNR case, only SENSE+TV and CS maintain image quality; image delineation is similar as well as nRMSE and Jaccard index values

Potential benefits of acceleration were also evaluated in another scenario with higher values of residual motion, as shown in figure 7.11. Compressed sensing and SENSE+TV provided a greater improvement in the case with higher residual motion values, making the images less sensitive to motion. compressed sensing performed better in terms of nRMSE but both algorithms performed similarly in terms of the Jaccard index. nRMSE for higher residual motion values is reduced from 41.77 ± 1.09, in absence of acceleration, to 39.31 ± 0.8 and 37.84 ± 0.78 for SENSE+TV and compressed sensing respectively.

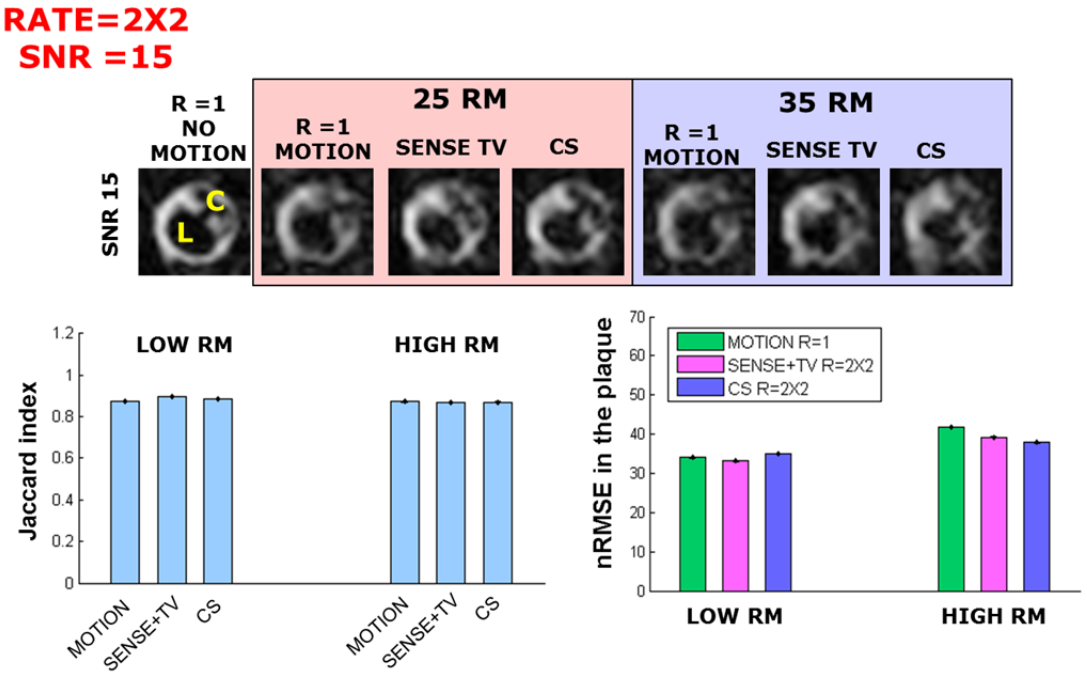

Figure 7.11. Benefits of acceleration for low and high residual motion (RM) values. Compressed sensing (CS) and SENSE+TV improved the nRMSE when working with high residual motion values.

7.4 Discussion

This work aimed to investigate, for the first time, the potential benefits of applying acceleration techniques to the visualization of coronary atherosclerotic plaques *in vivo*. Our hypothesis was that in presence of acceleration, and following a hybrid acquisition scheme, greater parts of the center of k-space could be acquired in absence of motion, thus making images less sensitive to motion besides just reducing acquisition times. However, a great limitation imposed by the size of the FOV of interest was found during the analysis. The small inner FOV used limited the potential benefits that acceleration techniques might provide to coronary atherosclerotic plaque MRI acquisitions.

Simulations performed in absence of motion, SVD and *g*-factor analysis agree in pointing out to a great limitation in acceleration rates due to the small FOV of interest. Singular value decomposition proved a high degree of overlap among coil profiles in the small FOV studied. The lack of independency among coil elements greatly reduces the achievable acceleration factors when the system is not perfect, whenever data are corrupted by noise. Results of simulations corroborated this fact: Good accelerations were achieved for high SNR. In contrast, in a more realistic scenario with low SNR, the acceleration rate could not be increased over 2x2.

The information provided by the *g*-factor maps is a good indicator of the expected noise amplification for parallel imaging reconstructions. The analysis of the different *g*-factor maps proved that indeed the main limitation is imposed by the FOV size, discarding any limitation due to the high resolution required for this type of imaging.

Despite the limitation mentioned above, this work also shows that acceleration techniques can potentially improve the visualization of coronary plaque morphology due to a reduction in motion sensitivity and/or in the acquisition time. This fact was reflected in a reduction of the nRMSE and an increase of the Jaccard index in most of the cases analyzed in presence of motion. 2x1 acceleration factor showed an improvement in motion sensitivity while 2x2 acceleration showed a maintenance of quality for reduced acquisition time. Moreover, for greater amounts of residual motion, and 2x2 acceleration factor with low SNR, this motion sensitivity improvement was also reflected.

In terms of the reconstruction algorithms evaluated, SENSE+TV and compressed sensing always offered the best reconstructions at low SNR, with results superior to standard SENSE and GRAPPA reconstructions. This fact is in agreement with the previous findings in coronary imaging literature, where a better performance of compressed sensing than SENSE was reported; mainly due to the noise amplification produced in the parallel imaging case [83]. Indeed, the TV regularization term present in both the compressed sensing and SENSE+TV algorithms evaluated in this work helped to greatly reduce the impact of noise amplification, at the same time that image details were preserved [94].

Further work can provide improvements in terms of the reconstruction methodology used: Dictionary based compressed sensing algorithms [148, 149] might improve the texture of the reconstructed images while L1-Spirit [78, 79] have shown to successfully combine parallel imaging and compressed sensing. Also other algorithms incorporating motion correction in the reconstruction step [72, 76] should be tested and evaluated. Moreover, a deeper understanding of the interaction of parallel imaging-compressed sensing reconstructions with different undersampling patterns, such random [146] or Poisson-disk [84], should be investigated. Coil compression is another feature than can be easily incorporated in future work [150]. However, all the improvements than can be done in the methodology and in the reconstruction process are strongly subject to the use of a better coil setup.

7.5 Conclusion

In this work a commercial phased-array coil setup was used, proving to be insufficient to accelerate coronary imaging in our small FOV of interest. The benefits that acceleration techniques, such as parallel imaging and compressed sensing, can provide to the visualization of atherosclerotic plaques were greatly limited by the coil setup analyzed.

These findings motivate the design and construction of dedicated cardiac receive arrays for coronary artery imaging, where design criteria should include optimized SNR and coil profiles over the coronary arteries, taking into account the high resolution and small FOV requirements. Such arrays could significantly enhance the impact of accelerating techniques on coronary artery plaque imaging, making the acquisitions faster, less sensitive to motion and therefore within reach.

8. Discussion and Conclusions

The main objective of this thesis was to explore and evaluate the benefits that compressed sensing provides to two leading cardiovascular applications: Cardiac cine acquisitions in small animals and the visualization of coronary atherosclerotic plaques in humans.

In broad terms, there is no doubt about the great impact that compressed sensing has caused in the area of MRI, as the increasing amount of works and patents published in the past years highlights. However, before it reaches its full potential in preclinical and clinical scenarios there are still critical validation steps to carry out [28]. Most of the works published about compressed sensing are focused on developing new algorithms and exploring new applications, its benefits and boundaries. Indeed, this is the first step required for the development of the technique; but to reach effective translation to preclinical and clinical routines those works have to be accompanied by real compressed sensing implementations, routine acquisitions and systematic evaluations. This last part, which is equally essential, has not yet been address in many applications. Systematic evaluations must be carried out by specialists, looking for relevant pathological information and not just focused on the general aspect of image quality [82]. This thesis provides original contributions in terms of compressed sensing methodologies and cardiovascular MR applications, taking into account all the key points mentioned above.

The two cardiovascular applications evaluated in this thesis are at very different stages of development and thus the contributions presented are framed in different phases of their development. The first one, cardiac cine acquisition in small animals is a widely used application in which compressed sensing can be straightforwardly applied. This thesis covers all key steps from the proposal of a new compressed sensing methodology to the implementation of real compressed sensing acquisitions, and a systematic evaluation of the results. While the second application, the visualization of coronary atherosclerotic plaques in humans, is not yet technically feasible. Thus, our work on the application of compressed sensing in this scenario is thus exploratory, limited to the proposal of the methodology and its theoretical evaluation.

Regarding the first application studied, besides just using standard image quality parameters in healthy subjects, in this thesis we also took into account the evaluation of unhealthy animals by using relevant clinical parameters and experts' criteria for the evaluation of the feasible

acceleration factors. Interestingly, we found that achievable accelerations in the case of unhealthy animals might be more moderate than in the case of healthy animals. This is probably due to a worst initial image quality, cardiac motion was restricted in animals that underwent cardiac surgery, and thus navigator signals showed worst quality and the classification of data into different frames was more challenging. In addition, the theoretical analysis was successfully completed with a practical implementation and the study of differences between theoretical and real compressed sensing implementations. As Chapter 5 points, there may exit some mismatch between theoretical and practical results at high acceleration rates. We found different sensitivity to motion events between theoretical simulations and real acquisitions, probably due to a higher temporal coherence of motion in real acquisitions, what makes them more prone to the presence of artifacts at high acceleration factors.

With respect to the second cardiovascular application addressed in this work, we have studied the feasibility and limits of MRI for the visualization of coronary atherosclerotic plaques in humans. Results obtained in Chapters 6 and 7 are entirely based on simulation studies. This should not be considered as a limitation because simulations are indeed a crucial step for future real implementations. In this thesis we proposed a new acquisition scheme for this type of studies, and we defined for the first time the technical requirements to face future *in vivo* acquisitions. Resolution and SNR requirements are technically within reach, and motion proved to be by far the most challenging aspect to overcome.

Acceleration techniques such as parallel imaging and compressed sensing have demonstrated to be essential in other cardiovascular areas, minimizing acquisition times, improving image quality and reducing sensitivity to motion. Thus, acceleration techniques could potentially make the difference allowing the visualization of coronary atherosclerotic plaques to be feasible in practice, providing faster and less sensitive to motion acquisitions. However, the simulations performed in this thesis showed that the coil setup analyzed was not optimal for the small FOV required for the coronary plaque visualization. Therefore, before this application reaches its viability, a joint effort of different MRI research areas has to be made in order to design a dedicated coil for coronary plaque visualization.

The main contributions and conclusions of this thesis are the following:

1. A new complete compressed sensing methodology was proposed and applied to self-gated cardiac cine acquisitions in small animals. This methodology was developed as a modification of the Split Bregman reconstruction algorithm to include the minimization of TV across both spatial and temporal dimensions. The evaluation of both healthy animals

and animals with myocardial infarction, by means of retrospectively undersampled simulations, indicated that acceleration factors of 10 are achievable and suitable for preclinical applications.

2. The previously proposed compressed sensing acquisition was implemented in a 7 T small-animal MR scanner. With this new sequence, we demonstrated that acceleration factors around 10 are achievable in practice, close to those obtained in previous simulations. However, at higher acceleration factors we found higher sensitivity to motion in real compressed sensing acquisitions than in previous simulations.
3. Simulation studies of *ex vivo* coronary human atherosclerotic plaques merged with *in vivo* coronary motion profiles provided valuable information to face future *in vivo* coronary atherosclerotic MRI plaque studies. We proposed a new acquisition scheme, and we defined resolution, SNR and motion thresholds required for accurate classification of atherosclerotic plaques in human. We also demonstrated that a proper motion estimation, together with excellent motion correction, are the greatest challenges to overcome for the consecution of future *in vivo* coronary atherosclerotic plaque evaluation by MRI.
4. The benefits that acceleration techniques, such as parallel imaging and compressed sensing, can provide to the visualization of atherosclerotic plaques in a clinical scenario were carefully studied. Among others, we implemented and evaluated a compressed sensing methodology incorporating the coils sensitivity profile information into the solution of the problem. The standard phased-array coil setup analyzed proved to be inadequate to accelerate coronary imaging, due to the small FOV evaluated. Thus, dedicated phased-arrays must be designed to enhance the benefits that accelerating techniques may provide on coronary artery plaque imaging, faster and less-sensitive-to-motion acquisitions could be then possible.

Future lines of research derived from the present work

Several possible lines for future improvements of the work presented here still remain open:

1. Regarding the algorithms used for the compressed sensing reconstruction, since the beginning of this thesis new excellent algorithms have been published that are great candidates for cardiovascular applications [71, 76, 78, 92, 149]. Our methodology based on Split Bregman minimizing the spatiotemporal TV has demonstrated to be a robust solution with great results in a wide variety of scenarios. However, a comparison of our Split Bregman methodology with other state-of-the-art algorithms will be indeed of interest

2. In terms of the incorporation of the proposed compressed sensing methodology to small-animal preclinical routines, we should overcome the limitation in the number of different undersampling patterns that can be stored in the MR scanner. Besides, future efforts should be addressed to reduce reconstruction times, as real-time reconstructions are essential for the final establishment of the technique
3. In terms of the validation of the compressed sensing methodology presented for self-gated small-animal cine acquisitions, future work should involve whole-heart real compressed sensing acquisitions in both healthy and unhealthy animals, in a higher number of subjects
4. Regarding the resolution, SNR and motion thresholds defined for the accurate classification of atherosclerotic plaques in humans, other acquisition schemes and sequences should be explored, as for example UTE and T2-W sequences.
5. As motion has demonstrated to be the main limiting factor for the acquisition of coronary images *in vivo*, future efforts can be focused on assessing new accurate motion estimation and motion correction strategies [70, 134, 140-142]
6. Clearly the design of dedicated phased-array coils for the imaging of coronary atherosclerotic plaques is of highly interest. New coil designs must be also accompanied by a new analysis of acceleration algorithms and its benefits, as they proved to be highly dependent on the coil configuration
7. We speculate that new algorithms combining parallel imaging and compressed sensing [78, 79] and/or including motion correction [76] [72] would indeed provide great benefits for the visualization of coronary atherosclerotic plaques *in vivo*

9. Publications

9.1 Related to this thesis

Articles in peer-reviewed journals

- **P Montesinos**, JR Polimeni, B Bilgic, SF Cauley, M Desco, R Nezafat, LL Wald, E Adalsteinsson, DE Sosnovik. *"High Resolution Inner Volume Imaging of Human Coronary Atherosclerotic Plaque: Impact and Limits of Parallel Acquisition"* (In preparation)
- **P Montesinos**, H Seifarth, H Bhat, M Desco, F A Jaffe, E Adalsteinsson, U Hoffmann, R Nezafat, D E Sosnovik. *"Motion, Resolution and Noise Thresholds for the Accurate Classification of Human Coronary Atherosclerotic Plaque"*. (Submitted to JCMR)
- JFPJ Abascal*****, **P Montesinos***, E Marinetto, J Pascau, M Desco. *"Comparison of total variation with a motion estimation based compressed sensing approach for self-gated cardiac cine MRI in small animal studies"*. PLoS One, 9(10): e110594 (10 pp.), 2014
- **P Montesinos**, JF PJ Abascal, L Cussó, JJ Vaquero, M Desco. *"Application of the Compressed Sensing Technique to Self-Gated Cardiac Cine Sequences in Small Animals"*. Magn Reson Med, 72(2): 369-380, 2013

International conferences

- **P Montesinos**, JR Polimeni, B Bilgic, SF Cauley, M Desco, R Nezafat, LL Wald, E Adalsteinsson, DE Sosnovik. *"High Resolution Inner Volume Imaging of Human Coronary Atherosclerotic Plaque: Impact and Limits of Parallel Acquisition"*. Proc Intl Soc Mag Reson Med, 22: 0107, 2014
- C Chavarrías, JFPJ Abascal, **P Montesinos**, M Desco. *"How Does Compressed Sensing Affect Activation Maps in Rat fMRI?"*. IFMBE Proceedings, 41: 202-205, 2013
- **P Montesinos**, JFPJ Abascal, C Chavarrías, JJ Vaquero, M Desco. *"Compressed Sensing for Cardiac MRI Cine Sequences: A Real Implementation on a Small-Animal Scanner"*. IFMBE Proceedings, 41: 214-217, 2013
- JFPJ Abascal, **P Montesinos**, E Marinetto, J Pascau, JJ Vaquero, M. Desco. *"A Prior-Based Image Variation (PRIVA) Approach Applied to Motion-Based Compressed Sensing Cardiac Cine MRI"*. IFMBE Proceedings, 41: 233-236, 2013

- **P Montesinos**, H Bhat, G Dai, M Desco, E Adalsteinsson, R Nezafat, D. E. Sosnovik. *"Motion, Resolution and Noise Thresholds for the Accurate Classification of Human Coronary Atherosclerotic Plaque by MRI*". Proc Intl Soc Mag Reson Med, 22: 0882, 2013
- **P Montesinos**, JF Pérez-Juste Abascal, J Chamorro, C Chavarrías, M Benito, JJ Vaquero, M Desco. *"High-Resolution Dynamic Cardiac MRI on Small Animals Using Reconstruction Based on Split Bregman Methodology"*. Abstract book of the IEEE Nuclear Science Symposium and Medical Imaging Conference, 349, 2011

National conferences

- **P Montesinos**, JF Pérez-Juste Abascal, J Chamorro, C Chavarrías, M Benito, JJ Vaquero, M Desco. *"Uso del método de Split Bregman para la resolución del problema de compressed sensing en imagen de resonancia magnética dinámica cardiaca para pequeño animal"*. Libro de actas del XXIX Congreso Anual de la Sociedad Española de Ingeniería Biomédica (CASEIB), 453-456, 2011

9.1 Other publications

Articles in peer-reviewed journals

- S Veintemillas-Verdaguer, Y Luengo, C J Serna, M Andrés-Vergés, M Varela, M Calero, A Lazaro-Carrillo, A Villanueva, A Sisniega, **P Montesinos**, M P Morales. *"Bismuth labeling for the CT assessment of local administration of magnetic nanoparticles"*. Nanotechnology 26 135101, 2015
- G Elvira, I García, J Gallo, M Benito, **P Montesinos**, E Holgado-Martín, A Ayuso-Sacido, S Penadés, M Desco, A Silva, JA García-Sanz. *"Detection of mouse endogenous type B astrocytes migrating towards brain lesions"*. Stem Cell Res, 14(1): 114-129, 2015
- PM Gordaliza, JM Mateos-Pérez, **P Montesinos**, J Guzmán de Villoria, M Desco, JJ Vaquero. *"Development and validation of an open source quantification tool for DSC-MRI studies"*. Comput Biol Med, 58: 56-62, 2015

International conferences

- JJ Vaquero, **P Montesinos**, L Cussó, V García-Vázquez, M Desco. *"In-line high resolution PET and 3T MRI hybrid device for preclinical multimodal imaging"*. EJNMMI Physics, 1(Suppl. 1): A7, 2014
- V García-Vázquez, L Cussó, J Chamorro-Servent, I Mirones, J García-Castro, L López-Sánchez, S Peña-Zalbidea, **P Montesinos**, C Chavarrías, J Pascau, M Desco. *"Registration of Small-Animal SPECT/MRI Studies for Tracking Human Mesenchymal Stem Cells"*. IFMBE Proceedings, 41: 399-402, 2013
- M Benito, A Rodríguez-Ruano, C Chavarrías, **P Montesinos**, M Desco. *"Vessel contrast in Susceptibility Weigthed Imaging (SWI) under inhalated anesthesia with different oxygen pressure"*. Proc Intl Soc Mag Reson Med, 18: 4451, 2010
- **P Montesinos**, A Rodríguez-Ruano, M Benito, JJ Vaquero, M Desco. *"Effect of different interpolation methods on the accuracy of the reconstruction of spiral K-Space trajectories in MRI"*. Abstract book of European Society for Molecular Imaging (ESMI), 171, 2009
- M Benito, S Fernández, **P Montesinos**, JJ Vaquero, C Chavarrías, M Desco. *"Fat composition assessment by 1H and 13C spectroscopy in mice"*. Proc Intl Soc Mag Reson Med, 17: 4345, 2009
- A Rodríguez-Ruano, M Benito, C Santa Marta, G Elvira, **P Montesinos**, JJ Vaquero, A Silva, M Desco. *"Quantification of SPIO using T2* and phase imaging"*. Proc Intl Soc Mag Reson Med, 17: 4457, 2009
- J Pascau, **P Montesinos**, M Benito, JJ Vaquero, C Santa Marta, M Desco. *"Validation of rat brain MR image intensity non-uniformity correction using surface coil images"*. Abstract book of European Society for Molecular Imaging (ESMI), 173, 2009
- **P Montesinos**, A Rodríguez-Ruano, M Benito, C Santa Marta, JJ Vaquero, M Desco.*"Quantitative comparison of partial fourier reconstruction algorithms in MRI at 7T"*. Abstract book of European Society for Molecular Imaging (ESMI), 172, 2009

National conferences

- C Simon-Martinez, M Torres, **P Montesinos**, E Bravo-Esteban, S Albu, J Gomez-Soriano, A Ferrer-Donato, I Galan-Arriero, G Avila-Martin, J Taylor. “Clinical impact of

hemorrhage secondary to spinal cord injury on somatosensory function". International Conference on Recent Advances in Neurorehabilitation, Spain; 03/2013

- **P Montesinos**, M Benito, C Chavarrías, JJ Vaquero, M Desco. *"MP2RAGE: una secuencia ponderada en T1 puro insensible a densidad protónica, contraste T2* e inhomogeneidades de campo"*. Proceedings del XXVIII Congreso Anual de la Sociedad Española de Ingeniería Biomédica (CASEIB), s.p., 2010
- E Marinetto, M Desco, **P Montesinos**, J Pascau. *"Corrección de artefacto de inhomogeneidad en imágenes de resonancia magnética de pequeños animales"*. Libro de actas del XXVIII Congreso Anual de la Sociedad Española de Ingeniería Biomédica (CASEIB), 125, 2010
- M Benito, S Fernández, C Chavarrías, **P Montesinos**, JJ Vaquero, M Desco.*"Determinación de la composición corporal y lípidica in vivo mediante imagen y espectroscopía de RM 1H/13C"*. Libro de Resúmenes del CASEIB 2009, 58, 2009
- **P Montesinos**, A Rodríguez-Ruano, M Benito, JJ Vaquero, M Desco. *"Efecto de diferentes métodos de interpolación en la reconstrucción de adquisiciones de trayectoria espiral en el espacio-k en IRM"*. Actas del XXVII Congreso Anual de la Sociedad Española de Ingeniería Biomédica, 149-152, 2009
- **P Montesinos**, A Rodríguez-Ruano, M Benito, C Santa Marta, JJ Vaquero, M Desco."Comparación cuantitativa de algoritmos de reconstrucción de Fourier parcial en IRM a 7 T". Actas del XXVII Congreso Anual de la Sociedad Española de Ingeniería Biomédica, 133-136, 2009
- C Chavarrías, M Benito, **P Montesinos**, V García-Vázquez, J Taylor, E Goiriena, M Desco."Adquisición de imágenes de resonancia magnética funcional (fMRI) en cerebro de rata". Actas del XXVII Congreso Anual de la Sociedad Española de Ingeniería Biomédica, 117-120, 2009

10. References

1. Usman, M., et al., *A computationally efficient OMP-based compressed sensing reconstruction for dynamic MRI.* Physics in Medicine and Biology, 2011. **56**(7): p. N99-N114.
2. Usman, M., et al., *k-t Group sparse: a method for accelerating dynamic MRI.* Magn Reson Med, 2011. **66**(4): p. 1163-76.
3. Montefusco, L.B., et al., *A fast compressed sensing approach to 3D MR image reconstruction.* IEEE Trans Med Imaging, 2011. **30**(5): p. 1064-75.
4. Wech, T., et al., *Accelerating Cine-MR Imaging in Mouse Hearts Using Compressed Sensing.* Journal of Magnetic Resonance Imaging, 2011. **34**(5): p. 1072-1079.
5. Goud, S., Y. Hu, and M. Jacob, *Real-time cardiac MRI using low-rank and sparsity penalties*, in *2010 7th Ieee International Symposium on Biomedical Imaging: from Nano to Macro*. 2010, Ieee: New York. p. 988-991.
6. Otazo, R., et al., *Combination of Compressed Sensing and Parallel Imaging for Highly Accelerated First-Pass Cardiac Perfusion MRI.* Magnetic Resonance in Medicine, 2010. **64**(3): p. 767-776.
7. Moghari, M.H., et al., *Compressed-Sensing Motion Compensation (CosMo): A Joint Prospective-Retrospective Respiratory Navigator for Coronary MRI.* Magnetic Resonance in Medicine, 2011. **66**(6): p. 1674-1681.
8. Wech, T., et al., *Highly accelerated cardiac functional MRI in rodent hearts using compressed sensing and parallel imaging at 9.4T.* Journal of Cardiovascular Magnetic Resonance, 2012. **14**(Suppl 1): p. P65.
9. Wech, T., et al., *Accurate infarct-size measurements from accelerated, compressed sensing reconstructed cine-MRI images in mouse hearts.* Journal of Cardiovascular Magnetic Resonance, 2012. **14**(Suppl 1): p. P57.
10. Motaal, A.G., et al., *Accelerated high-frame-rate mouse heart cine-MRI using compressed sensing reconstruction.* Nmr in Biomedicine, 2013. **26**(4): p. 451-457.
11. Christodoulou, A.G., et al., *High-Resolution Cardiac MRI Using Partially Separable Functions and Weighted Spatial Smoothness Regularization*, in *2010 Annual International Conference of the Ieee Engineering in Medicine and Biology Society*, Ieee: New York. p. 871-874.
12. Oei, M.L., et al., *T1-weighted MRI for the detection of coronary artery plaque haemorrhage.* Eur Radiol, 2010. **20**(12): p. 2817-23.
13. Fayad, Z.A., et al., *Noninvasive in vivo human coronary artery lumen and wall imaging using black-blood magnetic resonance imaging.* Circulation, 2000. **102**(5): p. 506-10.
14. Yeon, S.B., et al., *Delayed-enhancement cardiovascular magnetic resonance coronary artery wall imaging: comparison with multislice computed tomography and quantitative coronary angiography.* J Am Coll Cardiol, 2007. **50**(5): p. 441-7.
15. Saam, T., et al., *The vulnerable, or high-risk, atherosclerotic plaque: noninvasive MR imaging for characterization and assessment.* Radiology, 2007. **244**(1): p. 64-77.
16. Yuan, C., et al., *In vivo accuracy of multispectral magnetic resonance imaging for identifying lipid-rich necrotic cores and intraplaque hemorrhage in advanced human carotid plaques.* Circulation, 2001. **104**(17): p. 2051-6.

17. Hatsukami, T.S., et al., *Visualization of fibrous cap thickness and rupture in human atherosclerotic carotid plaque in vivo with high-resolution magnetic resonance imaging.* Circulation, 2000. **102**(9): p. 959-64.

18. Cai, J.M., et al., *Classification of human carotid atherosclerotic lesions with in vivo multicontrast magnetic resonance imaging.* Circulation, 2002. **106**(11): p. 1368-73.

19. Millon, A., et al., *High-resolution magnetic resonance imaging of carotid atherosclerosis identifies vulnerable carotid plaques.* J Vasc Surg, 2013. **57**(4): p. 1046-1051 e2.

20. Karolyi, M., et al., *Classification of Coronary Atherosclerotic Plaques Ex Vivo With T1, T2, and Ultrashort Echo Time CMR.* JACC Cardiovasc Imaging, 2013. **6**(4): p. 466-74.

21. Desco, M. and J.J. Vaquero, *Imagen Molecular.* Profesión Veterinaria, 2009. **año 16, nº 70** (Diciembre 2008-Marzo 2009): p. 68-76.

22. Weissleder, R. and U. Mahmood, *Molecular Imaging.* Radiology, 2001. **219**(2): p. 316-333.

23. Gibby, W., *Nuclear Magnetic Resonance (NMR) Principles*, in *Neuroimaging*, R. Zimmerman, W. Gibby, and R. Carmody, Editors. 2000, Springer New York. p. 65-82.

24. Bernstein, M.A., K.F. King, and X.J. Zhou, *Handbook of MRI pulse sequences*. 2004, Amsterdam: Elsevier Academic Press.

25. Liang, Z.-P. and P. Lauterbur, *Principles of Magnetic Resonance Imaging: A Signal Processing Perspective*. 1999: {Wiley-IEEE Press}.

26. Morris, G.A., *Spin dynamics: Basics of nuclear magnetic resonance, second edition. Malcolm H. Levitt. Wiley Chichester. 2008. pp xxv + 714. ISBN 978-0-470-51118-3(hbk) 978-0-470-51117-6 (pbk).* NMR in Biomedicine, 2009. **22**(2): p. 240-241.

27. Radiology, P.O.E.S.o., *MR ten years from now: potential and challenges* in *European Congress of Radiology*. 2011.

28. Axel, L. and D.K. Sodickson, *The need for speed: accelerating CMR imaging assessment of cardiac function.* JACC Cardiovasc Imaging, 2014. **7**(9): p. 893-5.

29. Kwong, R.Y. and P. Libby, *Cardiovascular Magnetic Resonance Imaging* CONTEMPORARY CARDIOLOGY, ed. S.-V.B. H. 2007.

30. Bovens, S.M., et al., *Evaluation of infarcted murine heart function: comparison of prospectively triggered with self-gated MRI.* Nmr in Biomedicine, 2011. **24**(3): p. 307-315.

31. Nahrendorf, M., et al., *Cardiac magnetic resonance imaging in small animal models of human heart failure.* Medical image analysis, 2003. **7**(3): p. 369-375.

32. Berr, S.S., et al., *Black blood gradient echo cine magnetic resonance imaging of the mouse heart.* Magnetic Resonance in Medicine, 2005. **53**(5): p. 1074-1079.

33. Kober, F., et al., *Cine-MRI assessment of cardiac function in mice anesthetized with ketamine/xylazine and isoflurane.* Magnetic Resonance Materials in Physics, Biology and Medicine, 2004. **17**(3-6): p. 157-161.

34. Montesinos, P., et al., *Application of the compressed sensing technique to self-gated cardiac cine sequences in small animals.* Magn Reson Med, 2014. **72**(2): p. 369-80.

35. Tsao, J. and S. Kozerke, *MRI temporal acceleration techniques.* J Magn Reson Imaging, 2012. **36**(3): p. 543-60.

36. Gallino, A., et al., *"In vivo" imaging of atherosclerosis.* Atherosclerosis, 2012. **224**(1): p. 25-36.

37. Lavin, B., et al., *Current Development of Molecular Coronary Plaque Imaging using Magnetic Resonance Imaging towards Clinical Application.* Current Cardiovascular Imaging Reports, 2014. **7**(12): p. 1-14.

38. Walter, T.C., et al., *The Great Migration: How MRI Replaces Traditional Imaging Techniques for the Characterization of Atherosclerosis.* Current Radiology Reports, 2014. **2**(3): p. 1-11.

39. Naghavi, M., et al., *From vulnerable plaque to vulnerable patient: a call for new definitions and risk assessment strategies: Part I.* Circulation, 2003. **108**(14): p. 1664-72.

40. Garcia-Garcia, H.M., et al., *Imaging plaques to predict and better manage patients with acute coronary events.* Circ Res, 2014. **114**(12): p. 1904-17.

41. DeLaPaz, R.L., *Echo-planar imaging.* Radiographics, 1994. **14**(5): p. 1045-1058.

42. Feinberg, D. and K. Oshio, *GRASE (gradient-and spin-echo) MR imaging: a new fast clinical imaging technique.* Radiology, 1991. **181**(2): p. 597-602.

43. Bernstein, M.A., S.B. Fain, and S.J. Riederer, *Effect of windowing and zero-filled reconstruction of MRI data on spatial resolution and acquisition strategy.* J Magn Reson Imaging, 2001. **14**(3): p. 270-80.

44. Margosian, P.M., G. DeMeester, and H. Liu, *Partial Fourier Acquisition in MRI*, in *eMagRes*. 2007, John Wiley & Sons, Ltd.

45. Blum, M.J., et al. *Fast magnetic resonance imaging using spiral trajectories*. in *The Marketplace for Industrial Lasers*. 1987: International Society for Optics and Photonics.

46. Glover, G.H., *Simple analytic spiral K-space algorithm.* Magn Reson Med, 1999. **42**(2): p. 412-5.

47. Rasche, V., D. Holz, and W. Schepper, *Radial turbo spin echo imaging.* Magnetic Resonance in Medicine, 1994. **32**(5): p. 629-638.

48. Mansfield, P., *Real-time echo-planar imaging by NMR.* Br Med Bull, 1984. **40**(2): p. 187-90.

49. Rzedzian, R., et al., *Echo planar imaging in paediatrics: real-time-nuclear magnetic resonance.* Ann Radiol (Paris), 1984. **27**(2-3): p. 182-6.

50. Pipe, J.G., *Motion correction with PROPELLER MRI: application to head motion and free-breathing cardiac imaging.* Magn Reson Med, 1999. **42**(5): p. 963-9.

51. Lustig, M., D. Donoho, and J.M. Pauly, *Sparse MRI: The application of compressed sensing for rapid MR imaging.* Magnetic Resonance in Medicine, 2007. **58**(6): p. 1182-1195.

52. Lustig, M., et al., *Compressed Sensing MRI.* Signal Processing Magazine, IEEE, 2008. **25**(2): p. 72-82.

53. Song, T., et al., *Optimal k-space sampling for dynamic contrast-enhanced MRI with an application to MR renography.* Magn Reson Med, 2009. **61**(5): p. 1242-8.

54. Roemer, P.B., et al., *The NMR phased array.* Magn Reson Med, 1990. **16**(2): p. 192-225.

55. Sodickson, D.K. and W.J. Manning, *Simultaneous acquisition of spatial harmonics (SMASH): fast imaging with radiofrequency coil arrays.* Magn Reson Med, 1997. **38**(4): p. 591-603.

56. Griswold, M.A., et al., *Generalized autocalibrating partially parallel acquisitions (GRAPPA).* Magn Reson Med, 2002. **47**(6): p. 1202-10.

57. Pruessmann, K.P., et al., *SENSE: sensitivity encoding for fast MRI.* Magn Reson Med, 1999. **42**(5): p. 952-62.

58. Griswold, M.A., et al., *Partially parallel imaging with localized sensitivities (PILS).* Magn Reson Med, 2000. **44**(4): p. 602-9.

59. Blaimer, M., et al., *SMASH, SENSE, PILS, GRAPPA: How to Choose the Optimal Method.* Topics in Magnetic Resonance Imaging, 2004. **15**(4): p. 223-236.

60. Niendorf, T. and D.K. Sodickson, *Parallel imaging in cardiovascular MRI: methods and applications.* NMR Biomed, 2006. **19**(3): p. 325-41.

61. Madore, B., G.H. Glover, and N.J. Pelc, *Unaliasing by fourier-encoding the overlaps using the temporal dimension (UNFOLD), applied to cardiac imaging and fMRI.* Magn Reson Med, 1999. **42**(5): p. 813-28.

62. Kellman, P., F.H. Epstein, and E.R. McVeigh, *Adaptive sensitivity encoding incorporating temporal filtering (TSENSE).* Magn Reson Med, 2001. **45**(5): p. 846-52.

63. Breuer, F.A., et al., *Dynamic autocalibrated parallel imaging using temporal GRAPPA (TGRAPPA).* Magn Reson Med, 2005. **53**(4): p. 981-5.

64. Tsao, J., P. Boesiger, and K.P. Pruessmann, *k-t BLAST and k-t SENSE: dynamic MRI with high frame rate exploiting spatiotemporal correlations.* Magn Reson Med, 2003. **50**(5): p. 1031-42.

65. Pedersen, H., et al., *k-t PCA: temporally constrained k-t BLAST reconstruction using principal component analysis.* Magn Reson Med, 2009. **62**(3): p. 706-16.

66. Feng, L., et al., *Highly accelerated real-time cardiac cine MRI using k-t SPARSE-SENSE.* Magn Reson Med, 2013. **70**(1): p. 64-74.

67. Jung, H., et al., *k-t FOCUSS: a general compressed sensing framework for high resolution dynamic MRI.* Magn Reson Med, 2009. **61**(1): p. 103-16.

68. Jung, H., J.C. Ye, and E.Y. Kim, *Improved k-t BLAST and k-t SENSE using FOCUSS.* Phys Med Biol, 2007. **52**(11): p. 3201-26.

69. Abascal, J.F.P.J., et al. *A Prior-Based Image Variation (PRIVA) Approach Applied to Motion-Based Compressed Sensing Cardiac Cine MRI*. in *XIII Mediterranean Conference on Medical and Biological Engineering and Computing 2013 (MEDICON)*. 2013. Sevilla: España.

70. Bhat, H., et al., *3D radial sampling and 3D affine transform-based respiratory motion correction technique for free-breathing whole-heart coronary MRA with 100% imaging efficiency.* Magn Reson Med, 2011. **65**(5): p. 1269-77.

71. Abascal, J.F., et al., *Comparison of total variation with a motion estimation based compressed sensing approach for self-gated cardiac cine MRI in small animal studies.* PLoS One, 2014. **9**(10): p. e110594.

72. Usman, M., et al., *Motion corrected compressed sensing for free-breathing dynamic cardiac MRI.* Magn Reson Med, 2013. **70**(2): p. 504-16.

73. Bilen, C., et al., *On compressed sensing in parallel MRI of cardiac perfusion using temporal wavelet and TV regularization.* 2010 IEEE International Conference on Acoustics Speech and Signal Processing (ICASSP). 2010: p. 630-633.

74. Lingala, S.G., et al., *Accelerated dynamic MRI exploiting sparsity and low-rank structure: k-t SLR.* IEEE Trans Med Imaging, 2011. **30**(5): p. 1042-54.

75. Moghari, M.H., et al., *Compressed-sensing motion compensation (CosMo): a joint prospective-retrospective respiratory navigator for coronary MRI.* Magn Reson Med, 2011. **66**(6): p. 1674-81.

76. Bonanno, G., et al., *Self-navigation with compressed sensing for 2D translational motion correction in free-breathing coronary MRI: a feasibility study.* PLoS One, 2014. **9**(8): p. e105523.

77. Akcakaya, M., et al., *Low-dimensional-structure self-learning and thresholding: regularization beyond compressed sensing for MRI reconstruction.* Magn Reson Med, 2011. **66**(3): p. 756-67.

78. Weller, D.S., S. Ramani, and J.A. Fessler, *Augmented Lagrangian with variable splitting for faster non-Cartesian L1-SPIRiT MR image reconstruction.* IEEE Trans Med Imaging, 2014. **33**(2): p. 351-61.

79. Murphy, M., et al., *Fast <formula formulatype="inline"> <img src="/images/tex/19122.gif" alt="\ell _1"> </formula>-SPIRiT Compressed Sensing Parallel Imaging MRI: Scalable Parallel Implementation and Clinically Feasible Runtime.* Medical Imaging, IEEE Transactions on, 2012. **31**(6): p. 1250-1262.

80. Cauley, S.F., et al., *Fast reconstruction for multichannel compressed sensing using a hierarchically semiseparable solver.* Magnetic Resonance in Medicine, 2014: p. n/a-n/a.

81. Liang, D., et al., *Accelerating SENSE using compressed sensing.* Magn Reson Med, 2009. **62**(6): p. 1574-84.

82. Vincenti, G., et al., *Compressed Sensing Single-Breath-Hold CMR for Fast Quantification of LV Function, Volumes, and Mass.* JACC Cardiovasc Imaging, 2014.

83. Akcakaya, M., et al., *Accelerated isotropic sub-millimeter whole-heart coronary MRI: Compressed sensing versus parallel imaging.* Magn Reson Med, 2013.

84. Vasanawala, S.S., et al. *Practical parallel imaging compressed sensing MRI: Summary of two years of experience in accelerating body MRI of pediatric patients*. in *Biomedical Imaging: From Nano to Macro, 2011 IEEE International Symposium on*. 2011.

85. Donoho, D.L., *Compressed sensing.* Ieee Transactions on Information Theory, 2006. **52**(4): p. 1289-1306.

86. Candes, E.J., J. Romberg, and T. Tao, *Robust uncertainty principles: Exact signal reconstruction from highly incomplete frequency information.* Ieee Transactions on Information Theory, 2006. **52**(2): p. 489-509.

87. Candès, E.J., J.K. Romberg, and T. Tao, *Stable signal recovery from incomplete and inaccurate measurements.* Communications on Pure and Applied Mathematics, 2006. **59**(8): p. 1207-1223.

88. Candès, E. and J. Romberg, *Sparsity and incoherence in compressive sampling.* Inverse Problems, 2007. **23**(3): p. 969-985.

89. Usman, M., et al., *A computationally efficient OMP-based compressed sensing reconstruction for dynamic MRI.* Physics in Medicine and Biology, 2011. **56**(Article): p. N99 - N114.

90. Tropp, J.A. and A.C. Gilbert, *Signal Recovery From Random Measurements Via Orthogonal Matching Pursuit.* Information Theory, IEEE Transactions on, 2007. **53**(12): p. 4655-4666.

91. Blumensath, T. and M.E. Davies, *Iterative hard thresholding for compressed sensing.* Applied and Computational Harmonic Analysis, 2009. **27**(3): p. 265-274.

92. Otazo, R., E. Candès, and D.K. Sodickson, *Low-rank plus sparse matrix decomposition for accelerated dynamic MRI with separation of background and dynamic components.* Magnetic Resonance in Medicine, 2015. **73**(3): p. 1125-1136.

93. Dong, L., et al., *K-T ISD: Compressed sensing with iterative support detection for dynamic MRI.* IEEE International Symposium on Biomedical Imaging: From Nano to Macro 2011.

94. Goldstein, T. and S. Osher, *The Split Bregman Method for L1-Regularized Problems.* Siam Journal on Imaging Sciences, 2009. **2**(2): p. 323-343.

95. Gilboa, G., *A Total Variation Spectral Framework for Scale and Texture Analysis.* SIAM Journal on Imaging Sciences, 2014. **7**(4): p. 1937-1961.

96. Wang, Y.L., et al., *A New Alternating Minimization Algorithm for Total Variation Image Reconstruction.* Siam Journal on Imaging Sciences, 2008. **1**(3): p. 248-272.

97. Bregman, L.M., *The relaxation method of finding the common point of convex sets and its application to the solution of problems in convex programming.* USSR Computational Mathematics and Mathematical Physics, 1967. **7**(3): p. 200-217.

98. Osher, S., et al., *An iterative regularization method for total variation-based image restoration.* Multiscale Modeling & Simulation, 2005. **4**(2): p. 460-489.

99. Abascal, J., et al., *Fluorescence diffuse optical tomography using the split Bregman method.* Medical Physics, 2011. **38**(11): p. 6275-6284.

100. Shi, Y. and Q. Chang, *Efficient Algorithm for Isotropic and Anisotropic Total Variation Deblurring and Denoising.* Journal of Applied Mathematics, 2013. **2013**: p. 14.

101. Wang, Y., et al., *A fast algorithm for image deblurring with total variation regularization.* Technical Reports 2007. **TR07-10**.

102. Yin, W., et al., *Bregman Iterative Algorithms for ℓ_1-Minimization with Applications to Compressed Sensing.* SIAM J. Img. Sci., 2008. **1**(1): p. 143-168.

103. Shepp, L.A. and B.F. Logan, *The Fourier reconstruction of a head section.* Nuclear Science, IEEE Transactions on, 1974. **21**(3): p. 21-43.

104. Aggarwal, N. and Y. Bresler, *Patient-adapted reconstruction and acquisition dynamic imaging method (PARADIGM) for MRI.* Inverse Problems, 2008. **24**(4): p. 29.

105. Lustig, M., et al., *k-t SPARSE : High frame rate dynamic MRI exploiting spatio-temporal sparsity.* Proceedings of the 14th Annual Meeting of ISMRM, Seattle, Washington, USA, 2006: p. 2420.

106. Brinegar, C., et al., *Real-time cardiac MRI using prior spatial-spectral information.* Engineering in Medicine and Biology Society, 2009. EMBC 2009. Annual International Conference of the IEEE, 2009: p. 4383-4386.

107. Zhao, B., J.P. Haldar, and Z.P. Liang, *PSF Model-Based Reconstruction with Sparsity Constraint: Algorithm and Application to Real-Time Cardiac MRI.* Annual International Conference of the IEEE Engineering in Medicine and Biology Society, 2010: p. 3390-3393.

108. He, L., et al., *MR image reconstruction from undersampled data by using the iterative refinement procedure.* PAMM, 2007. **7**: p. 1011207–1011208.

109. Cai, J.F., S. Osher, and Z.W. Shen, *SPLIT BREGMAN METHODS AND FRAME BASED IMAGE RESTORATION.* Multiscale Modeling & Simulation, 2009. **8**(2): p. 337-369.

110. Zhang, H., L. Cheng, and J. Li, *Reweighted minimization model for MR image reconstruction with split Bregman method.* SCIENCE CHINA Information Sciences, 2011.

111. Smith, D.S. and E.B. Welch, *Non-Sparse Phantom for Compressed Sensing MRI Reconstruction* Proc. Intl. Soc. Mag. Reson. Med. 19, 2011: p. 2845.

112. Michailovich, O., Y. Rathi, and S. Dolui, *Spatially Regularized Compressed Sensing for High Angular Resolution Diffusion Imaging.* Ieee Transactions on Medical Imaging, 2011. **30**(5): p. 1100-1115.

113. Ye, X., et al., *Fast MR Image Reconstruction for Partially Parallel Imaging With Arbitrary k-Space Trajectories.* IEEE TRANSACTIONS ON MEDICAL IMAGING, 2011 **30**(3).

114. van den Berg, E. and M.P. Friedlander, *PROBING THE PARETO FRONTIER FOR BASIS PURSUIT SOLUTIONS.* Siam Journal on Scientific Computing, 2008. **31**(2): p. 890-912.

115. Becker, S., J. Bobin, and E.J. Candes, *NESTA: A Fast and Accurate First-Order Method for Sparse Recovery.* Siam Journal on Imaging Sciences, 2009. **4**(1): p. 1-39.

116. Montesinos, P., et al., *High-resolution dynamic cardiac MRI on small animals using reconstruction based on Split Bregman methodology.* Nuclear Science Symposium and Medical Imaging Conference (NSS/MIC), 2011 IEEE, 2011: p. 3462-3464.

117. Cai, J., S. Osher, and Z. Shen, *Split Bregman Methods and Frame Based Image Restoration.* Multiscale Modeling & Simulation, 2010. **8**(2): p. 337-369.

118. Hankiewicz, J.H., et al., *Principal strain changes precede ventricular wall thinning during transition to heart failure in a mouse model of dilated cardiomyopathy.* Am J Physiol Heart Circ Physiol, 2008. **294**(1): p. H330-6.

119. Starck, J.L., M. Elad, and D.L. Donoho, *Image decomposition via the combination of sparse representations and a variational approach.* IEEE Trans Image Process, 2005. **14**(10): p. 1570-82.

120. Huang, Y., et al., *Bayesian nonparametric dictionary learning for compressed sensing MRI.* IEEE Trans Image Process, 2014. **23**(12): p. 5007-19.

121. Cand, E.J., et al., *Robust principal component analysis?* J. ACM, 2011. **58**(3): p. 1-37.

122. Adluru, G., et al., *Reconstruction of 3D dynamic contrast-enhanced magnetic resonance imaging using nonlocal means.* Journal of Magnetic Resonance Imaging, 2010. **32**(5): p. 1217-1227.

123. Han, S., et al., *Temporal/spatial resolution improvement of in vivo DCE-MRI with compressed sensing-optimized FLASH.* Magn Reson Imaging, 2012. **30**(6): p. 741-52.

124. Haldar, J.P., D. Hernando, and Z.P. Liang, *Compressed-sensing MRI with random encoding.* IEEE Trans Med Imaging, 2011. **30**(4): p. 893-903.

125. Leber, A.W., et al., *Accuracy of multidetector spiral computed tomography in identifying and differentiating the composition of coronary atherosclerotic plaques: a comparative study with intracoronary ultrasound.* J Am Coll Cardiol, 2004. **43**(7): p. 1241-7.

126. Achenbach, S., et al., *Detection of calcified and noncalcified coronary atherosclerotic plaque by contrast-enhanced, submillimeter multidetector spiral computed tomography: a segment-based comparison with intravascular ultrasound.* Circulation, 2004. **109**(1): p. 14-7.

127. Gudbjartsson, H. and S. Patz, *The Rician distribution of noisy MRI data.* Magn Reson Med, 1995. **34**(6): p. 910-4.

128. Chang, L.C., G.K. Rohde, and C. Pierpaoli, *An automatic method for estimating noise-induced signal variance in magnitude-reconstructed magnetic resonance images*, in *Medical Imaging 2005: Image Processing, Pt 1-3*, J.M. Fitzpatrick and J.M. Reinhardt, Editors. 2005, Spie-Int Soc Optical Engineering: Bellingham. p. 1136-1142.

129. Gharib, A.M., et al., *The feasibility of 350 mum spatial resolution coronary magnetic resonance angiography at 3 T in humans.* Invest Radiol, 2012. **47**(6): p. 339-45.

130. van Heeswijk, R.B., et al., *Motion compensation strategies in magnetic resonance imaging.* Crit Rev Biomed Eng, 2012. **40**(2): p. 99-119.

131. Li, D., et al., *Coronary arteries: magnetization-prepared contrast-enhanced three-dimensional volume-targeted breath-hold MR angiography.* Radiology, 2001. **219**(1): p. 270-7.

132. Johnson, K.R., et al., *Three-dimensional, time-resolved motion of the coronary arteries.* J Cardiovasc Magn Reson, 2004. **6**(3): p. 663-73.

133. Wang, Y., E. Vidan, and G.W. Bergman, *Cardiac motion of coronary arteries: variability in the rest period and implications for coronary MR angiography.* Radiology, 1999. **213**(3): p. 751-8.

134. Nguyen, T.D., et al., *Direct monitoring of coronary artery motion with cardiac fat navigator echoes.* Magn Reson Med, 2003. **50**(2): p. 235-41.

135. Shechter, G., et al., *Respiratory motion of the heart from free breathing coronary angiograms.* IEEE Trans Med Imaging, 2004. **23**(8): p. 1046-56.

136. Fabiano, S., et al., *High-resolution multicontrast-weighted MR imaging from human carotid endarterectomy specimens to assess carotid plaque components.* Eur Radiol, 2008. **18**(12): p. 2912-21.

137. Sun, B., et al., *Characterization of coronary atherosclerotic plaque using multicontrast MRI acquired under simulated in vivo conditions.* Journal of Magnetic Resonance Imaging, 2006. **24**(4): p. 833-841.

138. Wang, Y., S.J. Riederer, and R.L. Ehman, *Respiratory motion of the heart: kinematics and the implications for the spatial resolution in coronary imaging.* Magn Reson Med, 1995. **33**(5): p. 713-9.

139. Danias, P.G., et al., *Prospective navigator correction of image position for coronary MR angiography.* Radiology, 1997. **203**(3): p. 733-6.

140. Kawaji, K., et al., *Direct coronary motion extraction from a 2D fat image navigator for prospectively gated coronary MR angiography.* Magn Reson Med, 2013.

141. Scott, A.D., J. Keegan, and D.N. Firmin, *High-resolution 3D coronary vessel wall imaging with near 100% respiratory efficiency using epicardial fat tracking: Reproducibility and comparison with standard methods.* Journal of Magnetic Resonance Imaging, 2011. **33**(1): p. 77-86.

142. Abd-Elmoniem, K., A. Gharib, and R. Pettigrew, *Coronary vessel wall MRI at 3.0 T using Time-Resolved Acquisition of Phase-Sensitive DIR (TRAPD): initial results in patients with risk factors for coronary artery disease.* Journal of Cardiovascular Magnetic Resonance, 2013. **15**(Suppl 1): p. P26.

143. Montesinos, P., et al. *Motion, Resolution and Noise Thresholds for the Accurate Classification of Human Coronary Atherosclerotic Plaque by MRI*. in *ISMRM 21th Scientific Meeting & Exhibition*. 2013. Salt Lake City, Utah.

144. Nagata, M., et al., *Diagnostic accuracy of 1.5-T unenhanced whole-heart coronary MR angiography performed with 32-channel cardiac coils: initial single-center experience.* Radiology, 2011. **259**(2): p. 384-92.

145. Bo, L., et al. *REGULARIZED SENSE RECONSTRUCTION USING ITERATIVELY REFINED TOTAL VARIATION METHOD*. in *Biomedical Imaging: From Nano to Macro, 2007. ISBI 2007. 4th IEEE International Symposium on*. 2007.

146. Chatnuntawech, I., et al., *Accelerated H MRSI using randomly undersampled spiral-based k-space trajectories.* Magn Reson Med, 2014.

147. Real, R. and J. Vargas, *The Probabilistic Basis of Jaccard's Index of Similarity.* Systematic Biology, 1996. **45**(3): p. 380-385.

148. Bilgic, B., et al., *Fast dictionary-based reconstruction for diffusion spectrum imaging.* IEEE Trans Med Imaging, 2013. **32**(11): p. 2022-33.

149. Caballero, J., et al., *Dictionary learning and time sparsity for dynamic MR data reconstruction.* IEEE Trans Med Imaging, 2014. **33**(4): p. 979-94.

150. Zhang, T., et al., *Coil compression for accelerated imaging with Cartesian sampling.* Magn Reson Med, 2013. **69**(2): p. 571-82.